UNIVERSITY COLLEGE LONDON

Faculty of Mathematics and Physical Sciences

Department of Physics & Astronomy

ACTUATION OF THIN GLASS FOR GRAZING INCIDENCE X-RAY MIRRORS

Thesis submitted for the Degree of Doctor of Philosophy of the University College London

by

Thomas Catling

Supervisors:

Peter Doel

Giorgio Savini

Examiners:

Graziella Branduardi-Raymont

Richard Myers

January 30, 2017

I, Thomas Catling, confirm that the work presented in this thesis is my own. Where information has been derived from other sources, I confirm that this has been indicated in the thesis.

Abstract

This thesis follows on from work done by the Smart X-ray Optics (SXO) consortium, which consisted of seven UK institutions working between 2007-2011 to produce advances in active x-ray optics. Although some final optical testing of a SXO prototype is described herein, most of the work is aimed towards exploring simpler prototypes which make use of commercially available components. We explore a new, scalable and low-cost method of actuating thin sections of glass within the context of grazing incidence mirrors for x-ray telescopes. Finite element analysis is used to simulate different arrangements of actuators and mountings, then commercially available macro-fibre lead zirconate titanate (PZT) actuators are attached to the rear surface of 0.4mm glass to produce a simple new prototype with a small number of degrees of freedom. Raytracing is used to evaluate the importance of different aberrations with respect to optical performance. Deflectometry is explored as a method for measuring surface height, and singular value decomposition is used to derive orthogonal influence functions and command matrices for the new prototype. We find that, although this technique shows some promise, there are important issues which would need to be overcome if it were to be scaled up to produce a working telescope. A full-sized x-ray telescope may have thousands of mirror segments which would need to be individually calibrated. A robust methodology does not yet exist for this process, but the large amount of hysteresis and variability exhibited by PZT actuators will surely make it harder. More work needs to be done in this area, but in the meantime this technology could be useful to create low-profile mirrors for other applications.

Acknowledgements

I would like to thank the many people who have made the work in this thesis possible, and who have given me the support and motivation needed to see it through.

Many thanks go to my supervisor, Professor Peter Doel, for checking my work and providing a sounding board for ideas. I am also indebted to my second supervisors offical and otherwise, Dr Giorgio Savini and Dr David Brooks, for technical ideas and discussions.

I would like to thank all the friends I have made during my time in London who provided me with the emotional support, often unknowingly, to see this through to the end. A special mention goes to Oli Coles, who I sadly won't get to work with any more.

Finally, I would like to thank my family for all of the above and many other things besides.

True happiness comes from the joy of deeds well done, the zest of creating things new.

Antoine de Saint-Exupery

Contents

List of Figures

Chapter 1

Introduction

1.1 Outline

The chapters in this thesis have three broad themes: an overview of x-ray astronomy which provides the scientific motivation for high resolution active imaging (chapters 1-3); the description of, and results of, tests on an existing active x-ray mirror prototype (Chapter 4); and the design and testing of a new simplified prototype (chapters 6-9).

This work was undertaken between 2012 and 2016 under the supervision of Professor Peter Doel, with funding from the Science and Technology Facilities Council (STFC).

1.2 Contemporary Paradigms in X-Ray Astronomy

The history of x-ray telescopes stretches back about fourty years to the 1970s, at which point the launch of Uhuru allowed a serious study of exotic astronomical objects, such as black holes and neutron stars, to begin. Several small satellites and observatories were launched in the next few decades, notably including XMM-Newton and Chandra in 1999. These two instruments have since defined the imaging limits of x-ray astronomy, being paragons of collecting area and angular resolution respectively. The two largest missions since then, Suzaku and NuSTAR, have carried primarily spectroscopic instruments; in terms of imaging, the resolution of Chandra and the sensitivity of XMM-Newton have yet to be surpassed (Willingale et al. (2013)).

In the last several years, interest in the workings of the early and energetic universe (see Chapter 2) has created a growing need for a new x-ray observatory with Chandra-like resolution and greater sensitivity than XMM-Newton (Elvis et al. (2006); Barcons

et al. (2012)). This need has prompted various proposals which have been through many amalgamations and changes.

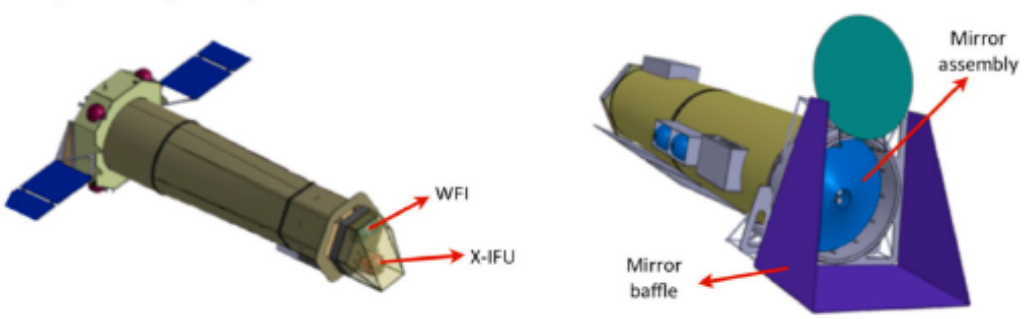

Figure 1.1. An early industrial design rendering of ATHENA with the Wide Field Imager (WFI) and X-ray Integral Field Unit (X-IFU) at the focal plane (Nandra et al. (2013)).

ATHENA, shown in Figure 1.1, is the latest incarnation of these plans and is the result of a reformulation of the International X-Ray Observatory (IXO) proposal, which was itself a combination of the XEUS and Constellation-X mission concepts (Bavdaz et al. (2009a, 2011)). The latest design contains a single silicon mirror assembly with a 12m focal length, carrying two main instruments; the WFI (Wide Field Imager) and the X-IFU (X-ray Integral Field Unit) providing spatially resolved high-resolution x-ray spectroscopy.

ATHENA has now been selected as the second L class science mission for launch in 2028 as part of ESA's Cosmic Vision 2015-25 plan[1], the theme of which is 'The Hot and Energetic Universe'. The science motivating this mission has set basic constraints on collecting area of $2m^2$ at 1keV, and angular resolution of 5 arcseconds (Willingale et al. (2013)). These specifications, although lower than for the previously proposed IXO, are still technically demanding and require new technologies.

The proposed ATHENA mission will implement modified Wolter-Schwarzchild optics using Silicon Pore Optics (SPO) technology, which consists of layers of very precisely machined and polished silicon. These layers form monolithic porous blocks, with machined grooves on each layer creating pores which allow light to pass through and be deflected (Willingale et al. (2013)). This technology was originally developed for the XEUS mission concept (Beijersbergen et al. (2004); Bavdaz et al. (2004)) and has persisted through various project iterations due to its high Technology Readiness Level (TRL) and ability to produce very rigid optics with reasonable angular resolution.

Slumped glass was also considered as a backup technology for IXO and is still being investigated by several groups in Europe and the US (Bavdaz et al. (2009b); Friedrich

[1] http://sci.esa.int/cosmic-vision/54241-athena-to-study-the-hot-and-energetic-universe/

et al. (2006)). This technology has a lower TRL but is attractive because of its similarly scalable nature (slumping flat sheets using mandrels) and the flight heritage of coated glass optics in x-ray missions (e.g. Chandra). These competing technologies and others are described in more detail in Chapter 3.

The work done in this thesis investigates the feasibility of adding piezoelectric actuators to the rear of thin slumped glass sections to improve their figure at low and mid orders, which in mirrors of this size typically corresponds to aberrations with spatial frequencies of several cm and above. This approach has been used in the past to produce several prototypes (Rodriguez Sanmartin et al. (2010)) with various substrates; testing of one of these prototypes is described in Chapter 4. Chapters 6-9 of this thesis will detail the design and testing of a new prototype which uses a different type of piezoelectric actuator, which is cheaper and better suited to low order corrections on scales of 5-10cm.

Although the initial IXO proposal which suggested sub-arcsecond resolution was deemed too technically difficult at the time, the need for higher resolution x-ray imaging persists and has recently resulted in a strawman proposal named the X-ray Surveyor Mission (Gaskin et al. (2015)). This validates the relevance of continued research into this area along many avenues, as the silicon pore technology proposed for ATHENA is unlikely to be capable of sub-arcsecond resolution without huge investment. In Chapter 2 we discuss the scientific motivation behind moving towards higher resolution, lightweight x-ray optics.

The above outline serves to give some idea of the context which surrounds the developmental work described in this thesis. Although active optics are not currently proposed for ATHENA, the growing need for high sensitivity, high resolution x-ray telescopes makes their use likely at some point in the future, despite great advances in optical manufacturing.

1.3 Focussing X-Rays

Before going through the science motivation and technological requirements for high sensitity, high resolution x-ray optics, it is prudent to give an overview of the form and physics behind the most common optical structures of a grazing incidence x-ray telescope - the Wolter I and Wolter-Schwarzchild geometries.

The reflectivity of a surface in the x-ray band depends strongly upon the atomic weight of the atoms within the surface and the angle of incidence of the incoming photons. Figure 1.2 shows this for various atomic weights and incident energies; for an x-ray telescope to be useful it is best to have an angle of incidence of no more than one or two degrees.

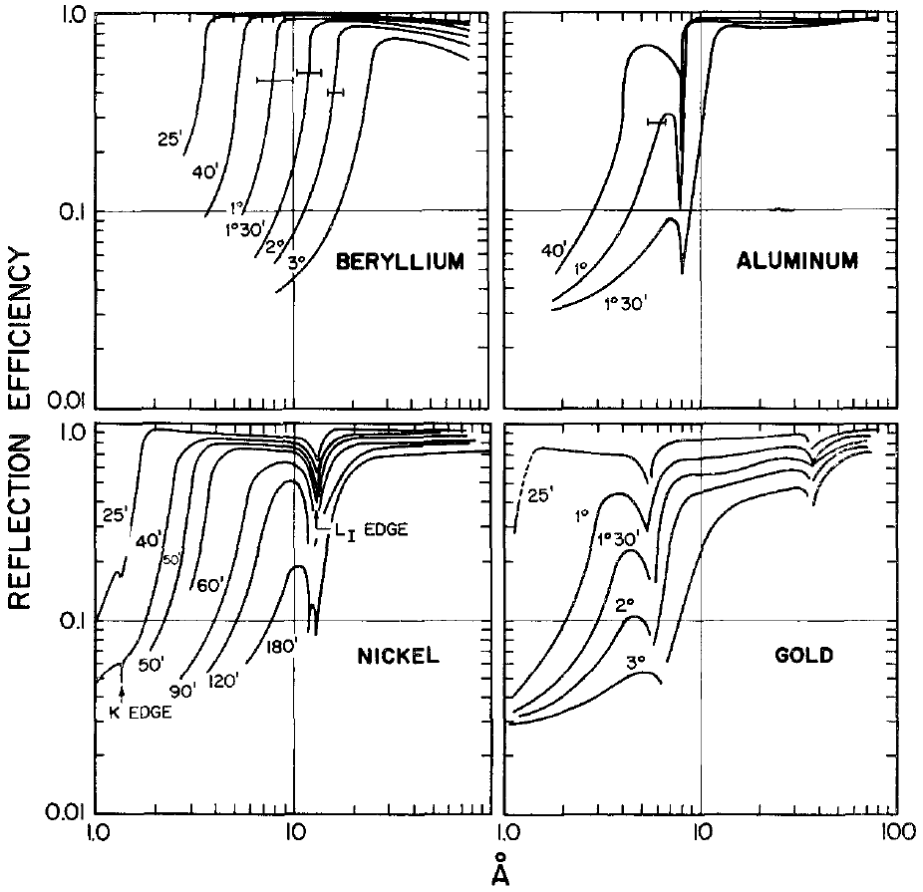

Figure 1.2. Theoretical reflectance vs. wavelength for various materials and incidence angles. Figure taken from Giacconi et al. (1969).

Although there are other ways of creating an image without exceeding this critical angle of incidence, the Wolter I and Wolter-Schwarzchild forms are most common in imaging telescopes. The basic Wolter I form shown in Figure 1.3 consists of two separate cylindrically symmetric, confocal sections of a hyperboloid and a paraboloid. The Wolter-Schwarzchild geometry contains minor adjustments to this shape (generally less than 1μm in most systems) which reduce the effects of coma and thus improve the off-axis resolution of the mirror (Aschenbach (2009)).

It can be seen from looking at Figure 1.3 that the collecting area presented along the optical axis is actually a narrow ring rather than a disc, and is much smaller than the physical mass of the mirror would allow with a 'normal' mirror configuration. This makes x-ray telescopes costly to produce because they must be launched into space (due to the very low atmospheric transmission at x-ray wavelengths) despite being disproportionately heavy, and the expensive, well figured surface of the mirror is comparatively under-utilised. To increase the collecting area, segments are usually stacked as shown in Figure 1.4.

Stacking the mirrors increases the collecting area as expected but necessitates making them thinner to avoid self-obstruction, so the surface form of the optic is naturally harder

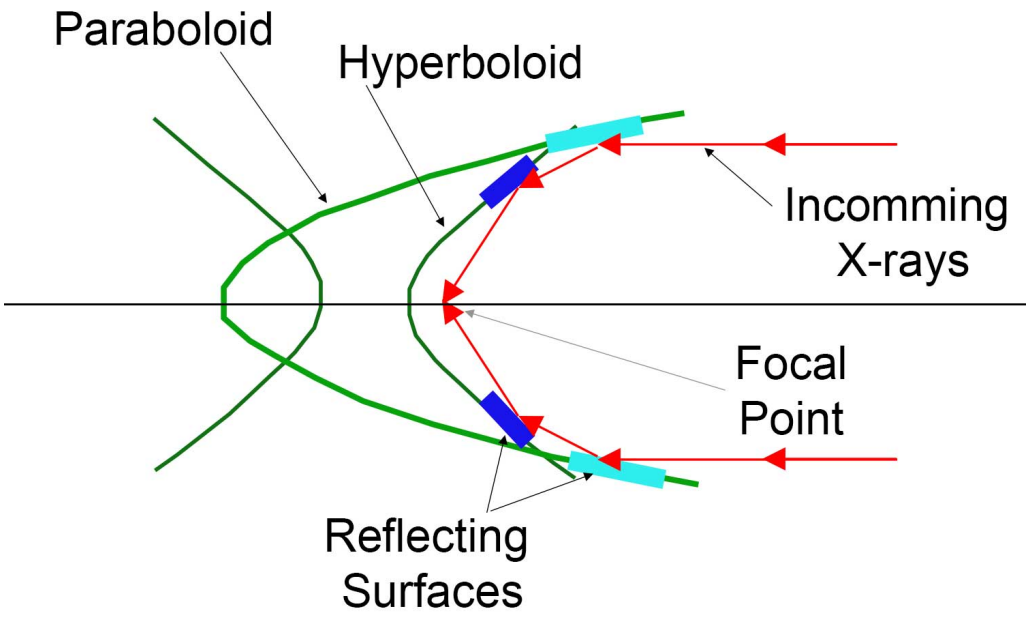

Figure 1.3. The Wolter I form consists of two separate cylindrically symmetric, confocal sections of a hyperboloid and a paraboloid. Light is usually deflected by both sections before coming to a focus (image credit: NASA).

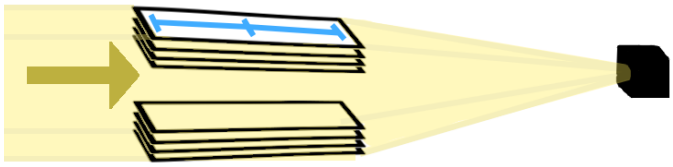

Figure 1.4. Stacking of grazing incidence mirrors to increase their effective area.

to manufacture accurately and is more prone to distortion. Grazing incidence mirrors are very sensitive (more than normal incidence mirrors) to surface finish, form and alignment (Korsch et al. (1979)), which makes high resolutions relatively harder to achieve. Historically, this problem has been approached by prioritising either collecting area or resolution. Chandra and XMM-Newton epitomise these two approaches; Chandra (Figure 1.5) uses four pairs of monolithic segments of glass, each 2cm thick and together weighing almost a tonne, to achieve a resolution of around 0.5" (compared to Hubble Space Telescope resolution of around 0.05"). In contrast, XMM-Newton (Figure 1.6) uses three separate mirror assemblies which each contain 58 concentric electroplated mirrors. This gives almost six times the collecting area of Chandra but the figure of the thin mirrors limits resolution to around 10".

As an aside, it is worth noting that terms like collecting area and resolution require

additional caveats when used in connection with grazing incidence optics. The reflectance of a surface at such extreme angles and energies varies sharply with the angle of incidence, as shown in Figure 1.2. The unofficial standard in the x-ray community is to refer to the effective collecting area at an energy of 1KeV (around 10Å); this convention is also employed here unless otherwise stated.

Resolution is always difficult to describe with a single number. We follow here the normal convention used in the literature of using the on-axis Half Energy Width (HEW), which is the radius of a circle on the focal plane which contains half of the incident flux. The off-axis performance of grazing incidence optics is also very variable depending upon the exact optical configuration.

Figure 1.5. Chandra used four pairs of massive thick mirrors with a very accurate surface but with limited effective area (image credit: NASA).

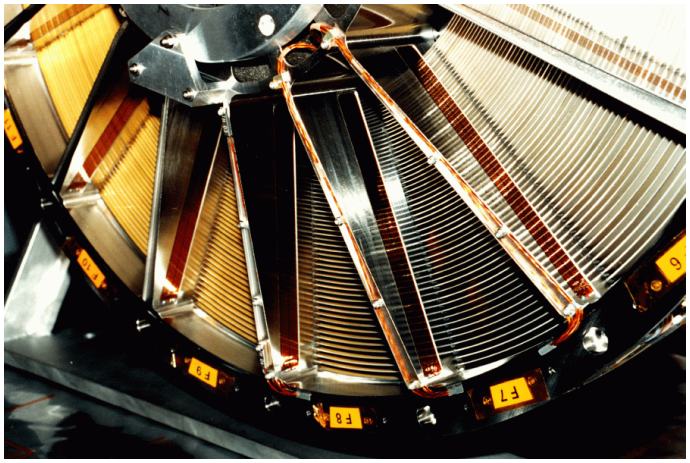

Figure 1.6. XMM-Newton uses stacks of many thin mirrors, prioritising effective area over resolution (image credit: NASA).

Chapter 2

Science Motivation

X-Ray astronomy can tell us information about the universe at nearly all scales; from the creation of super-massive black holes (SMBHs) (Aird et al. (2013)) to their effect on galaxy and galaxy cluster formation (Cappi et al. (2013); Croston et al. (2013)). In this chapter the science case will be made for high resolution, high sensitivity x-ray astronomy, which necessarily requires novel optics such as those described in Chapter 3 and the rest of this thesis.

The European Space Agency (ESA) has selected 'The Hot and Energetic Universe' for the science theme of the L2 mission due for launch in 2028. Two key questions are posed by this theme: 1) How does ordinary matter assemble into the large-scale structures we see today? and 2) How do black holes grow and shape the Universe? (Nandra et al. (2013)).

To address these questions we must first map the hot gas structures in the Universe and determine their physical properties and evolution through cosmic time. Second, it is necessary to find SMBHs, even in obscured environments and at high redshifts, and observe the distribution of matter and energy around them as they grow. Because of the high temperature of these gaseous components of the universe, and because of the energetic nature of the environment near SMBHs, these observations must be taken in the x-ray band. Producing new science here requires high sensitivity and resolution, which has led to the proposal of ATHENA. In this chapter we will explain why existing x-ray observatories are not capable of answering these questions, and why new x-ray optics are required.

Figure 2.1 shows simulated 50ks exposures of the Perseus Cluster core taken with

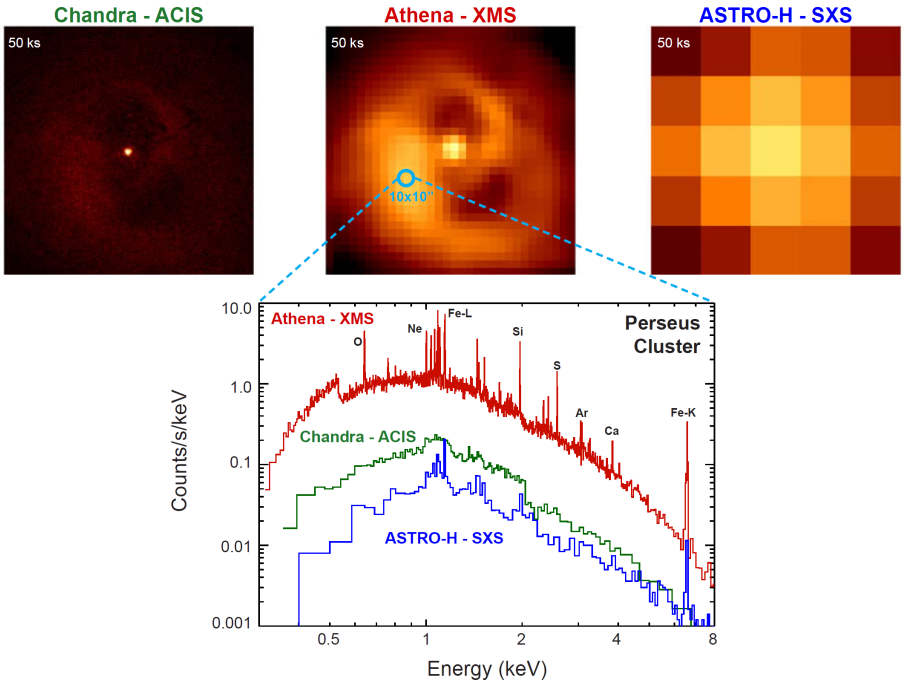

Figure 2.1. An image of the Persus Cluster core simulated for 50ks observations from Chandra ACIS-I, ATHENA XMS and ASTRO-H SXS. The bottom panel shows the simulated spectrum from a 10"x10" region, although the angular resolution of ASTRO-H would actually prohibit it from analysing a region this size. While Chandra images the core of the cluster well, its spectral resolution is too poor to give good data on emission lines and its sensitivity is too low to properly expose the diffuse gas around the core. ASTRO-H has excellent spectral resolution but the angular resolution is too poor to resolve the gaseous structure and its sensitivity is too low to detect many of the emission lines. The combination of resolution and sensitivity in ATHENA allows far more information to be gained on gas flow and AGN feedback from an equivalent exposure. Figure taken from Barcons et al. (2012)

ASTRO-H, Chandra, and the proposed ATHENA X-ray Microcalorimeter Spectrometer (XMS). Chandra has excellent angular resolution but lacks the sensitivity to reveal diffuse features adjacent to the core of the cluster, and poor spectral resolution causes interesting emission lines to be missed. ASTRO-H has good spectral resolution but the angular resolution is bad, and the sensitivity is too low to detect emission lines from diffuse components without a longer exposure time. Because of its unique combination of high resolution and large collecting area, ATHENA will be able to resolve the cluster core and successfully capture the gaseous components. The new instrumentation onboard will also have enough spectral resolution to provide good data on emission lines.

Figure 2.2 shows the weak line spectroscopic capability of ATHENA compared to Chandra/XMM-Newton and ASTRO-H. Although the calorimeter used in the ASTRO-H SXS is a very high resolution instrument, the collecting area of the telescope means that it will be severely photon-starved for observations outside of the local universe. For

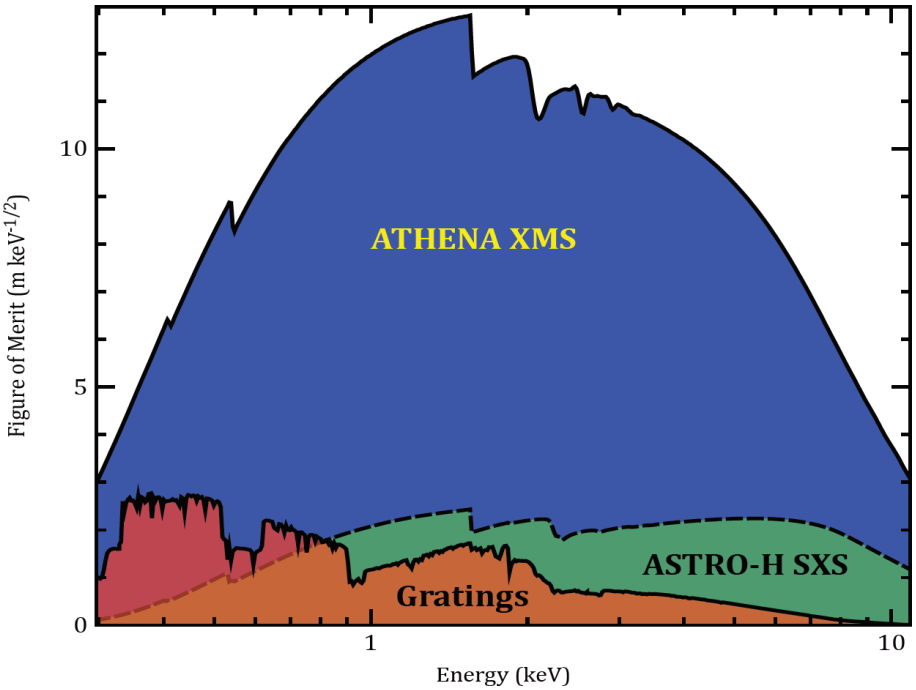

Figure 2.2. A 'figure of merit' analysis of weak spectral line sensitivity, derived from the number of counts per independant spectral bin, shows the greatly improved ability of the ATHENA XMS instrument to detect these lines. Figure taken from Barcons et al. (2012)

example, in Figure 2.1 it can be seen that spectroscopic analysis of the Perseus Cluster using ASTRO-H SXS misses many of the emission lines which are visible in the ATHENA analysis. The large collecting area of ATHENA, combined with great improvements over XMM-Newton and Chandra gratings, allows it to exceed the spectroscopic capabilities of any other observatory in the x-ray band.

Figure 2.3 shows the number of sources expected to be detected in a single exposure at high galactic latitudes for ATHENA, XMM-Newton and Chandra. The wide field of view of ATHENA (40 arcminutes compared to ∼30 arcminutes for Chandra and XMM-Newton), good sensitivity and superior off-axis performance allow it to perform surveys far faster than either Chandra or XMM-Newton. This is essential in studies of AGN feedback, as candidate objects must be discovered before observations can be followed up with other telescopes.

The figures mentioned above use ATHENA as an example of why a large collecting area, high resolution x-ray observatory with a good field of view is necessary to advance our knowledge of 'The Hot and Energetic Universe.' ATHENA is specified to have an angular resolution of 5 arcseconds HEW, a collecting area of $2m^2$ at 1keV and a 40 arcminute field of view. A general argument can be made that a certain minimum sensitivity is needed for cosmic sources, along with a certain minimum useful resolution to prevent

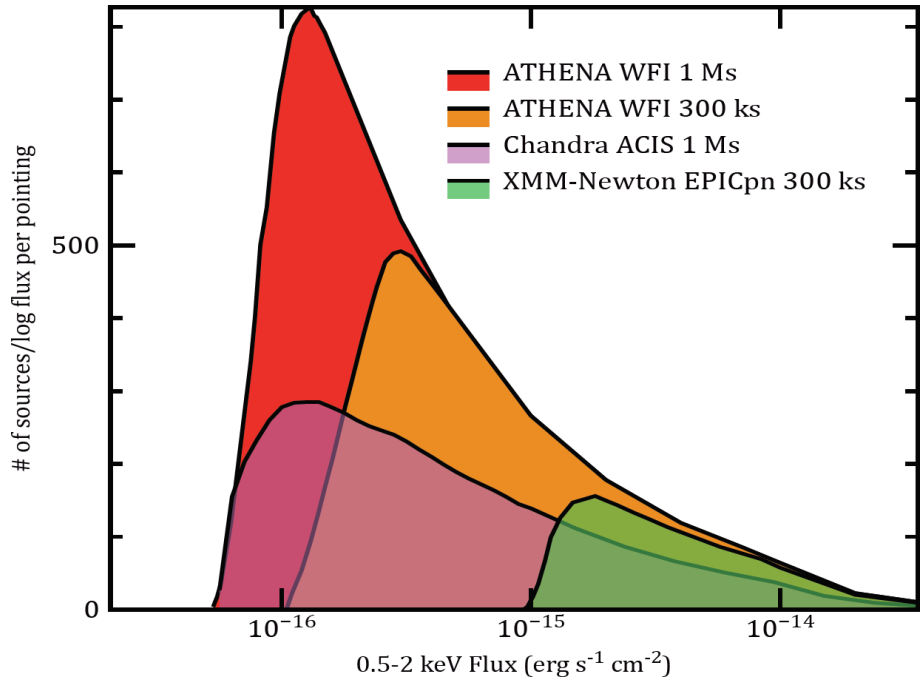

Figure 2.3. ATHENA is expected to detect many more sources than Chandra or XMM-Newton in a single exposure at high galactic latitudes, due to its large field of view, high sensitivity and good off-axis performance. Figure taken from Barcons et al. (2012)

source confusion. Willingale et al. (2013) placed these limits at 10 arcseconds and 0.1m^2 respectively and produced the plot shown in Figure 2.4, which neatly shows this 'Golden Quadrant' and its position relative to existing missions.

This is of course a simplification, but it is still useful to see how ATHENA compares to previous missions using these simple metrics. The recent strawman proposal of the X-ray Surveyor mission proposes a similar field of view and collecting area but a much higher, sub-arcsecond resolution.

Finally, Figure 2.5 shows various x-ray mirror technologies and the rough collecting area/angular resolution envelope they occupy. ATHENA is outside the capability of existing technologies such as monolithic shells (Chandra) or thin foils (ASTRO-H) and a new tecnology, Silicon Pore Optics (SPO), is nominated. SPO is explored further in Chapter 3, along with other candidate technologies for high resolution x-ray imaging. The X-ray Surveyor mission is outside the envelope of Silicon Pore Optics in terms of resolution, and most likely requires actively corrected optics of some kind, such as those discussed in this thesis.

The key point of this figure is that a new technology is needed to achieve the specifications required to create Figures 2.1, 2.2 and 2.3. This is the motivation for looking at new ways of creating high resolution, lightweight and stackable x-ray mirrors.

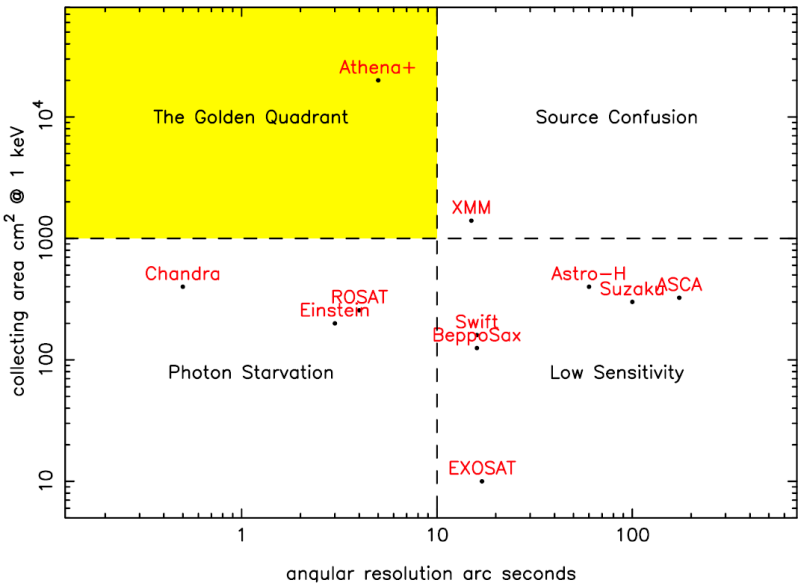

Figure 2.4. A diagram showing the collecting area and angular resolution of previous x-ray missions compared to ATHENA. The 'Golden Quadrant' describes an ideal area where sources are both clearly detected and well resolved. Figure taken from Willingale et al. (2013).

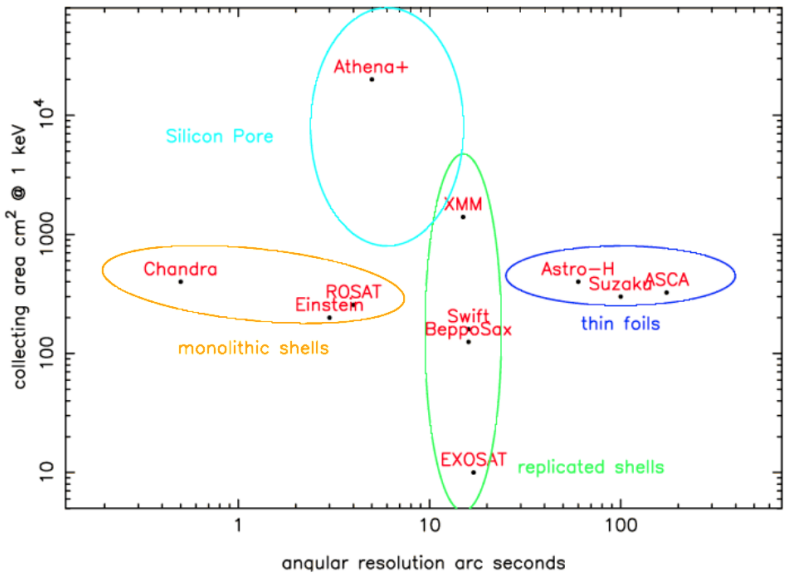

Figure 2.5. A diagram showing the collecting area and angular resolution of different x-ray mirror technologies and missions. Figure taken from Willingale et al. (2013).

A fifth technology not shown in Figure 2.5 is slumped glass optics; this is explored more in Chapter 3. The theoretical limits on collecting area with this technology are comparable to SPO, but the limits on resolution could be better if the optics were well mounted and actively corrected as in the X-ray Surveyor proposal (Gaskin et al. (2015)). These glass shells often need only low order corrections (Civitani et al. (2011); Proserpio et al. (2011)); this is the motivation for the work done in the last half of this thesis on actuating thin sheets of glass.

Chapter 3

Technology Review

3.1 Technology Review

There are only a handful of groups working on next generation x-ray mirrors (active or otherwise) around the world, and there are now two technologies which have emerged as favourites for the next high resolution imaging x-ray missions: SPO and slumped glass (Bavdaz et al. (2013)).

SPO has many possible advantages over glass, despite having little heritage in space-borne missions. The semiconductor industry has huge amounts of experience and money invested in machining and growing silicon; this is a very mature technology with the benefit of having massive commercial applications, which significantly lowers cost. It is important that any technology to be used for the next generation of x-ray mirrors be highly scaleable, since a large x-ray telescope may make use of many thousands of small, discrete mirror segments. This is the current technology selected for Athena+ (Civitani et al. (2010); Nandra et al. (2013)).

Silicon can be grown as large single crystals with almost no internal stresses, making it a very stable material to cut and machine (Gnther et al. (2006)). Large crystals are cut into wafers, which are then scored with precise channels. These scored wafers are then bent, stacked and glued on top of each other, creating a very rigid, stable structure pierced by a regular grid of pores (Figure 3.1). There are many mechanical advantages of working with silicon, and an x-ray telescope with a large collecting area and a resolution of 2-3" may be achievable soon using this technology (Collon et al. (2013)).

Work has also been done on manufacturing monolothic silicon optics, again because

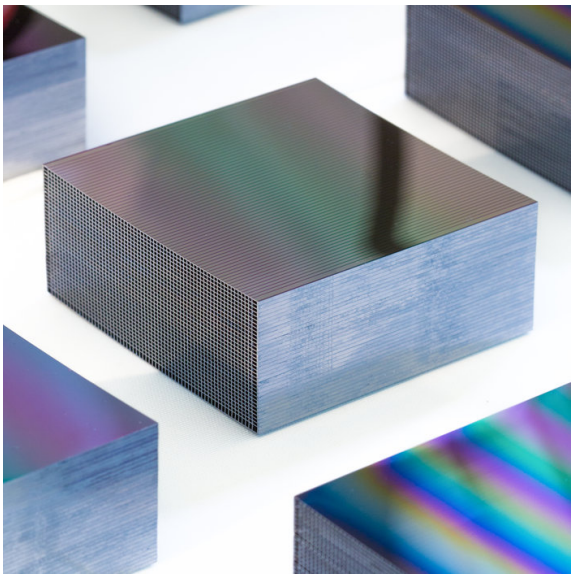

Figure 3.1. Silicon pore optic.

of the low internal stresses present in a grown crystal. Riveros et al. (2014) were able to produce a lightweight silicon shell using a combination of machining, polishing and etching to remove surface cracks from material removal (Figure 3.2).

However, for very high resolution (arcsecond and sub-arcsecond) x-ray imaging, slumped glass mirrors are still the favourite candidate (McClelland et al. (2013)). Slumping involves placing a flat piece of thin (normally 0.4mm) glass onto a mandrel which is then inserted into an oven. The temperature is controlled such that the glass softens enough to conform to the shape of the mandrel. High quality thin glass is now widely available due to its inclusion in many displays, so the material is very cheap. The major technical issues with

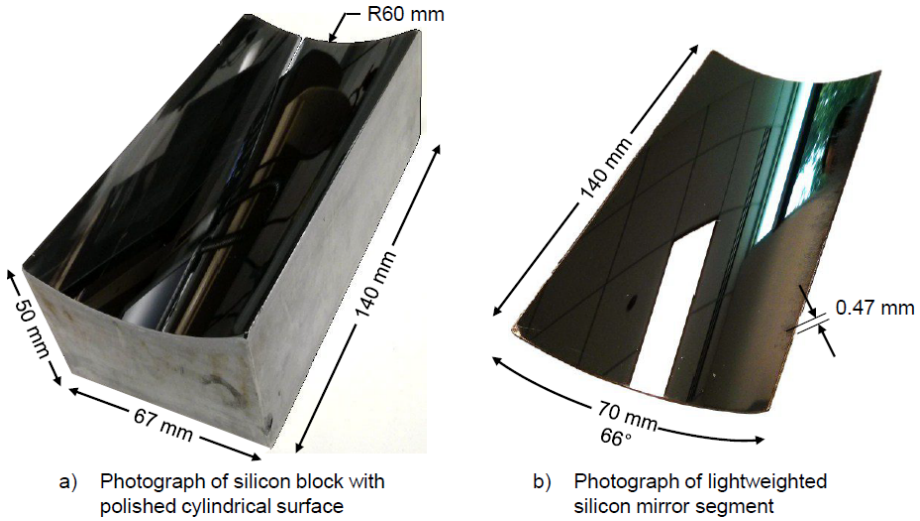

Figure 3.2. Monolithic silicon optic. Riveros et al. (2014)

Figure 3.3. Slumped glass on mandrel.

un-actuated slumped glass are alignment and the surface finish and ripple produced during the slumping process itself. There are various approaches to automate the alignment, which will also be essential if enough segments are to be assembled for a telesope with a reasonable collecting area (Civitani et al. (2011)).

The slumping process is difficult for many reasons. The mandrel is usually porous ceramic and quite rough; if the glass is directly slumped (optical face downards) this roughness is transferred to the optical surface. However, if the glass is indirectly slumped there is less control over the final form as the optical surface is directly affected by thickness variations in the glass. There are also difficulties associated with differing Coefficients of Thermal Expansion (CTEs) between the mould and the glass and springback effects after forming (Winter et al. (2013)). Some work has been done on slumping the glass onto an air bearing, but this technique is still being developed (Sung et al. (2013)).

In terms of actuation of thin glass, the technique which has shown most promise so far involves sputtering Lead Zirconate Titanate (PZT) actuators and electrodes onto the rear surface of the mirror (Reid et al. (2012); Allured et al. (2015)). There are many advantages to this, including great control over actuator layout and shape, and the low stress introduced during the sputtering process compared to gluing. This technique has

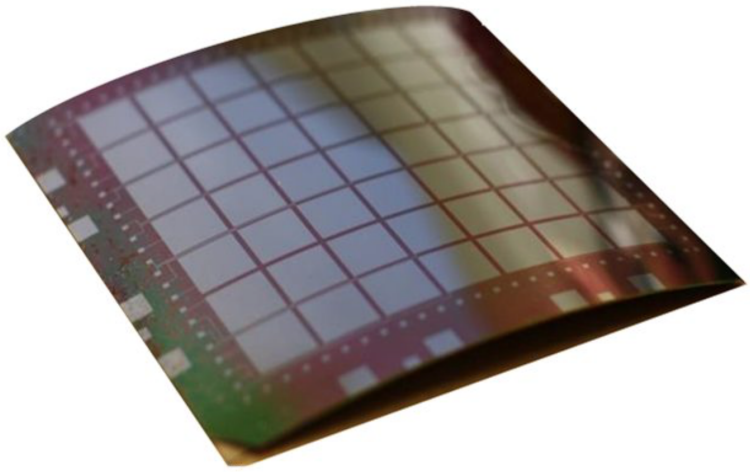

Figure 3.4. An image of PZT actuators deposited onto the rear surface of a thin glass mirror. Allured et al. (2015)

been quite successful so far but is still very experimental; although good agreement is now observed between desired and observed influence functions, the glass being used is still substantially thicker than the ideal and a percentage of sputtered actuators are inoperable in any given test. Most of the prototypes produced so far with this technique have focussed on zonal corrections with an actuator size of around 10mm. This is an ongoing paradigm with early tests of new actuator technologies and is understandable in that it pushes the limits of the technology and allows testing of repeatability in both use and manufacturing. However, any practical use case must pay attention to the surface deformations that can be obtained with a given arrangement and type of actuator, and zonal strategies can make certain common modes difficult to obtain. Consider, for instance, how to obtain curvature in only a single axis with this type of actuator.

In addition to the above, some work has been done on depositing magnetostrictive films onto glass, which then allow strains to be 'written in' using a magnet in the same way that a cassette tape can be programmed by a write head (Wang et al. (2015)). This work shows promise but there are issues with high temperatures used during the process (as with the above PZT sputtering) and leakage from magnetic fields induced in adjacent mirrors. Work has also been done on passive correction of thin shells using ion figuring and differential deposition (Ulmer et al. (2012)). It may be that a combination of both passive and active correction is necessary to create a mirror module capable of sub-arcsecond resolution.

Very recently, work has been done on applying commercial PZT actuators to grazing incidence mirrors. The advantages of this are lower cost and simplicity, the difficulties

come from glue shrinkage and CTE differences. However, it can be shown that the modes introduced by these effects are generally able to be corrected by the actuators themselves (Spiga et al. (2014, 2016)). More research needs to be done on the effects of charged radiation on piezoelectric actuators in space (Ulmer et al. (2012)), as it is conceivable that ionising radiation could alter the charge on piezoelectric actuators and thus change the stress imparted to the mirror.

The work done in chapters 6-9 follows a similar idea but with actuators which move primarily in one direction tangential to the surface instead of two. We hope to make use of commercial macro-fibre actuators and correct low to medium order errors with a modal approach which allows fewer degrees of freedom; see Figure 3.5 for an example. The advantage of using a modal, rather than zonal, approach is that low order modes (such as those caused by springback from slumping) can be corrected with small number of actuators. Lower degrees of freedom also make the system as a whole much easier to characterise. The advantages over sputtered actuators are primarily simplicity, cost and reliability, and the avoidance of problems associated with poling actuators attached to a fragile, thin substrate. PZT actuators must be 'poled' before they exhibit a coherent piezoelectric effect; this requires a high electric field and temperature, which can damage or disfigure any attached optic (this is discussed in Reid et al. (2012); Allured et al. (2015))). However, by attaching actuators directly we are forced to use some kind of adhesive which comes with its own set of problems. The mirror in Figure 3.5 uses double-sided polyimide tape. Although this tape is cryo-compatible and low-outgassing, it obviously has drawbacks in terms of repeatability and rigidity which need to be quantified.

There are also many things to be considered with active x-ray mirrors which have not been fully addressed in the literature. For example, mounting will be very important but has not been much discussed (Feldman and Willingale (2012)). Because the forces involved in actuating a thin mirror are very small, and because by its nature a stacked mirror can only really be supported from its edges, it is difficult to support the mirror without constraining it in a way which introduces extra deformations. Conversely, it is difficult to adjust the mirror without some kind of reaction structure to push against. Calibration of the actuators has also not been widely considered, and this will be a problem when a telescope has several thousand degrees of freedom and a relatively dim calibration source. One possibility is that the piezoelectric actuators could be used as strain sensors during ground calibration, and the mirrors could then be re-actuated in space to match the calibration strain (Reid et al. (2012)). Another possible approach could be to take several intrafocal measurements of the intensity, possibly even at optical wavelengths, and use

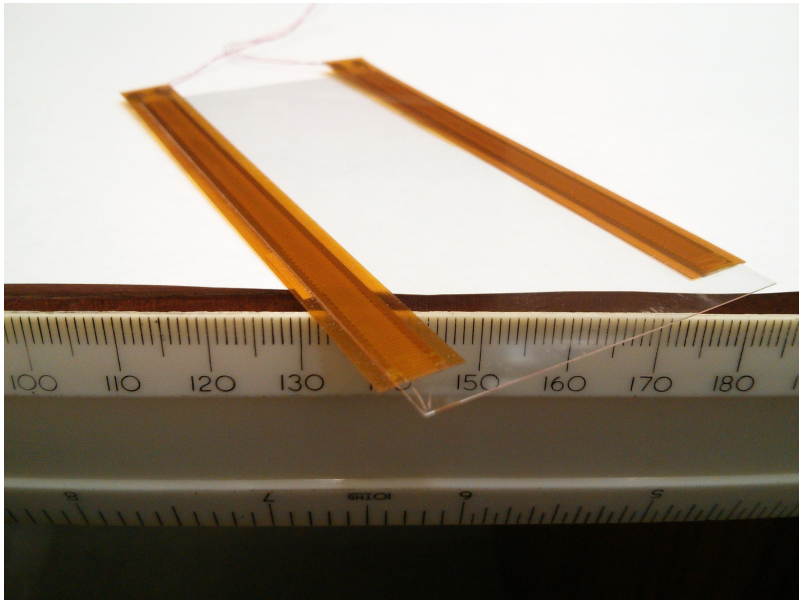

Figure 3.5. Macro fibre composite PZT actuators attached to a thin sheet of glass.

this to derive the shape of the mirror segments (Spiga et al. (2013); Spiga et al. (2014)). This would require a reasonable flux, as well as the placement of at least two detectors, or a single moveable detector, within the optical path inside the focus of the mirrors. This is a fairly new field which faces a lot of difficult technical challenges.

Chapter 4

Smart X-Ray Optics and NEMO2

4.1 NEMO2

The first eighteen months of the work described herein were focussed on finalising metrology of NEMO2 (the origin of this acronym is mysterious), which is one of two final active x-ray mirror prototypes produced by the UK Smart X-Ray Optics (SXO) consortium between 2007 and 2011 (Feldman (2009); Atkins (2009)). SXO consisted of seven UK institutions (including UCL) and was funded by an Engineering and Physical Sciences Research Council (EPSRC) basic technology grant, which has now run its course. The aim of the consortium was 'to design and develop X-ray focussing technology for both small and large scales.' The intention was to use NEMO2 to design tests which would be useful for NEMO1. NEMO1 has been kept clean and boxed since it was determined to have a slightly better form (Feldman et al. (2010)), whereas NEMO2 has seen a lot of rough handling and is unsuitable for use in vacuum with exposed detectors and optical elements.

The latter part of this plan was not implemented, as it was determined after testing NEMO2 that there were too many degrees of freedom for either mirror to be useful in a conceivable x-ray telescope, and the 'puckering' action of the actuators made low order corrections (necessary due to stresses created during electroplating) difficult. The electroplating technology used to produce NEMO1 and NEMO2 is also now out of favour for this application, and it seemed more useful to investigate actuation of more relevant substrates (e.g. slumped glass) with better actuators (e.g. macro fibre composites). Nevertheless, the process and results of testing NEMO2 are presented in this chapter for the sake of

completeness.

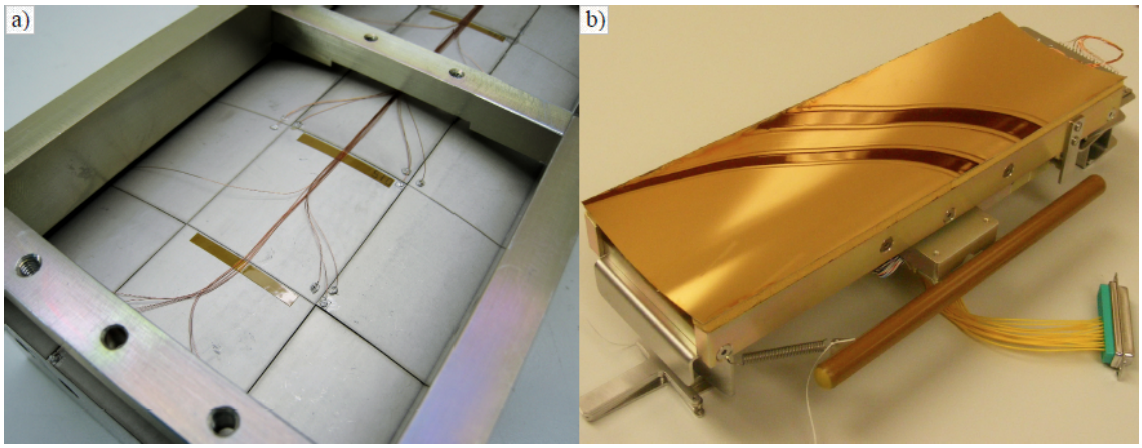

Figure 4.1. Image of NEMO2 rear surface with closely spaced actuators (a) and optical surface (b) (Rodriguez Sanmartin et al. (2010))

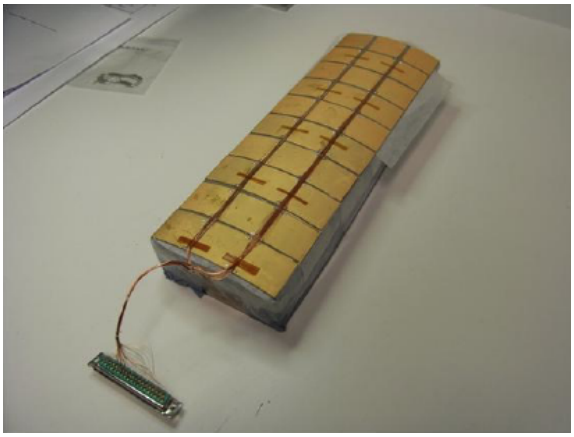

Figure 4.2. A rear view of a first generation prototype produced prior to NEMO2. Gaps between the actuators are easily visible and are between 0.5-1mm wide (O'Dell et al. (2012)).

NEMO2 (shown in Figure 4.1) consists of a 400 μm thick nickel shell with 24 piezoelectric ceramic actuators attached to the back surface in a grid arrangement. It is similar in construction to the earlier prototype shown in Figure 4.2, except that the actuators have been precisely machined to reduce the spacing between them, which is now estimated to be $\sim$ 20μm (Rodriguez Sanmartin et al. (2010)). All of these prototypes are nominally segments of an ellipsoidal surface with 28m between focii and a radius of curvature of $\sim$15cm at the section where the mirror is formed, roughly 4.5m away from one focus. To the naked eye they look like 10cm by 30cm cylindrical segments with $\sim$15cm radius of curvature (see Figures 4.1 and 4.2). This shape is designed for point-to-point focus testing

in the University of Leicester X-Ray Test Tunnel Facility.

4.2 Actuator Print-Through ('Kinks')

One of the main aims in constructing NEMO1 and NEMO2 was the avoidance of 'kinks' which had been present in earlier prototypes. These kinks are difficult to avoid when attaching actuators to thin substrates. The flexibility of the substrate allows the influence functions and effects of glue shrinkage to become very localised, effectively introducing high order errors which cannot be corrected by the actuators. Figures 4.3 (Feldman et al. (2009)) and 4.4 (Zhang et al. (2009)) show the effect of this in the prototype shown in Figure 4.2, along with the generally poor shape of the mirror compared to its ideal. It was thought that this could be improved by reducing the inter-actuator spacing (Feldman et al. (2009); Zhang et al. (2009)).

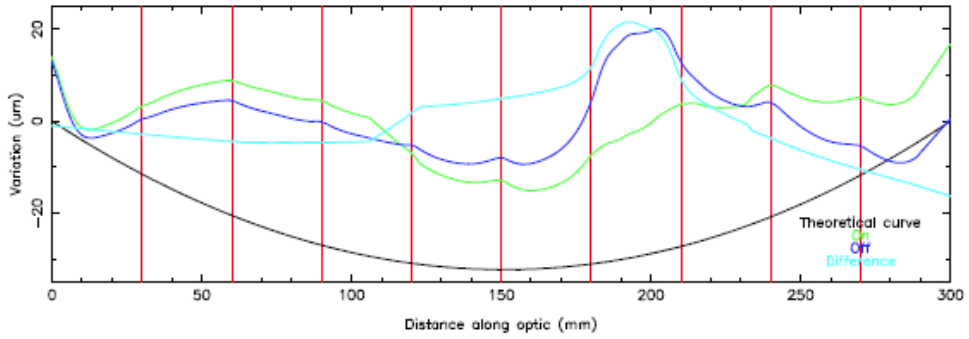

Figure 4.3. Generally poor form and kinking are clearly visible from an older prototype with large inter-actuator spacing. Red lines mark the actuator boundaries, where the surface height of the mirror can be seen to 'kink'. The thick black line indicates the theoretical shape of the mirror, from which the measurements deviate by several tens of microns. (Feldman et al. (2009))

Other lessons learned from the errors in Figure 4.3 and 4.4 were also applied to the construction of NEMO1 and NEMO2. Great attention was paid to the thickness of the glue layer and the stresses created when electroforming the nickel substrate (Feldman (2009); Atkins (2009)). Unfortunately, testing of either prototype could not be completed before the end of SXO budgetary period (Feldman et al. (2010)), so the work documented here represents the only real test of the improvements.

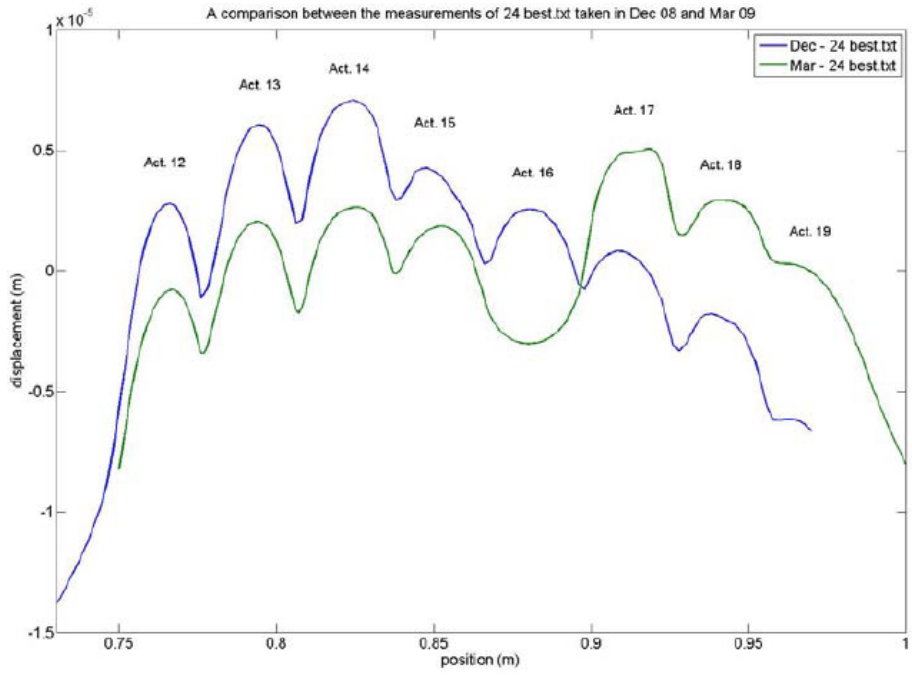

Figure 4.4. Extreme kinking is observed with thin substrates when no effort is made to control inter-actuator spacing. Zhang et al. (2009)

4.3 Interferometric Testing

The tests described herein were limited by equipment, finances, and availability of the people previously involved in the project. The equipment used to produce Figures 4.3 and 4.4 was not available, so alternative methods were researched. The key aim was to investigate whether the careful gluing of NEMO2 reduced the actuator print through, which was the major problem in previous designs. Figure 4.5 (Zhang et al. (2009)) shows some finite element analysis predicting the size of kinking as a function of actuator spacing. Since the actuator spacing in NEMO2 was about 20μm (Rodriguez Sanmartin et al. (2010)), it was expected that the kinking should be small. However, it is important to note that disagreement is already evident between this finite element analysis and the contemporaneous measurements shown in Figures 4.3 and 4.4. Whereas Figure 4.5 predicts kinks of several hundred nm for an actuator spacing of 100μm, Figures 4.3 and 4.4 show deviations of much more than even one micron.

Firstly, a 10.6μm interferometer was used to directly measure the surface height. This was not well suited to the task because of the high level of curvature, and the difficulty and expense of creating a nulling element for such a high power, aspheric mirror in the infrared band. Reasonable data were obtained with a ~10mm field of view over the join of two actuators in the center of the mirror (Figure 4.6). Figure 4.7 also shows several line

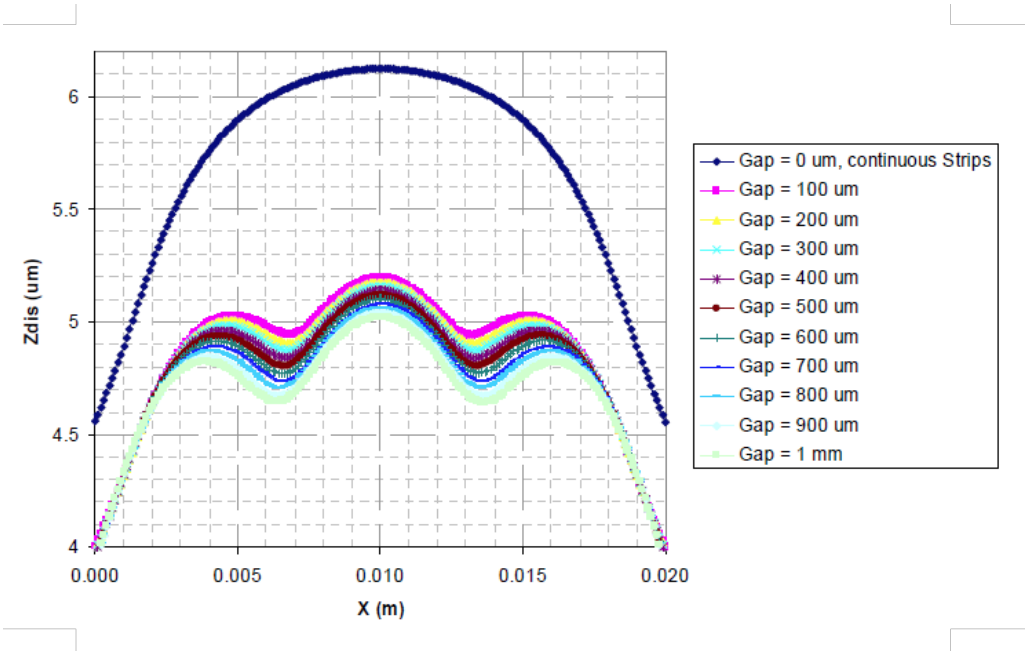

Figure 4.5. Finite element analysis of the effect of inter-actuator spacing on kink size (Zhang et al. (2009)). Extrapolation from this figure to the improved actuator spacing of 20μm produced for NEMO2 indicates that kinks should be below 100nm.

traces across this join at various actuator voltages, all with no visible kinking. However, the sensitivty of these measurements is fairly low. Figure 4.5 suggests that kinking should be present in NEMO2 at a level of something like 200nm across the actuator footprint; the field size of the interferometer (limited by the curvature of the mirror), coupled with the relatively long wavelength, means that this would be very difficult to see.

It is clear from Figures 4.6 and 4.7 that NEMO2 at least presents a substantial improvement over previous prototypes, which can be seen (e.g. Figure 4.4) to have kinks of $\sim$5μm amplitude. This would have been visible via interferometer so clearly there is some improvement. In an effort to exaggerate any print through which may be present, the measurements shown in Figure 4.7 were taken at different voltages. Flexing adjacent actuators in the same direction should exacerbate any problems, but revealed nothing. There are some features observed in Figure 4.6, but these are orthogonal to the actuator boundary and likely are artifacts caused by noise, or real features indicative of the generally poor surface of the mirror. At the level of sensitivity required for these measurements the interferometer is very sensitive to vibrational noise, which was hard to remove from the test environment. It is necessary in this context to be aware of the error budget of such mirrors, as it is not useful, beyond a point, to chase smaller and smaller errors. In this mindset, it was decided to test the general optical performance of NEMO2 and the capability of its actuators.

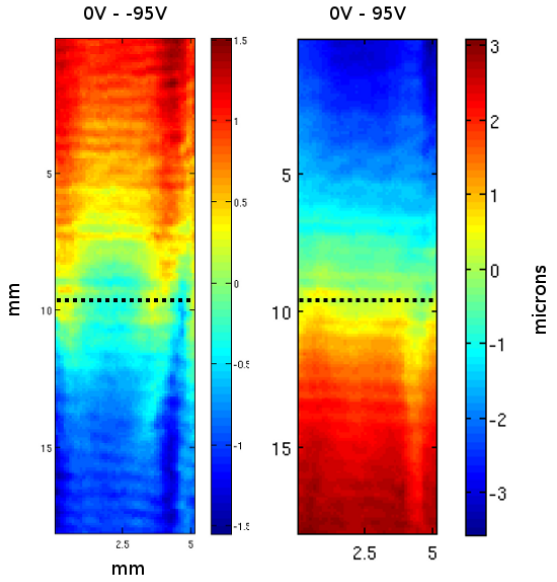

Figure 4.6. Effect of actuators on NEMO2. The sensitivity and field of view available with the interferometer mean that this is not a very good test, however it is enough to show a clear improvement over previous prototypes (Figure 4.4). This is a validation of the final gluing technique used, but the form of the mirror is still quite poor. There are some visible features which are orthogonal to the actuator boundary and thus probably have some other cause, but this measurement certainly rules out kinking at the micron level that was observed previously.

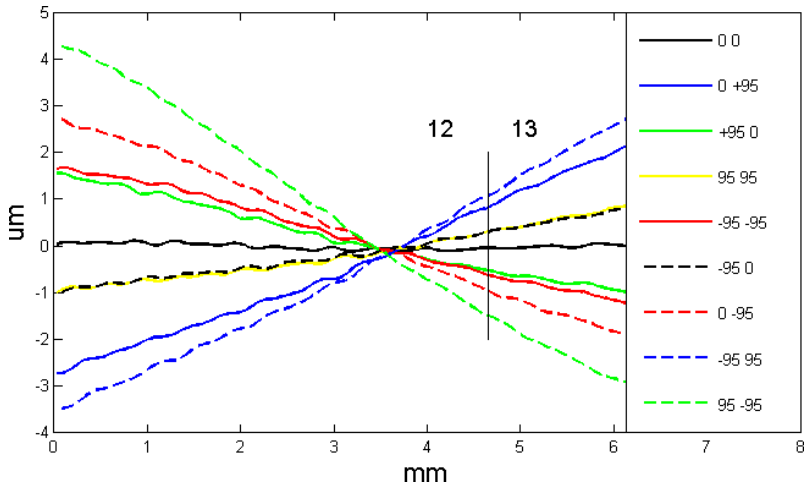

Figure 4.7. Effect of actuators on NEMO2 at various voltages across an actuator join. No 'kinks' are visible even under extreme actuation. This data is taken from averaged line profiles across interferometric scans.

4.4 Simulation

Before optical testing, it was decided to roughly simulate the output of a similar system in order to have an idea of the best (diffraction limited) focal spot that could theoretically be obtained with a 600nm laser. If the output of NEMO2 were much worse than this,

then it would be reasonable to test it with the same laser rather than with x-rays.

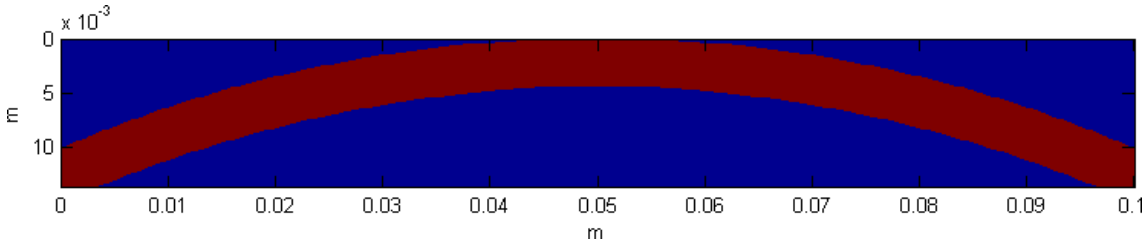

Figure 4.8. An aperture mask roughly simulating NEMO2 at 1° grazing incidence.

An aperture mask was created (Figure 4.8) to roughly simulate a 10cm × 30cm optic at 1° grazing incidence. The fourier transform was taken of this in Matlab to create an approximation of the ideal point spread function. From Figure 4.9 and 4.10, it can be seen that the full width half maximum (FWHM) of the focal spot should be around 0.1mm × 0.5mm.

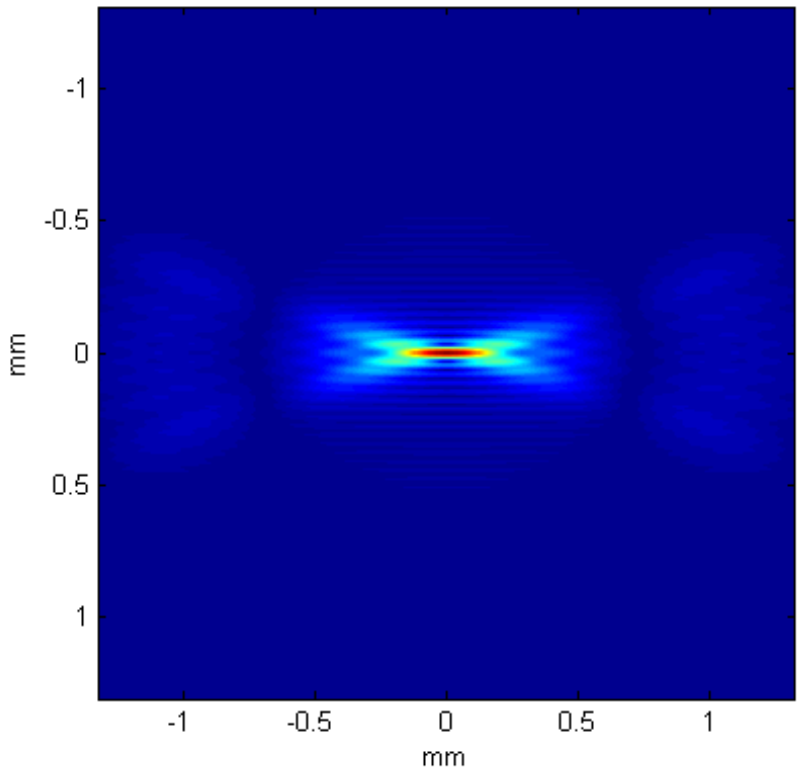

Figure 4.9. A simulation of the diffraction limited focal spot of NEMO2, created by taking the fourier transform of Figure 4.8.

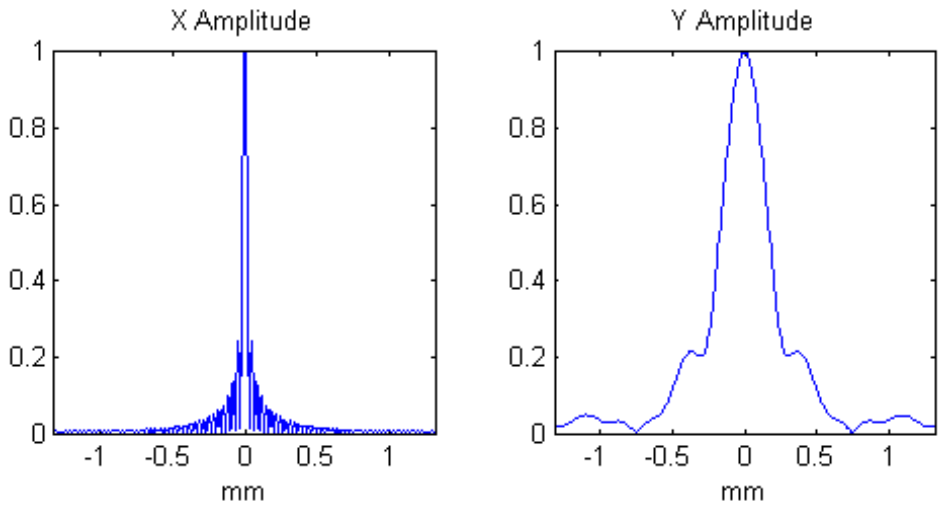

Figure 4.10. Orthogonal traces across the center of a simlated 'best case' PSF (Figure 4.9) showing the relative intensity.

4.5 Optical Testing

A test setup (see Figure 4.11) was created to allow NEMO2 to focus on a standard optical bench despite the very long focal length. By placing a pinhole within the focus of a parabolic mirror, a virtual image of a point source was created ∼24m away from NEMO2 with a 593nm laser. NEMO2 was placed at grazing incidence (∼1 degree) and the optical path was folded until the beam came to a focus about 4.5m away from the mirror. The focal spot (shown in Figure 4.12) was placed onto a piece of tracing paper, the rear side of which was then imaged using a Thorlabs USB camera. This was done because the focal spot itself was much larger than the sensor in the camera.

All of the test optics used were better than $\lambda/2$ across their surface, so were taken to contribute negligibly to errors in the system due to the much larger aberrations present in NEMO2. Images were captured with Python using the pyueye library, which is a wrapper for the uEye camera driver[1].

4.5.1 Control of NEMO2

The mirror was powered using a Starpoint Adaptive Optics High Voltage Amplifier and a simple digital to analogue (DAC) board controlled via parallel port, which allowed individual control of the actuators from within Python running on a laptop.

[1] https://code.google.com/p/pyueye/

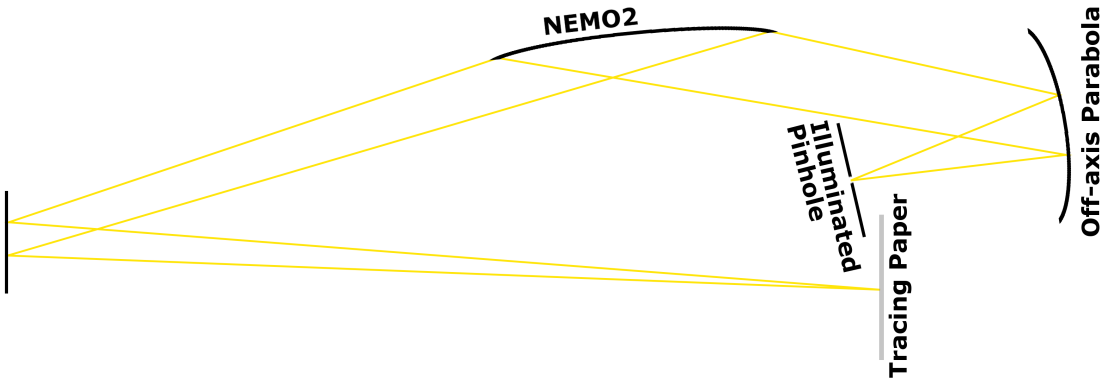

Figure 4.11. A visible light setup was created to characterise the focus of NEMO2 on a standard size optical bench.

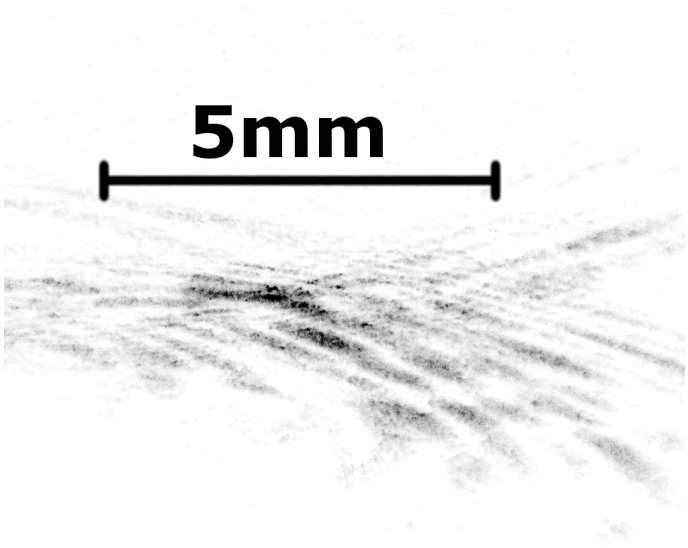

Figure 4.12. The focal spot from NEMO2 was imaged on tracing paper with the control system disconnected.

4.5.2 Simulated Annealing

A simulated annealing algorithm was written to try to blindly optimise the focal spot of the mirror by reducing the half energy width (HEW). Simulated annealing works by iterating through neighbouring states (in this case defined as 15V steps on an actuator) and probabilistically remaining in a state based upon its 'energy cost' and the 'temperature' of the system, which is gradually decreased. The energy cost in this case was proportional to the HEW (the radius of a circle which contains half of the energy of the focussed light). If the state is not adopted another one is tested; if it is, the chosen actuator remains at its new voltage and another actuator is randomly chosen and stepped up or down by 15V. This continues indefinitely and should converge eventually upon an ideal solution - the probabilistic approach is used so that the system does not become deterministically

stuck in local minima in the energy cost (HEW). This approach is useful when there are too many degrees of freedom to explicitly check every possible state of a system, and was chosen in this case because the algorithm is easy to implement and optimisation time was not a factor; the aim was just to see how much improvement could be achieved using the actuators.

The acceptance probability was defined as a, where:

$$a = e^{\frac{c_{new} - c_{old}}{T}} \tag{4.1}$$

where c_{old} and c_{new} are the energy costs of the previous and new states respectively and T is the system 'temperature'. After determining a, a random number is rolled between 0 and 1, and if the number is $< a$ then the new state is accepted.

There were some issues with this approach, due mostly to the very poor focus of NEMO2 (see Figure 4.12). As the actuators moved, many of them would displace light entirely outside of the part of the focal plane being imaged by the camera. This often resulted in a decrease of the HEW since the overall light being detected on the focal plane was decreased. To counteract this, an energy cost was added into the simulated annealing algorithm to track the total irradiance at the focal plane. Camera exposure was manually set at a level to avoid saturation whilst still being sensitive enough to see outlying features of the PSF.

The results of the simulated annealing algorithm can be seen in Figure 4.13. A repeatable improvement of about 30% was achieved for HEW, but the number of degrees of freedom and the settling time of the actuators (due most likely to the high output impedance of the amplifier and capacitance of the actuators), meant that simulated annealing runs were prohibitively long.

Figure 4.14 shows a comparison between the unactuated focal spot and that produced by the best form found from the annealing. There is a clear improvement, although in absolute terms the focus is still very bad.

In order to reduce the effects of hysteresis, a dithering algorithm was used to approach target voltages, consisting of a decaying sinusoid beginning at the maximum and minimum actuator voltages. The effects of hysteresis in NEMO2 are very significant. This is often a problem in PZT actuators and is analogous to slack or backlash in a mechanical system, except that the deviation is dependent upon the signal size (which is a why an oscillating signal with decaying amplitute works to counter it). It is thus often presented as the ratio of the width of the hysteresis curve to the signal. Figure 4.15 shows a measurement of

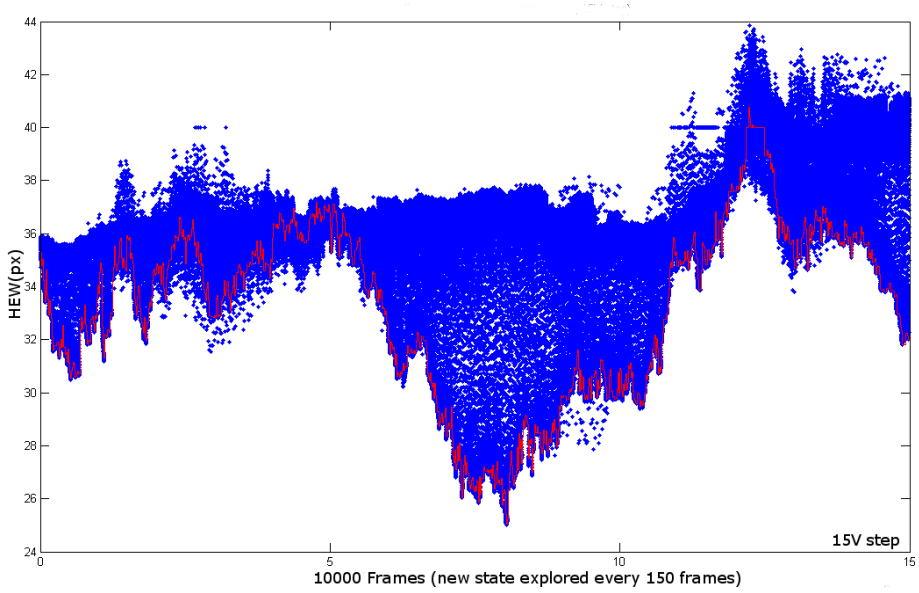

Figure 4.13. Results of simulated annealing of NEMO2 form. Some improvement was achieved, but settling time of actuators/electronics led to very long runs being required. Blue points mark the HEW of explored states, whilst the red line follows the HEW of states actually adopted by the mirror.

the HEW when actuating a set of actuators between ±75V and is illustrative of a typical hysteresis curve.

4.5.3 Conclusions

After analysing these results it was decided that time would be better spent on creating a new prototype using different materials and processes. The form of NEMO2 is very bad and cannot be corrected using actuators alone. Although the measures taken to avoid actuator print-through on the optical surface appear to have worked to some extent, the optic itself still leaves much to be desired. As mentioned in Chapter 3, electroplated optics are no longer being proposed for high resolution grazing incidence optics, since stresses created during electroplating make it very difficult to create an accurate form.

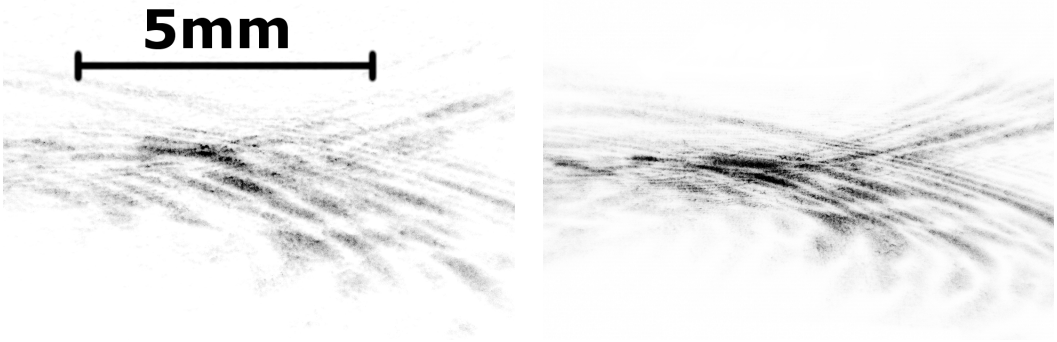

(a) Un-actuated focus. (b) Post-annealing.

Figure 4.14. An improved focus was obtained through simulated annealing.

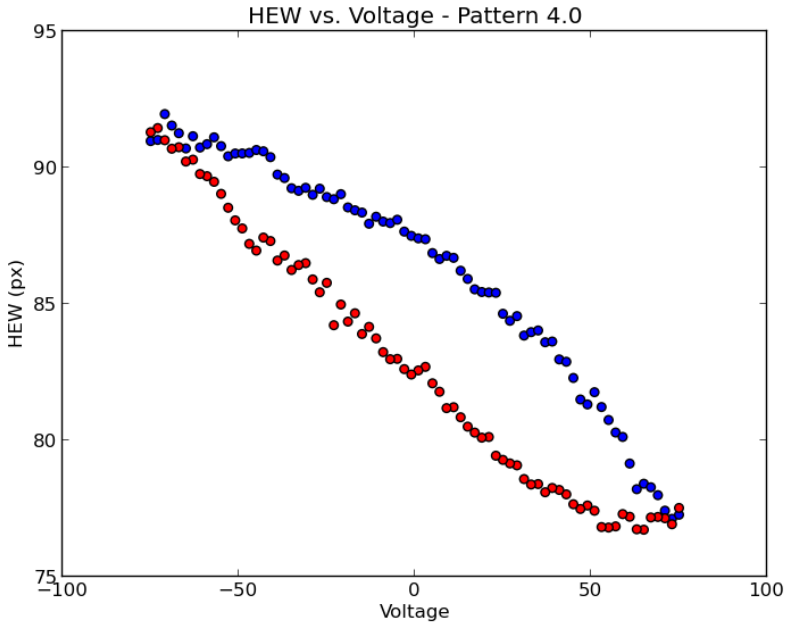

Figure 4.15. Hysteresis is clearly visible in the effect of the actuators on the half energy width.

Chapter 5

Ray Tracing

In order to evaluate the importance of different optical defects in grazing incidence systems, it was decided to develop a simple raytracing code. There are several commercially available software packages that perform raytracing analysis (e.g. Zemax) however most of these lack the ability to import arbitrary surfaces. For this reason a code was developed with the intention that it could be easily expanded to simulate the optical performance of real surfaces, given data on the surface height. Raytracing in x-ray optics is a fairly simple problem as diffraction effects can usually be ignored and the calculation easily becomes 'embarrassingly' or trivially parallel.

5.1 Initial Surface Generation

A rectangular section of a parabolic surface is generated with variable projected length, width and offset from the origin. The surface height is evaluated along a cartesian grid, with surface normals found analytically through differentiation.

A general three dimensional parabola as shown in Figure 5.1 can be described in cartesian co-ordinates by

$$z(x, y) = ax^2 + by^2 + c$$

which can be rearranged to:

$$x(z, y) = \sqrt{\frac{z - by^2 - c}{a}}$$

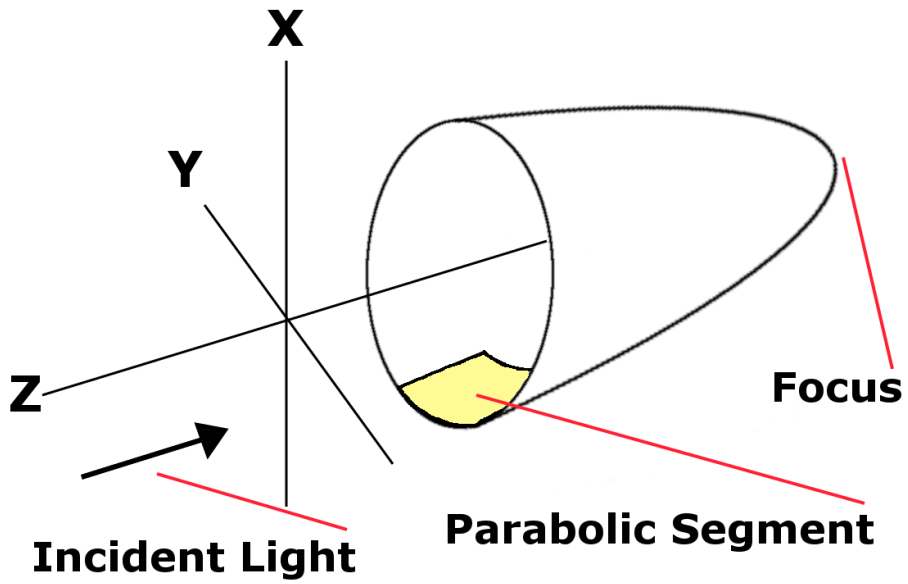

Figure 5.1. A diagram showing the internal layout of the x,y,z axes used within the code to generate the parabolic mirror segment.

if we define z as the optical axis and x as the 'surface height' of the mirror. Careful limits on y and z, which are anyway necessary to produce a sensible mirror, prevent x from becoming imaginary or multivalued.

Partial derivatives can be found for $\frac{\delta x(z,y)}{\delta y}$ and $\frac{\delta x(z,y)}{\delta z}$:

$$\frac{\delta x(z,y)}{\delta y} = \frac{-by}{a\sqrt{\frac{-by^2-c+z}{a}}}$$

$$\frac{\delta x(z,y)}{\delta z} = \frac{1}{2a\sqrt{\frac{-by^2-c+z}{a}}}$$

The arctangent of these derivatives can then be used to calculate the tip $(\delta x(z,y)/\delta z)$ and tilt $(\delta x(z,y)/\delta y)$ of each mirror element, and these values can be used to describe a surface normal vector $\mathbf{N}$:

$$\mathbf{N} = \begin{pmatrix} \text{-cos}(\frac{\delta x(z,y)}{\delta y})\text{sin}(\frac{\delta x(z,y)}{\delta z}) \\ \text{cos}(\frac{\delta x(z,y)}{\delta z})\text{sin}(\frac{\delta x(z,y)}{\delta y}) \\ \text{cos}(\frac{\delta x(z,y)}{\delta z})\text{cos}(\frac{\delta x(z,y)}{\delta y}) \end{pmatrix}$$

Given the surface normal, it is trivial to calculate the vector of the reflected ray if the incident vector is known. From Figure 5.2:

$$\mathbf{R}_r = \mathbf{N}(\mathbf{R}_1 \cdot \mathbf{N}) + \mathbf{a}$$

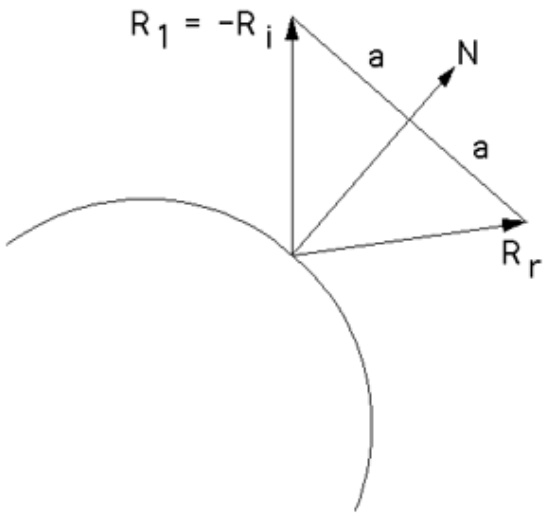

Figure 5.2. A diagram explaining how to calculate the direction of a reflected ray ($\mathbf{R}_r$) given an incident ray ($\mathbf{R}_i$) and the surface normal ($\mathbf{N}$) [2]

$$\mathbf{R}_1 + \mathbf{a} = \mathbf{N}(\mathbf{R}_1 \cdot \mathbf{N})$$

which can be rearranged to:

$$\mathbf{R}_r = 2\mathbf{N}(\mathbf{R}_1 \cdot \mathbf{N}) - \mathbf{R}_1$$

then we can substitute $\mathbf{R}_1$ for $-\mathbf{R}_i$:

$$\mathbf{R}_r = \mathbf{R}_i - 2\mathbf{N}(\mathbf{R}_1 \cdot \mathbf{N}) \tag{5.1}$$

Where $\mathbf{R}_r$ is the reflected vector, $-\mathbf{R}_1 = \mathbf{R}_i$ is the incident vector, $\mathbf{N}$ is the surface normal and $\mathbf{a}$ is as shown in Figure 5.2. $\mathbf{R}_1$ and $\mathbf{a}$ are created and labelled only to simplify this derivation.

A ray can then be generated for each surface point such that the number of rays depends on the resolution of the generated surface. Every ray is assumed to be incident directly along the z axis, corresponding to perfectly collimated light. Combined with the x, y, z coordinate of the relevant surface element, the rays are propagated towards a screen of which the user can control the position, size and resolution. Rays are weighted according to the 'aperture' (projected area along the optical axis) of the surface element from which they were created, and are summed into pixels on the screen using path differences to keep track of their phase. The user is able to visualise all of these elements in a 3D plot within MATLAB as shown in Figures 5.3, 5.4 and 5.5.

[2] Figure taken from http://paulbourke.net/geometry/reflected/

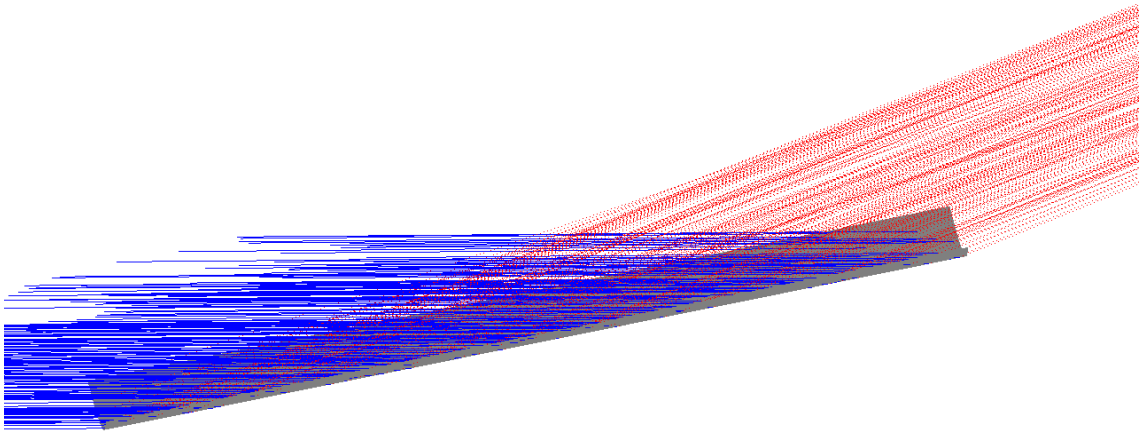

Figure 5.3. A close up image of the generated surface showing incident (blue) and reflected rays (red). Incident rays are aligned along the optical axis and generated just for visual confimation of angles. The surface is shown in grey although it is mostly obscured by rays in this example.

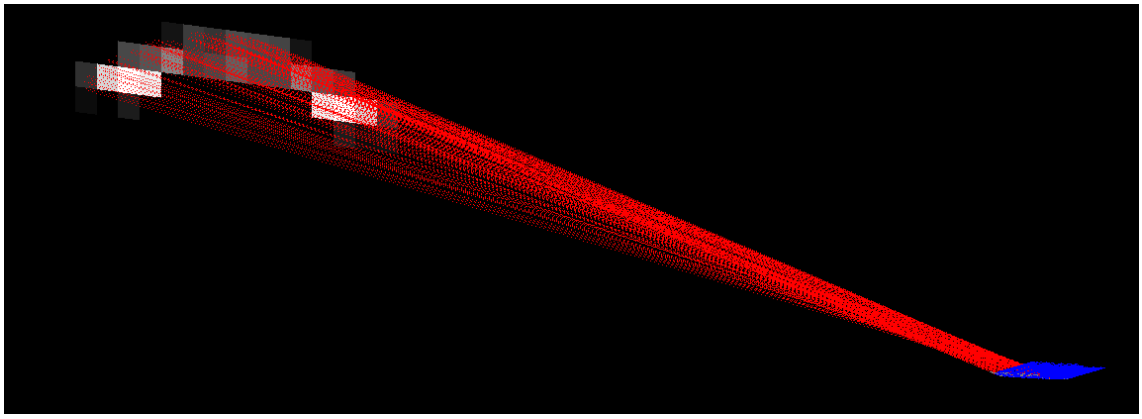

Figure 5.4. An image with distorted perspective which also shows the screen element on which reflected rays are captured and summed. The surface in this image is at an extreme angle so the rays are very out of focus. The screen was made very large to catch the divergent rays, so here appears very low resolution.

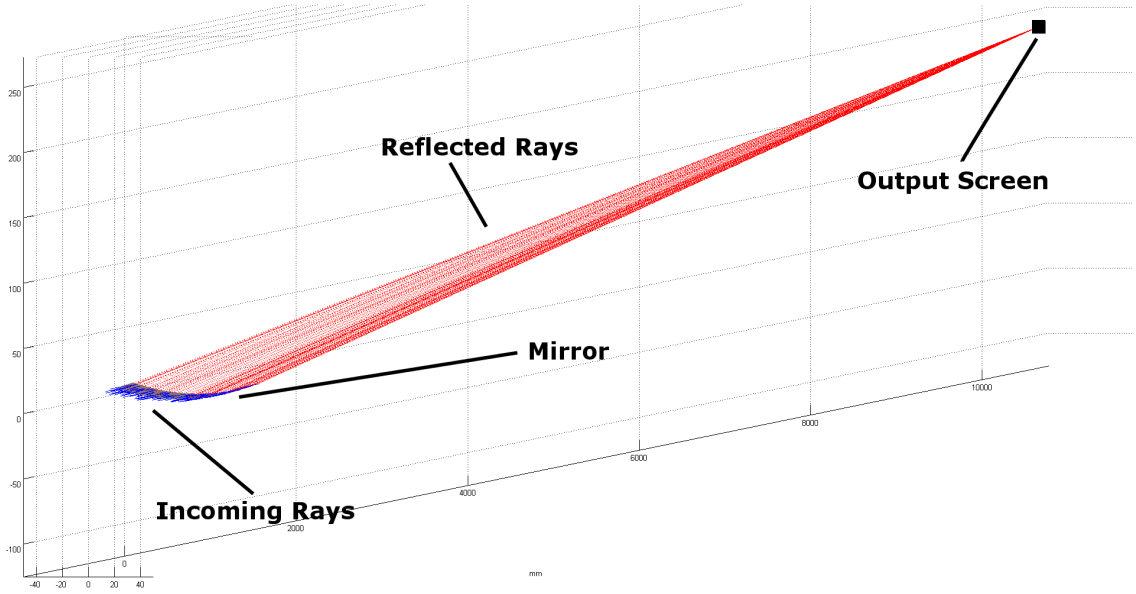

Figure 5.5. A 3D image showing the rays, surface and screen in normal use. This is a $\sim$ 10×30cm optic with a 4.5m focal length; the image is compressed along the optical axis.

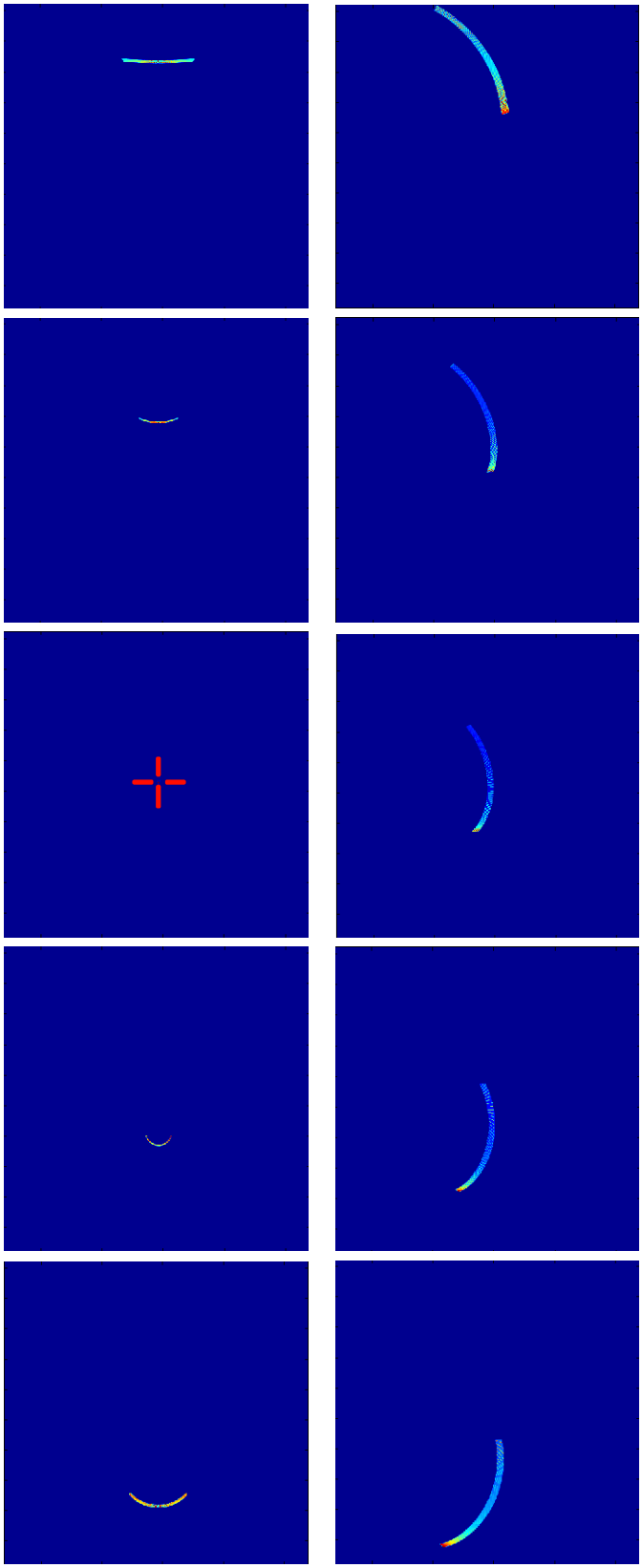

Figure 5.6. Images of the focal spot of a 4.5m focal length parabola (left column) at -2mm, -1mm, 0mm, +1mm and 2mm with respect to the nominal focal plane. The right hand column shows rays at the same position but the simulated mirror has a $\sim 1\mu$m twist applied. Field of view is 10 arcseconds. In images with a very small focal spot the red crosshair is used to aid identification

5.2 Perturbations

The code was extended to allow the addition of rectangularly derived zernike polynomials (He et al. (2010)) to the base parabolic surface. Lots of different basis sets could have been chosen for this purpose, these were used mostly out of interest. The first nine of these polynmials are shown in Figure 5.7. Gradients were found for these polymials and included in the surface normal calculation described in Section 5.1, allowing their effect on reflected rays to be calculated analytically. Only the first six of these have been included in the code so far, and of these only modes four, five and six are interesting. The first mode does nothing, and modes two and three are better represented by explicitly adding tip (rotation about the short axis) and tilt (rotation about the long axis) errors to the simulated mirror, which is handled separately by the code. Rotation errors within the 'plane' of the mirror were not investigated.

Figure 5.8 shows the surface height of a simulated 4.5m focal length paraboloid with 150mm radius of curvature. These dimensions were chosen to be similar to slumped glass prototypes being made by other groups.

Figure 5.9 shows the effect on the focal spot of 1 arcsecond of additional tip and 1 arcminute of additional tilt. The mirror is much more sensitive to tip errors. Intuitively this makes sense since tilt errors essentially amount to a translation of the focal spot around a circle with the same radius of curvature as the mirror segment, whereas tip errors displace the focal spot with an optical lever the length of the focus (4.5m) and also defocus the image.

Figure 5.10 shows the effects of zernike modes four, five and six on the focal spot of the same mirror.

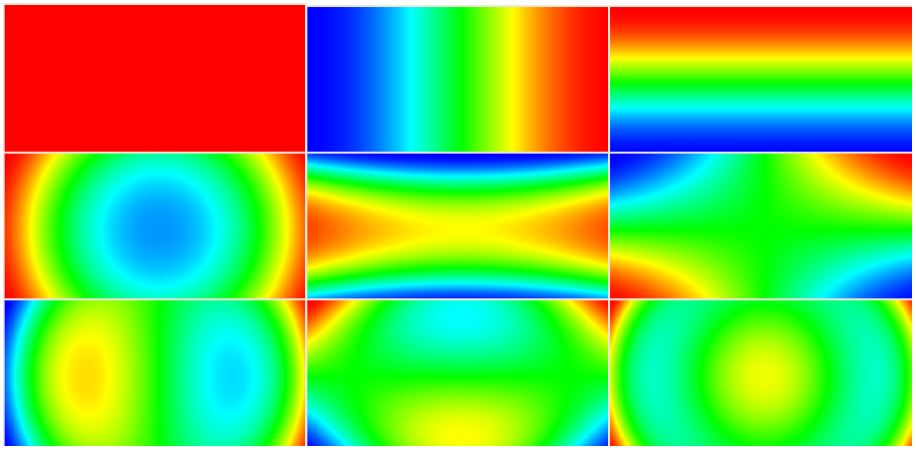

Figure 5.7. The first nine rectangular zernike polynomials derived by He et al. (2010)

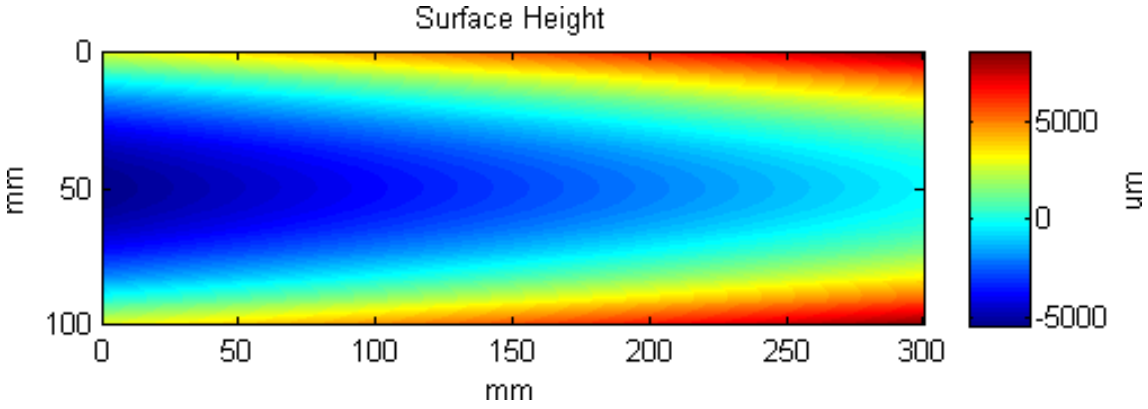

Figure 5.8. 150mm radius of curvature, 4.5m focal length paraboloid generated using the raytracing software. This should be a reasonable approximation to a Wolter I system, but adding that surface explicitly instead of a parabola would be a very useful feature. This would be quite easy as it simply requires the addition of another hyperbolic suface and a new calculation to see where the rays intersect for the second reflection.

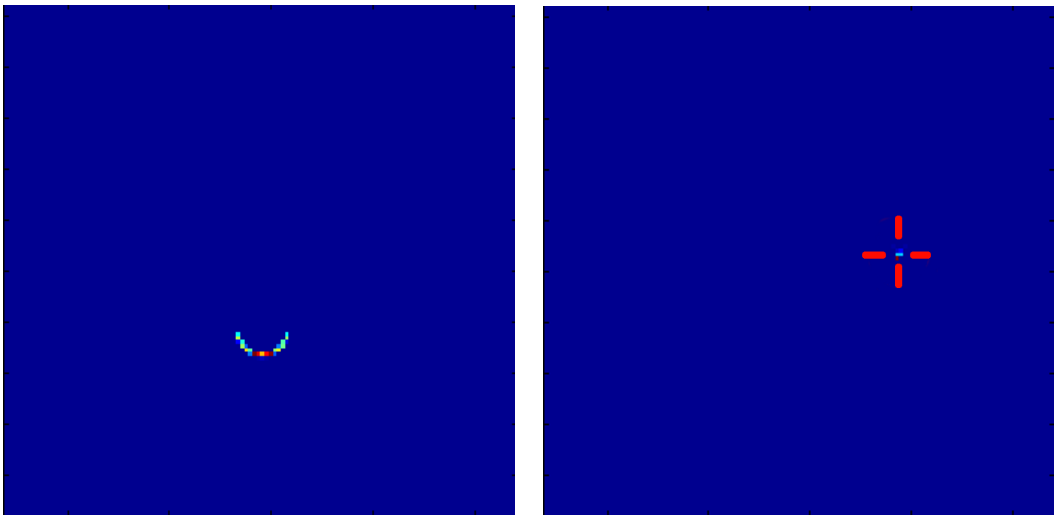

Figure 5.9. The effects of 1 arc**second** gross tip (left) and 1 arc**minute** tilt (right, red crosshair indicating the position of the focal spot). The mirror is roughly 60x more sensitive to tip errors. Field of view is 10 arcseconds.

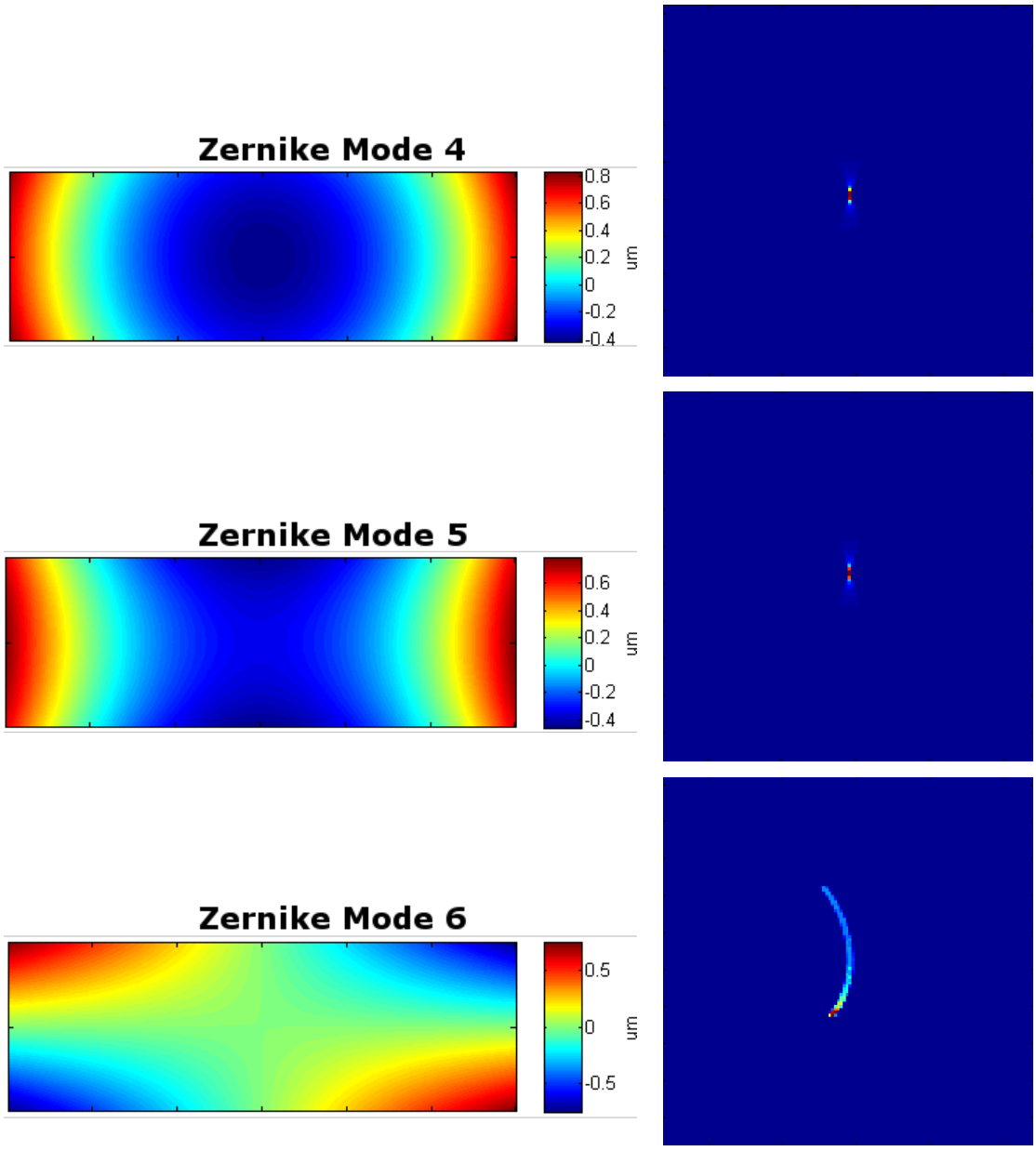

Figure 5.10. The optical effects of three different aberrations with magnitudes of $\sim 1\mu$m. The base surface is that shown in Figure 5.8, the aberrations are shown here in the left hand column. The field of view shown at the focal plane on the right is 10 arcseconds. Clearly for sub-arcsecond resolution the error budget is sub-micron. Although the focal spot in the image of the sixth zernike mode appears much more diffuse the peak is actually higher, making the sensitivity to the different modes comparable in terms of resolution.

5.3 Summary

We developed a raytracing code which allows the user to visualise an optical system with a single parabolic surface and extract the focus rays at any point. The size and radius of curvature of the mirror can be set by the user and it is possible to add gross tip and tilt errors as well as several different rectangular zernike modes. There is great potential for expanding this code to allow optical simulation of arbitrary surfaces and systems with multiple reflections.

From Section 5.2 it is already possible to get a good idea of the error budget and sensitivity to different modes of a 4.5m focal length grazing incidence parabolic mirror. It is clear that aberrations must be sub-micron for a mirror of this focal length to have sub-arcsecond resolution, and it is also clear from Figure 5.9 that tilt and especially tip must be carefully controlled during mounting. Although Figure 5.10 seems to imply that the mirror is more sensitive to the sixth zernike mode, this is an artefact caused by the scaling of the contrast between pixels. Because there is no diffraction or dithering of rays in the code, numerical issues can arise depending on the pixel size of the screen element at the focus.

Improving this pixel summing would be a useful first improvement to the code. Another obvious improvement would be the explicit inclusion of true Wolter I surfaces. Following this, it would be interesting to tie this code together with the work done in Chapters 7 and 6 on deflectometry and simulation of actuator influence functions. It would be useful to measure the surface of a real test optic with deflectometry (see Chapter 7) and then simulate it using the raytracing code and use finite element analysis to test different strategies for correction.

The lessons learned during developing and testing this code were employed during the prototype design phase described in the next chapter, most notable the great sensitivity to tip errors.

Chapter 6

Prototype Design & Simulation

This chapter explains the process and decisions which went into designing the new active mirror prototype using Macro-Fibre Composite (MFC) actuators and commercially available thin glass. Macro-fibre composites consist of a layer of PZT fibres sandwiched between two electrode layers held in a polyimide package. These are a relatively new technology which can provide a large range of motion along with much greater flexibility (physically as well as in application) over monolithic ceramic actuators.

6.1 Finite Element Analysis of MFC Actuators

In order to simulate the effects of different actuator arrangements it was necessary to first simulate the effect of an MFC actuator. A basic diagram of the two main types of MFC is shown in Figure 6.1. d_{33} actuators (left) were chosen for the prototype since they have a greater range of motion for an equivalent voltage. These actuators consist of interdigitated

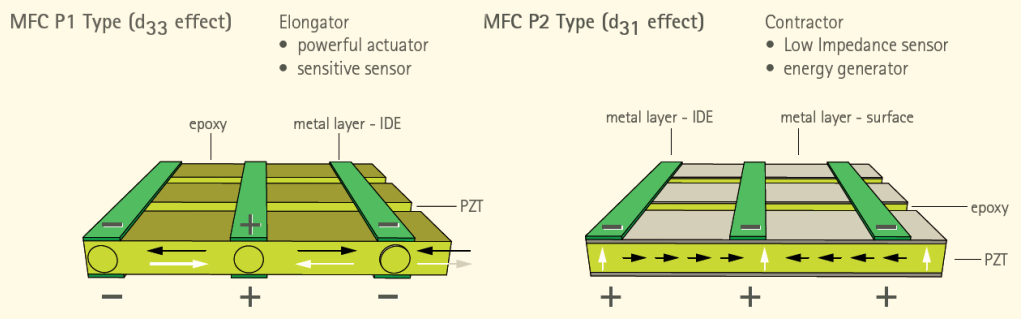

Figure 6.1. A diagram of the insides of MFC actuators taken from www.smart-material.com. P1 type actuators (left) were used in the construction of this prototype due to their greater range of motion.

Low-field (|E| < 1kV/mm), unbiased-operation piezoelectric constants:		
d_{33}*	4.0E + 02 pC/N	4.0E + 02 pm/V
d_{31}**	-1.7E + 02 pC/N	-1.7E + 02 pm/V
Free-strain* per volt (low–field – high–field) for d_{33} MFC (P1)	~ 0.75 – 0.9 ppm/V	0.75 – 0.9 ppm/V
Free-strain* per volt (low–field – high–field) for d_{31} MFC (P2)	~ 1.1 – 1.3 ppm/V	~ 1.1 – 1.3 ppm/V
Free-strain hysteresis*	~ 0.2	~ 0.2
DC poling voltage, Vpol for d_{33} MFC (P1)	+1500 V	+1500 V
DC poling voltage, Vpol for d_{31} MFC (P2)	+450 V	+450 V
Poled capacitance @ 1kHz, room temp, Cpol for d_{33} MFC (P1)	~ 0.30 nF/cm²	~ 1.94 nF/in²
Poled capacitance @ 1kHz, room temp, Cpol for d_{31} MFC (P2)	~ 7.8 nF/cm²	~ 50 nF/in²
Orthotropic Linear Elastic Properties (constant electric field):		
Tensile modulus, E1*	30.336 GPa	4.4E + 06 psi
Tensile modulus, E1**	15.857 GPa	2.3E + 06 psi
Poisson's ratio, v12	0.31	0.31
Poisson's ratio, v21	0.16	0.16
Shear modulus, G12 (rules-of-mixture estimate)	5.515 GPa	8.0E + 05 psi

Figure 6.2. An extract from the MFC datasheet from smart-material.com showing the piezoelectric parameters of their d_{31} actuators. *along fibre axis **not along fibre axis

electrodes which create an electric field along the length of the fibres, the same direction along which they are poled. Figure 6.2 shows an extract from the MFC datasheet from Smart Material GmbH where the actuators were purchased.

Fully simulating an MFC actuator in FEA would be very difficult, since each poled region of every fibre would have to be treated as a separate actuator, and there are many thin layers of glue, polyimide and copper which would be difficult to mesh adequately. Instead, an approximate approach was chosen whereby the COMSOL piezoelectric toolbox was used to create a new piezoelectric material with the bulk properties of an MFC actuator. Using the information in Figure 6.2, a compliance matrix S_E, piezoelectric coupling matrix d and permittivity matrix ϵ_T/ϵ_0 were created. These are shown below. Axis ordering for all matrices is $xx, yy, zz(, yz, xz, xy)$, fibres are along x axis, electric field is applied along the z axis:

$$S_E = \begin{pmatrix} 0.3 & -0.1 & -0.1 & 0 & 0 & 0 \\ -0.1 & 0.6 & -0.1 & 0 & 0 & 0 \\ -0.1 & -0.1 & 0.6 & 0 & 0 & 0 \\ 0 & 0 & 0 & 0.7 & 0 & 0 \\ 0 & 0 & 0 & 0 & 0.8 & 0 \\ 0 & 0 & 0 & 0 & 0 & 0.8 \end{pmatrix} \times 10^8 \text{ Pascal}^{-1}$$

$$d = \begin{pmatrix} 0 & 0 & 0 & 0 & 0 & 0 \\ 0 & 0 & 0 & 0 & 0 & 0 \\ -4 & 1.7 & 1.7 & 0 & 0 & 0 \end{pmatrix} \times 10^{-10} \text{ Coulomb/Newton}$$

$$\frac{\epsilon_T}{\epsilon_0} = \begin{pmatrix} 1475 & 0 & 0 \\ 0 & 1475 & 0 \\ 0 & 0 & 1300 \end{pmatrix}, \epsilon_0 = 8.854 \times 10^{-12} \text{ Farad/Meter}$$

With this information COMSOL is able to solve the boundary equations and incorporate the material into a piezoelectric FEA simulation. Local co-ordinate systems are used to place the MFC material in different orientations within a simulation. The results of this can be seen in Figure 6.3 and onwards throughout this chapter.

6.2 Mounting

The mounting of an active mirror dramatically affects its response. It is clear to see from finite element analysis that, with very thin mirrors, the best results are obtained when the mirror is as unconstrained as possible, or when the actuator is bridging between two constrained areas of the mirror. This is shown in the comparison between Figures 6.3 and 6.4 which were simulated in COMSOL using the piezoelectric toolbox, and a custom material with the actuator. Simulation of the actuator behaviour is discussed in Section 6.1.

If the mirror is overconstrained then the large stress created by even very small strain causes the actuator influence functions to become very localised as in Figure 6.3. This introduces higher order aberrations which cannot be removed by adjusting the actuators. Reducing these constraints results in a smoother influence function and a greater range of motion for a given voltage, as shown in Figure 6.4.

The mounting strategy also has a large effect on the viability of the mirror for use in a stacked optic and on the ease of construction and integration. This is discussed further in Section 6.6.

In the designing of the prototype, two main configurations were considered. The first is bonded to a rigid block along the entirety of an edge, the second is bonded to a rubber block in a 3x3mm area at each corner. These topologies represent an unconstrained (in one axis) and reasonably constrained mirror respectively, and are shown in Figure 6.5. The Young's modulus of the rubber blocks was taken to be 0.2GPa, which corresponds to medium-stiff RTV rubber. These designs are greatly simplified, but the intent was to

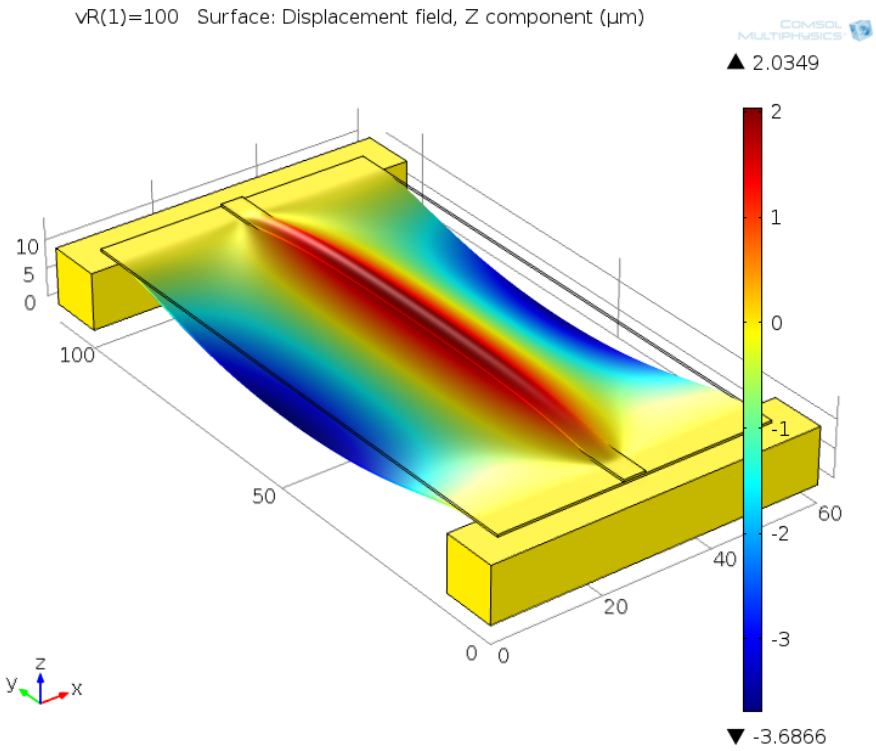

Figure 6.3. Over-constraint of the mirror causes very localised influence functions. In this model the two shorter ends of the glass are attached to fixed, rigid blocks, meaning that the displacement is very small despite the large (100V) potential. The influence function of the actuator is not useful for correcting low order aberrations.

distinguish between the two mounting paradigms.

The advantage of the mounting scheme shown in Figure 6.5a is that most of the mirror is relatively unconstrained so large shifts can be achieved with moderate actuator voltages. It is possible to adjust the gross tip and tilt of the mirror by introducing a curve or twist near the support. We know from Chapter 5 that grazing incidence mirrors are very sensitive to tip errors, so it may be useful to be able to make corrections after assembly. The mount can also be machined accurately to constrain one edge of the mirror to the correct radius of curvature. The downside is that most of the mirror is not well supported mechanically; some kind of temporary damping system would likely be needed to support the free end of the optic during launch. The bonding area is also relatively large and glue shrinkage would become a problem. In the configuration shown in Figure 6.5a, the mount also interferes with the leading edge of the optic, meaning that the separation between glass segments would have to be at least the mount thickness, plus the projected aperture of the lower segment. This quickly becomes a problem when stacked optics are considered; machining tolerances also become an issue if the mount is made too thin.

The mounting arrangement shown in Figure 6.5b has several advantages. Firstly, the

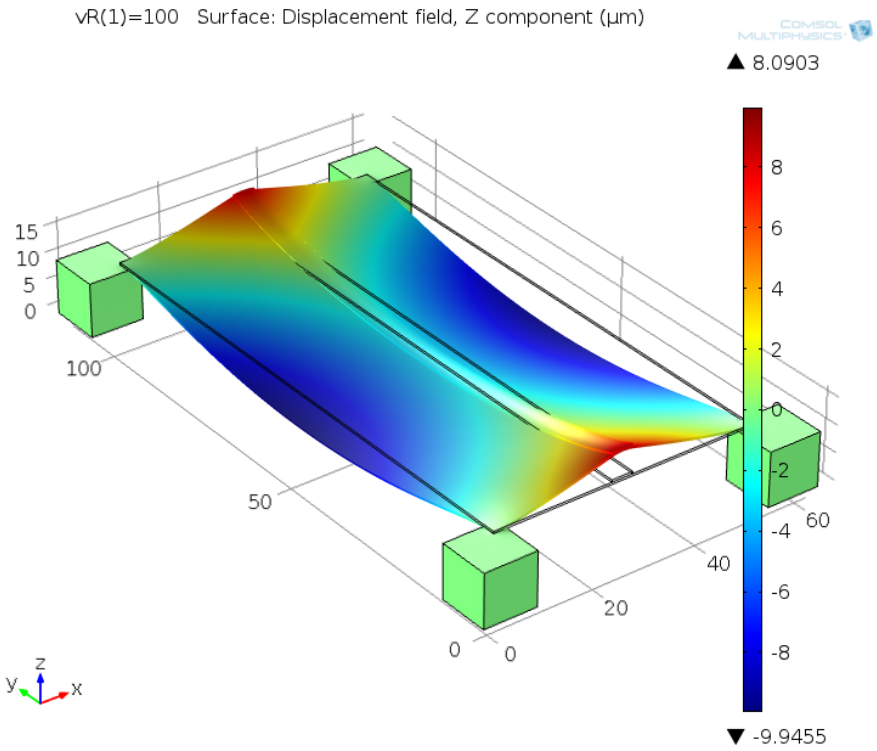

Figure 6.4. Minimal constraints on the glass allow the influence function to expand compared to Figure 6.3. The corner supports shown here have a Young's modulus of 0.2GPa, which is a middling value for RTV rubber.

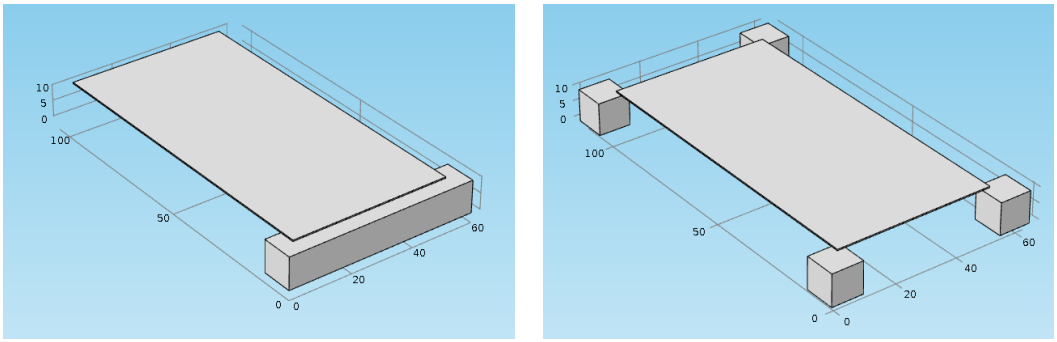

(a) Single edge support. (b) Corner supports.

Figure 6.5. Two different mounting schemes were considered.

mirror is better supported mechanically and should survive transport and launch more easily. Constraining all four corners also forces the gross tip and tilt of the mirror to be set during integration, which may or may not be an advantage. The clear disadvantage is that the extra constraints on the mirror make it harder to achieve large corrections, meaning that initial manufacture of the mirror (and stresses on the mirror during integration) must be better controlled.

Examples of these divergent approaches can be seen in the literature in Civitani et al. (2011) and McClelland et al. (2013) respectively. Civitani et al. deliberately overconstrain

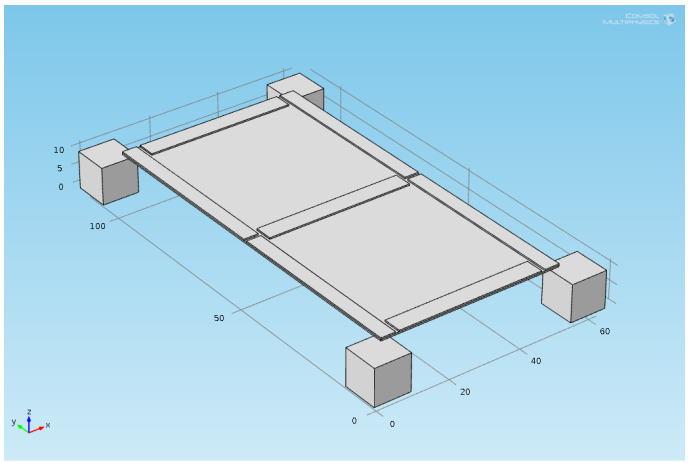

Figure 6.6. Example actuator placements. These produce the influence functions shown in Figure 6.7.

the mirror during integration by using the slumping mandrel as a form whilst gluing the mirror to the previous layer. Glass 'ribs' are placed between each optic to hold the shape and glue gaps are used to absorb mechanical tolerances and thickness variations. Measurements are taken of the alignment and mirror surface during integration and curing. Glue shrinkage is still a concern with this approach, although the effect is not additive between layers.

In contrast, McClelland et al. attempted the opposite approach: the glass is glued as lightly as possible at six edge points, paying close attention to glue shrinkage. McClelland et al. were able to achieve a better focus with this method, but the mirror is less structurally stable than the prototype produced by Civitani et al. and the method is arguably less scalable. However, this mounting strategy would work well with active mirrors and is similar to the approach shown in 6.5b.

Both of these topologies were simulated under actuation with different actuators arrangements, the results of which are shown in Section 6.4. Sections 6.4 and **??** explain the steps taken to make this possible.

6.3 Singular Value Decomposition

This is a general overview of the Singular Value Decomposition (SVD) technique used to find control matrices for the prototype mirror, and to predict the ability of various designs to assume different shapes. Although the mathematics in this section is completely general, the images shown use data from a corner-supported prototype design with seven independent actuators; this design is shown in Figure 6.6.

The influence functions for this prototype are shown in Figure 6.7. These are found for

the simulated prototype using finite element analysis in COMSOL, with the MFC actuator approximation described previously in Section 6.1.

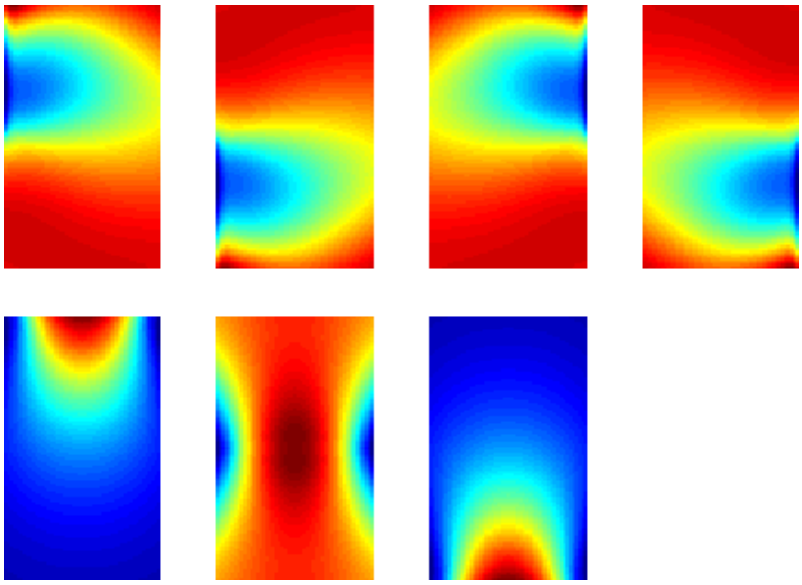

Figure 6.7. Actuator influence functions found using FEA for the prototype shown in Figure 6.6

A continuous surface can be described by a two dimensional matrix $\mathbf{X}$, where each matrix cell refers to the average height of a corresponding area on the surface. $\mathbf{X}$ can be thought of as the result of multiplying an interaction matrix ($\mathbf{I}$) with a control matrix of voltage signals ($\mathbf{v}$):

$$\mathbf{X} = \mathbf{I}\mathbf{v} \tag{6.1}$$

This can be further generalised such that $\mathbf{v}$ is a two dimensional matrix of different combinations of signals, and $\mathbf{X}$ encapsulates the surfaces output by these various combinations. The aim here is to find the inverse of $\mathbf{I}$, which can be used to find $\mathbf{v}$ (the control voltages) to produce an arbitrary surface:

$$\mathbf{v} = \mathbf{I}^{-1}\mathbf{X} \tag{6.2}$$

A 'poke' matrix is first created by moving each actuator in turn with a 50V signal, such that

$$\mathbf{v} = \begin{pmatrix} 1 & 0 & 0 & 0 \\ 0 & 1 & 0 & 0 \\ 0 & 0 & 1 & 0 \\ 0 & 0 & 0 & 1 \end{pmatrix}$$

This produces the influence functions shown in Figure 6.7.

The mirror surface is sampled over a matrix of points, the columns of which are then

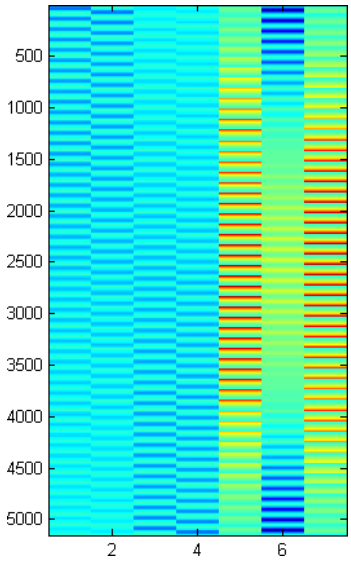

Figure 6.8. The influence functions produced by the poke matrix are stacked into columns to create the input matrix, $\mathbf{X}$. In the case of the poke matrix ($\mathbf{v}$), $\mathbf{X}$ is equivalent to $\mathbf{I}$.

stacked to produce $\mathbf{X}$; an image of this matrix is shown in (Figure 6.8). Each column in $\mathbf{X}$ refers to the output from a different row (actuator combination) in $\mathbf{v}$, which in the case of a poke matrix is just a single actuator. Because $\mathbf{v}$ is now just a unit matrix, Equation 6.1 simply becomes $\mathbf{X} = \mathbf{I}$.

The MATLAB svd() function is used on $\mathbf{X} = \mathbf{I}$:

$$\text{svd}(\mathbf{I}) = [\mathbf{U}, \mathbf{S}, \mathbf{V}'] \tag{6.3}$$

Just as $\mathbf{X}$ contains a stack of input influence functions in columns, $\mathbf{U}$ (Figure 6.9a) now contains the different orthogonal modes of the system stacked into columns. These can be extracted and are shown in Figure 6.10. Figure 6.9b shows $\mathbf{S}$ which contains the singular values of $\mathbf{X}$, relating to how accurately the system expresses the corresponding orthogonal mode. Figure 6.9c shows $\mathbf{V}'$, which gives the actuator voltages required to express the related mode.

From $\mathbf{U}$, $\mathbf{S}$ and $\mathbf{V}'$ it is possible to find the pseudo-inverse of $\mathbf{I}$:

$$\mathbf{I}^{-1} = \mathbf{V}\mathbf{S}^{-1}\mathbf{U}' \tag{6.4}$$

Given $\mathbf{I}^{-1}$, it is possible to use Equation 6.2 to find the control matrix $\mathbf{v}$ for any arbitrary surface. The control matrix produced by Equation 6.2 produces a least-squares fit to the input surface under the assumption of actuator linearity, by using a sum of orthogonal modes. It is clear to see in Section 6.4 that some arrangements are much better at

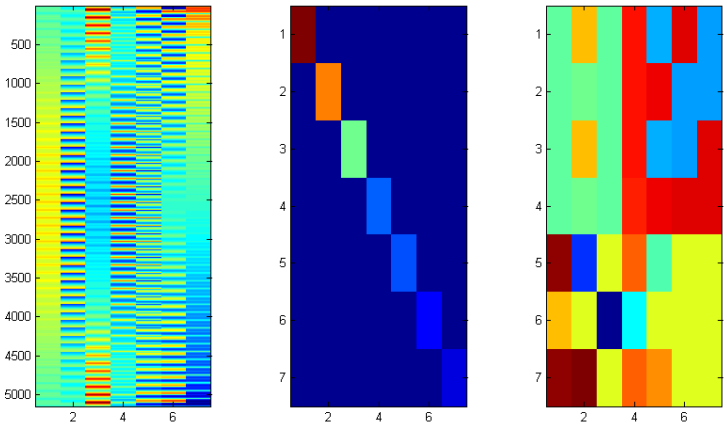

(a) **U** (b) **S** (c) **V′**

Figure 6.9. Matrices produces from using the svd() function in MATLAB as shown in Equation 6.3.

approximating common shapes than others.

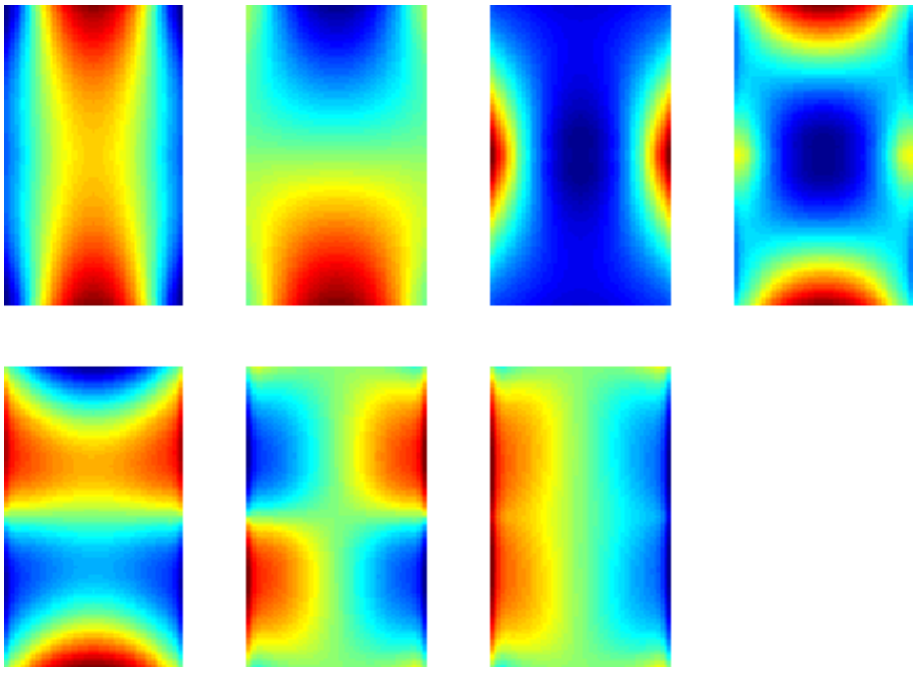

Figure 6.10. Orthogonal modes found through SVD analysis in MATLAB for the protoype arrangement shown in Figure 6.6.

6.4 Actuator Arrangements

Finite element analysis and singular value decomposition were used to check the viability of different actuators topologies through their ability to correct common large scale errors. The ability to correct for first order astigmatism and twist was tested since these are common modes encountered in slumped glass due to springback after slumping (Ghigo et al. (2013)). To this end, SVD was used as outlined in Section to find a control matrix for each of the various actuator arrangements under consideration, such that they could be made to approximate common corrections necessary in slumped glass mirrors. This produced a least-squares fit to the input surface based on the limitations of the actuators.

The following Figures 6.11 - 6.14 show different actuation and mounting strategies, and it is clear that some are more able than others to produce the basic shapes used as a test in this case. The different designs are referred to as MkI, MkII, MkIII and MkIV. This refers to the order in which the different paradigms (and slight variations thereof) were considered. In each of the following figures the left hand column shows the three test shapes and the right column shows the best approximation of this shape according to SVD. It is important to remember that these simulations rely on several assumptions such as actuator linearity (SVD) and the accuracy of the pseudo-MFC custom material created in COMSOL (Section 6.1) in order to simulate the actuator behaviour.

6.4.1 MkI

The first arrangement tested, shown in Figure 6.11, has six independent actuators equally spaced around the mirror. The supported edge is un-actuated as it is impossible to adjust, and in theory the support constrains the mirror to the correct shape in that area. This prototype is mounted as shown in Figure 6.5a.

It can be seen that, although the mirror is able to reproduce a twist and astigmatism conjugate to the optical axis, it struggles to introduce curvature along the optical axis without also tilting the mirror in tip. This effect is exploited in the second arrangement (Figure 6.12) to allow a tip adjustment.

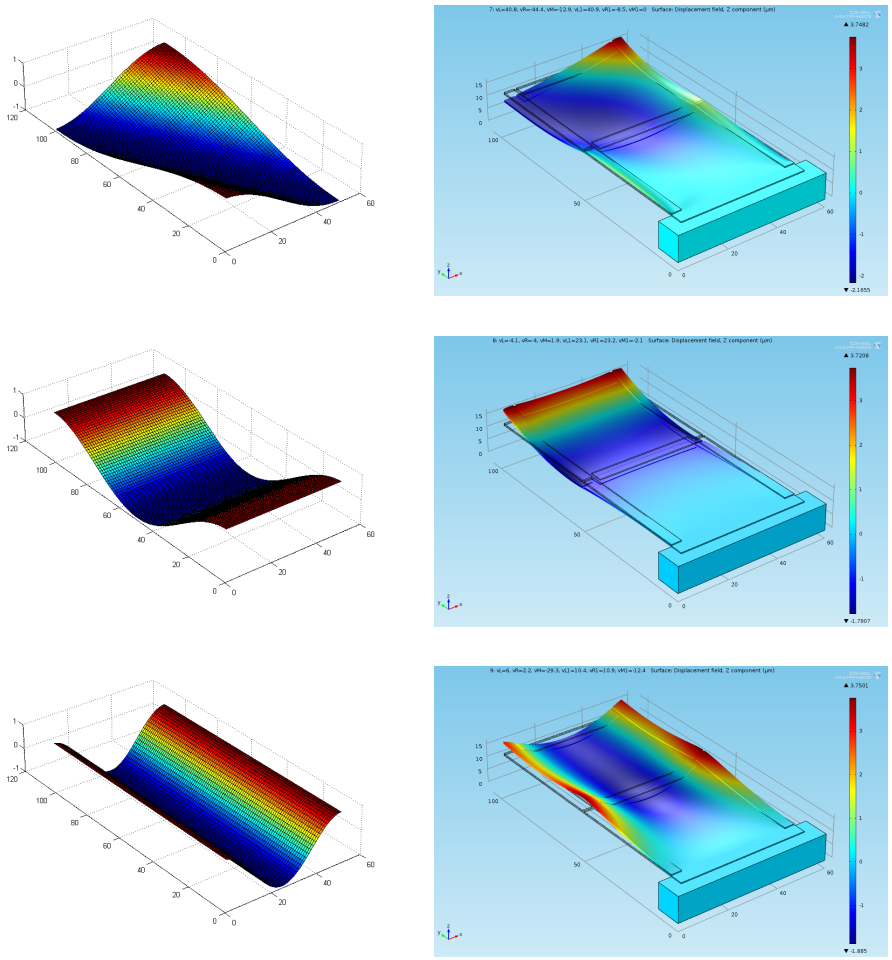

(a) Deformation (b) Least squares

Figure 6.11. A mirror supported along a single edge with six actuators is able to produce forms accurately in one direction, but introduces unnecessary tip changes when correcting aberrations along the optical axis.

6.4.2 MkII

This configuration with five independent actuators has the advantage of being able to adjust the overall tip of the mirror very accurately using the two smaller actuators near the mirror support. As shown in Chapter 5, the optical performance of a grazing incidence mirror is very sensitive to tip. Aside from this advantage, the performance of this arrangement is quite poor.

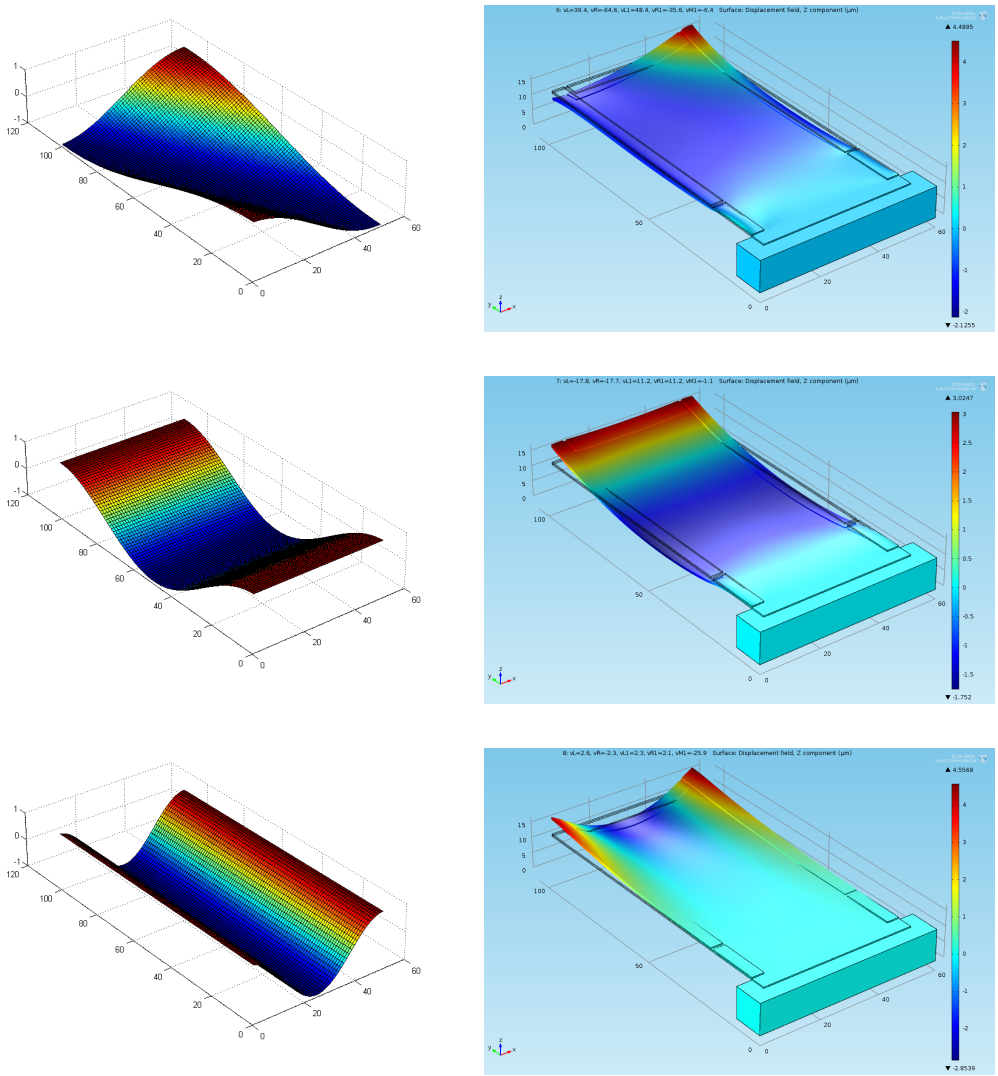

(a) Deformation (b) Least squares

Figure 6.12. The unwanted tip changes exhibited in Figure 6.11 are exploited here to allow for a gross tip adjustment of the mirror, but the ability of the mirror to produce these low-order shapes suffers.

6.4.3 MkIII

The third arrangment simulated was an improvement on MkI, in that placing the central actuator closer to the mount allows for a more uniform adjustment of the radius of curvature. The rigidity of the mount greatly reduces the effect of actuation nearby, so one pair of actuators was moved closer to the mounted edge in order to 'focus' their influence function in that area. It can be seen that the bottom shape is consequently much better approximated than in Figure 6.11.

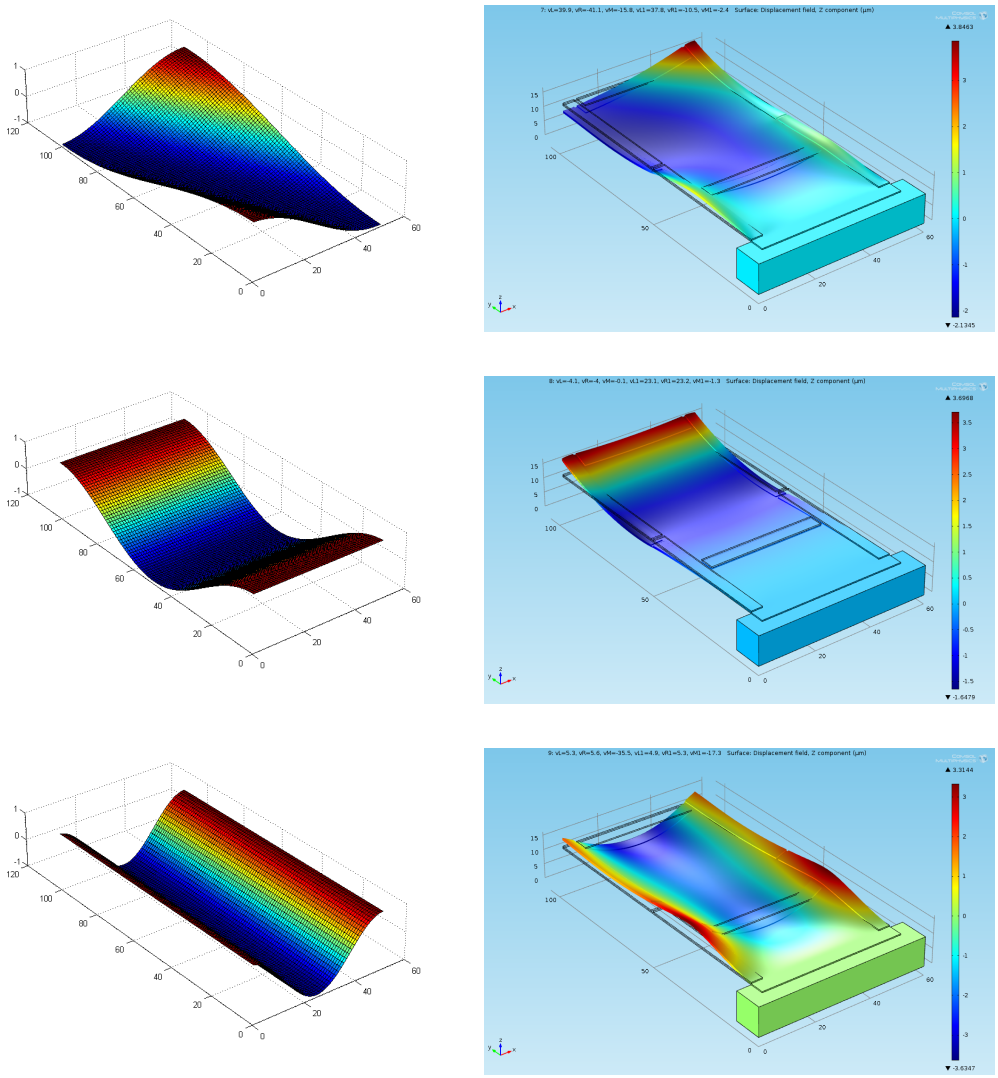

(a) Deformation (b) Least squares

Figure 6.13. This arrangement of actuators is the same as in Figure 6.11, except that the second radial actuator is moved closed to the mount. This allows for greater adjustment of the mirrors radius of curvature.

6.4.4 Corner Supports (MkIV)

A corner-braced design was also simulated. From Figure 6.14 it can be seen that this actually allows closer mapping of the input figure. However, the voltage required to achieve this is higher due to the extra constraints on the mirror. It also becomes impossible to adjust the overall tip and tilt of the mirror, so greater care must be taken during manufacture and integration. This mounting strategy is the same as that shown in 6.5b. The corner mountings are simulated to be made of stiff rubber in order to moderate the effect of the extra constraints.

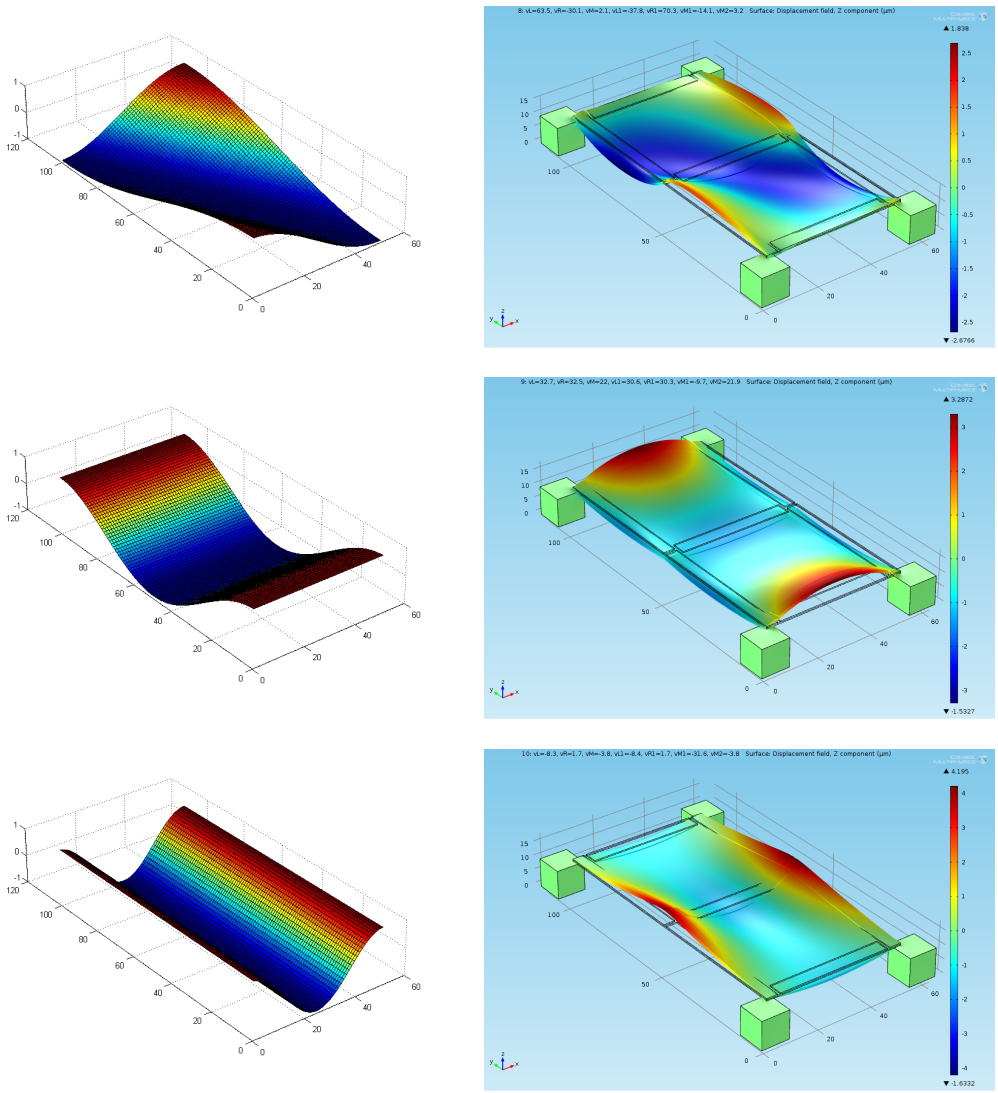

(a) Deformation (b) Least squares

Figure 6.14. The fourth design is supported only lightly at each corner, which allows for better mechanical support of the mirror at the expense of actuator range.

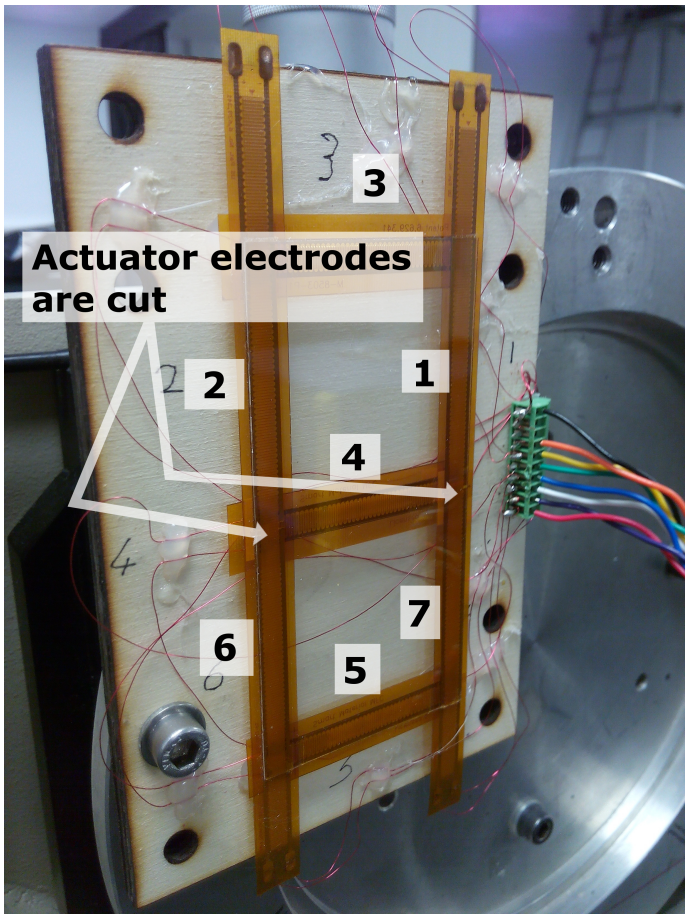

Figure 6.15. A closeup of the prototype with attached actuators numbered. The glass segment measures 50mm×100mm and is 0.4mm thick.

6.5 Construction

On balance, it was decided that corner supports are a better choice due to the extra mechanical stability and fixation of tip and tilt upon mounting. The simulated influence functions of the actuators are also more conducive to correction of common aberrations, and construction and testing of a prototype would be much easier with this configuration. Actuators and supports were placed as shown in Section 6.4.4 (MkIV).

The actuators used to construct the final prototype were purchased from Smart Material GmbH. The glass used was a 50x100mm sheet of D263T eco thin glass from Schott. An image of the prototype is shown in Figure 6.15. Three 3x85mm actuators (product code M 8503 P1) were trimmed down to size and used for actuators 3, 4 and 5 (see Figure 6.15 for numbering). For the long edges, two 3x140mm actuators were used (M 14003 P1) with the electrodes cut in the middle to create four separate areas for actuators 1,2,6 and 7. Note that the actuator measurements refer to the active area, the package dimensions exceed these numbers by several mm in each direction.

5mm double sided polyimide Kapton® tape was used to attach the actuators to the rear surface of the mirror. The total thickness of this tape is 100μm with 30μm of silicone adhesive on each side. The tape is low outgassing and cryogenically compatible.

The mirror was mounted to a wooden board using small blobs of hot glue in the corners. This is an approximation of the semi-rigid corner mounting scheme shown in Section 6.4.4, since the cooled consistency of the glue is that of a fairly stiff rubber.

The glass was used uncoated since it was reflective enough to be used with a deflectometric setup (see Chapter 7) and it was thin enough, and the thickness constant enough, that there were no problems with false readings from the rear surface.

6.6 Ideas for Integration

Having chosen a mounting strategy and an appropriate actuator arrangement, it is interesting to think how these mirror segments might be combined to build a complete x-ray telescope even at this early stage.

Because an x-ray telescope may have many hundreds of mirror segments, it is sensible to create a repeatable process which can be easily mechanised. To this end Brera Astronomical Observatory designed and built an 'integration machine' to populate their mirror cells (Civitani et al. (2011)). Something similar can be created to hold corner-supported segments in place whilst glue is curing. A mount must provide a stable mechanical base for the mirror to support it in launch, without overconstraining it as discussed previously in this chapter. It must also be light-weight, thermally matched to the mirror and other attached structures, and allow as much clear aperture as possible for each segment to make best use of the glass present in the assembly.

A simple cell is shown in Figure 6.16. Populated from the bottom upwards, this cell would allow each mirror segment to be supported from its rear (non-optical) side as it is slid into the cell and glued. This is an important opportunity to add initial gross corrections to the mirror, the position of which could be monitored and corrected in-situ as the glue is curing. In the case of the prototype being developed, a shaped vacuum chuck which exposes the mirror edges could be attached to a hexapod robot, allowing the corners to be bonded to the cell with semi-rigid silicone. This is very similar to the process developed at Brera, and would provide good fixing of tip and tilt during mirror bonding, which is essential with a well-constrained mounting scheme. Although the radius of curvature varies slightly with each mirror in the stack, it is possible that these variations could be provided post-installation through use of the bonded actuators. This might require some

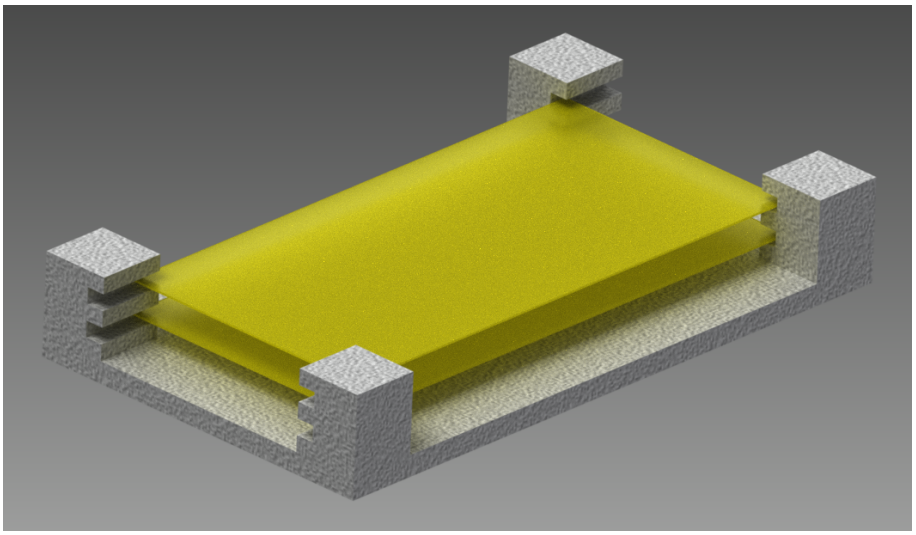

Figure 6.16. Proposed cell design. Glass segments are yellow with the optical face on the underside.

rethinking of the actuator placement, but it could be an interesting way of simplifying mirror manufacture.

As well as mechanical concerns, there are electrical considerations which must be made when designing a mirror cell which may contain several mirrors with many actuators. For instance, a great deal of time and complexity could be saved if the actuators connected very simply to the cell when the mirrors were installed. Automating this wiring as part of the mirror installation would be very beneficial. Similarly, if the mirror cells are constructed such that they connect together and slot onto an electrical bus the wiring can be simplified even further. The piezo driver electronics could be offloaded entirely onto each mirror cell to make them completely modular, but the harsh environment and sensitivity of the mirror after launch may make this unworkable. There are a lot of logistical and system-engineering problems which would need to be tacked before constructing a telescope with so many active mirror elements.

This page was intentionally left blank

Chapter 7

Deflectometry

7.1 Introduction

Before manufacturing a new mirror prototype we needed to develop a way of testing it. This chapter details the developement of a deflectometric surface metrology system designed to measure up to 5×10cm pieces of glass with surface distortions from flat up to several hundred microns.

The proliferation of powerful computers, large displays and relatively high resolution digital cameras in recent years has led to a resurgence in geometric optical tests based upon deflectometry. These systems have been developed under various names but all share similar principles; the system explained here was inspired by a talk on the subject by Run Huang at SPIE Optics & Photonics 2013 (Huang et al. (2013)) and was created to facilitate testing of the prototype described in Chapter 6.

The most common full-field optical tests make use of interferometry, the length-scale of which is determined by the wavelength of light used. Generally this is anywhere from optical to infra-red, placing the upper range of measureable deflections (due to fringe density and phase retrieval problems) at perhaps several tens of microns without nulling optics. Reliably mounting thin glass, which may be only nominally flat, to this level of precision is very difficult and time-consuming and the facilities required were generally not available in the lab used for testing. Ideally a system was needed which was quite insensitive to alignment and vibration, with a dynamic range of several hundred microns and sub-micron resolution. Software controlled phase measuring deflectometry has proved to be a good solution for these requirements.

7.2 Theory

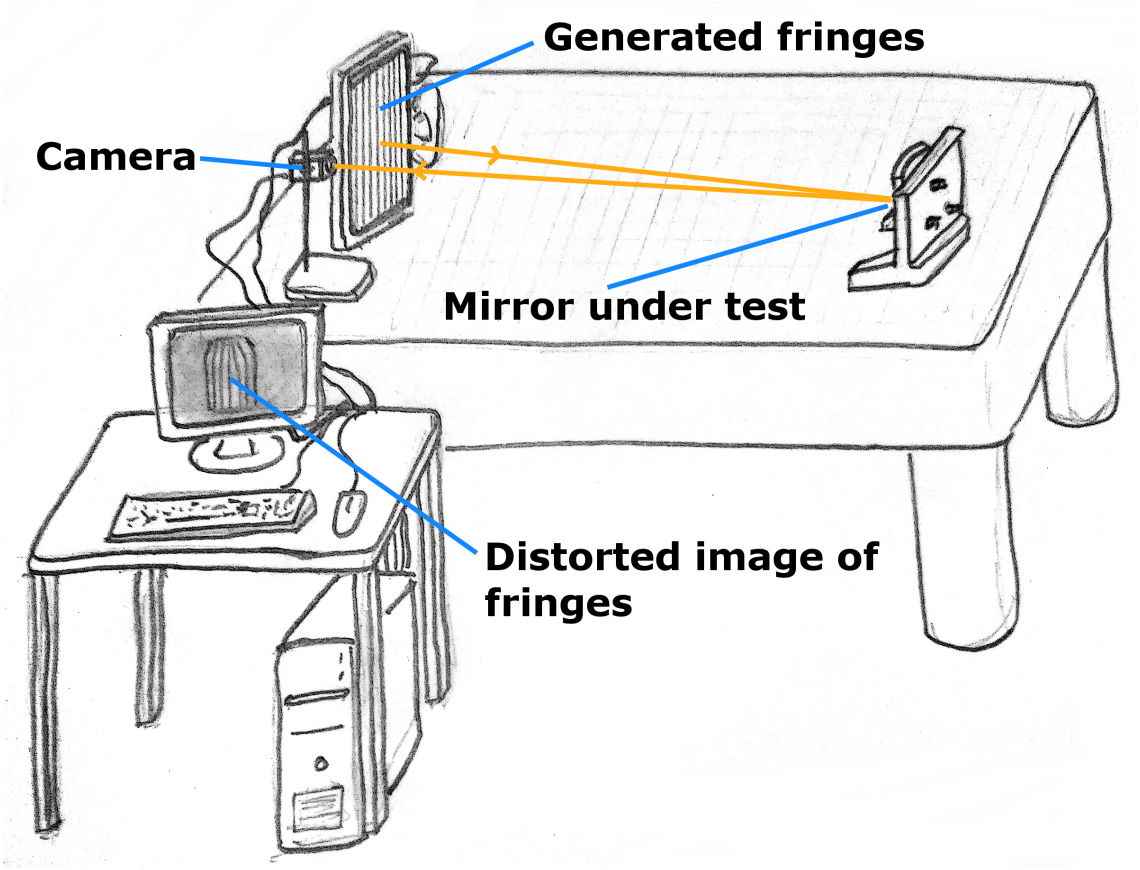

Figure 7.1. A simplified experimental setup. The mirror under test is on the right of the optical table and the camera and generated fringes are on the left. As shown on the computer screen, the camera image of the fringes is distorted due to curvature in the mirror.

In this section will be given an overview of the theory behind phase measuring deflectometry. The basic principle is that regular shapes or fringes are viewed through or 'in' the optic under test. Distortions visible in the final image must then contain information about the test optic, and these distortions can be decoded to reveal the shape of the object under test.

More specifically, some kind of screen or projection is set up a distance (d) away from the test optic as shown in Figure 7.1. This distance forms an optical lever which will ultimately determine the sensitivity of the test; a distance of around two metres is usually appropriate. Sinusoidal fringes are created on the screen according to a phase which increases linearly either horizontally or vertically across the screen. The phase gradient can be controlled via software and allows for the sensitivity of the test to be further adjusted based on the optic under test. Greater fringe spacing is more appropriate for

severely distorted optics but measurements are noisier due to the reduced sensitivity.

A camera is placed as close to the optical axis as possible (see Section 7.2.3 for certain optical and physical considerations) and images are taken at phase shifts of 0, $\pi/2$, π and $3\pi/2$ radians. Each pixel in the camera image represents a portion of the optic under test, which can be given a phase based on the part of the screen which is imaged through or 'in' it. This phase can be accurately reconstructed using the four phase-shifted images (see Section 7.2.1). A change in angle of the surface of the optic causes a different part of the screen to be imaged, hence distorting the image and changing the 'phase' of that part of the optic. Vertical fringes (phase changing vertically) reveal tip, whereas horizontal fringes show tilt. Both are used sequentially in order to provide a complete basis for reconstructing surface height (Catling et al. (2014)).

It is easy to see that the phase change $\delta\theta$ due to a test surface deflection α is $\frac{2\pi d}{p}\sin(2\alpha)$, where d is the separation between the optic and screen and p is the physical fringe period on the screen. Since all deflections should be small this can be further approximated as $4\pi d\alpha/p$, which can be rearranged to find α when the phase change is known. α can be related to an absolute slope by using a known flat mirror to create a reference phase image which is then used to find $\delta\theta$. This also has the advantage of reducing certain systematic effects since they are common to both the reference and measurement phase images and disappear during the subtraction of one from the other.

Once this operation has been performed for every pixel within the area of interest, for both orientations of fringe, a complete gradient field of the surface has been found and the surface height (ignoring some constant piston term) can be reconstructed.

7.2.1 Phase Retrieval

The first and most important part of the process described in the previous section is phase retrieval. For this test, four phase shifted images are used with a four step algorithm to reconstruct the pixel phase from the intensity:

$$\theta + \delta\theta = tan^{-1}\left(\frac{I(\theta + 3\pi/2) - I(\theta + \pi/2)}{I(\theta) - I(\theta + \pi)}\right) \tag{7.1}$$

Where $I(\theta)$ is the measured intensity of a pixel and θ the phase which increases linearly across the screen. In theory the measured intensity of each pixel should simply follow $I(\theta) = A + B\cos(\theta)$, where A is some background term and B is the camera response to illumination which varies as $\cos(\theta)$. However, there are several effects introduced by screen

brightness, surface reflectivity and camera response linearity which are not completely removed by the four-step algorithm, so a prior calibration stage is introduced which allows flatfielding and mapping of measured intensity back to the digital pixel value. This is described in more detail in Section 7.3.

Having found $\theta + \delta\theta$, $\delta\theta$ is then found by subtracting the output of Equation 7.1 for a reference measurement image from the test image. The values of $\delta\theta$ are used to construct a gradient field for the surface, $\hat{G}_{i,j}$ which is a $m \times n$ matrix of 2D vectors, where m and n are the number of rows and columns of camera pixels used to capture the surface under test.

7.2.2 Reconstruction of Surface

The next step is to reconstruct a height map $H(x, y)$ from the gradient field $\hat{G}(x, y)$. Surface reconstruction is a common problem in graphics and image processing in general, not only in surface metrology. There are several methods of retrieving $H(x, y)$ from a gradient field, and the most appropriate method usually depends on some prior knowledge of the surface being reconstructed. Optical surfaces are usually continuous and, if the test is set up appropriately, well sampled, so simple discrete integration is used in this case with $H(x, y)$ being described by $H_{i,j}$. A two-pass approach described by Klette and Schlns (1996) was used, starting from opposite corners.

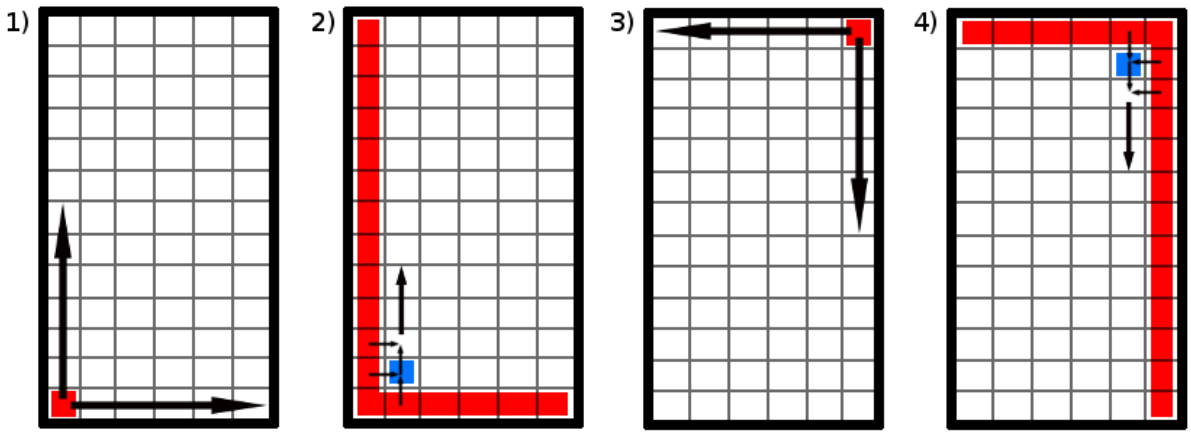

Figure 7.2. This image shows how the surface height is found by integrating the gradient field. Edges are integrated first, starting from a corner which is arbitrarily set to $H_{0,0} = 0$. Surface pixels are then reconstructed using both of the edges which border the previously reconstructed pixels or edges. The process is repeated from the opposite corner and the surfaces are averaged.

Values are first found for the sides after setting the surface height at the corner to 0

($H_{0,0} = 0$):

$$H_{0,0} = 0; \qquad H_{0,j} = H_{0,j-1} + sG^0_{0,j-1} \tag{7.2}$$

$$H_{i,0} = H_{i-1,0} + sG^1_{i-1,0} \tag{7.3}$$

Having found height values for the edge pixels, this process is repeated with the exception that each new pixel now has two neighbours with a known height. Both neighbours contribute to the surface height calculation of the new pixel in order to reduce errors (see Figure 7.2):

$$H_{i,j} = \frac{1}{2}(H_{i-1,j} + H_{i,j-1}) + \frac{1}{4}(G^0_{i,j-1} + G^0_{i,j} + G^1_{i-1,j} + G^1_{i,j})s \tag{7.4}$$

where s is the projected size of each camera pixel on the mirror surface. This process is then repeated using the opposite corner as a starting point; the two surfaces are averaged afterwards in a further attempt to reduce any errors and systematics. This process is shown diagrammatically in Figure 7.2.

7.2.3 Considerations

There are several factors which must be considered before the methods described above can be implemented successfully in reality. Firstly, depth of field requires that the camera aperture be small if both screen and test surface are to be simultaneously in focus. Otherwise it is possible to trade uncertainty in phase (translating to height errors) for uncertainty in spatial position by choosing whether to focus on the mirror or the screen. Secondly, the screen must be large enough to cover the field of view of the camera through the test optic, which is dependant upon the power of the piece under test but is generally at least twice the size of the test optic. Finally, the field of view of the camera is often much larger than it needs to be so some provision must be made for cropping the image, and great care must be taken that the test and reference optics are placed in the correct position.

7.3 Methodology

An inexpensive USB CMOS camera (Thorlabs DCC1545M) with a 50mm lens was placed 2m away from a 15cm x 30cm 1/10th wave flat mirror. A 22” LCD screen was attached to a laptop and placed next to the camera such that it was imaged through the mirror. Figure 7.4 shows the position of the screen and camera as seen from the test or reference

optic.

A code was written in python using the pyUeye library, which is a wrapper for the uEye camera drivers which work with the Thorlabs DCC1545M, to automate the process of taking images. Calibration images can be taken using a command which generates a uniform brightness on the screen at pixel values of `[0,25,50,75,100,125,150,175,200,225,250]`. The user may set the camera gain and the numbers of images to take for each measurement as arguments in this command. The images for each measurement are averaged and stored in a 'calibration' subfolder within the folder assigned to the specific optic. Each optic is assigned its own directory - this section of the code does not make any distinction between reference or test optics.

Another command is used to take a sequence of measurement images. Within this command there also exist arguments to set the camera gain and the number of images over which to average, but the fringe width may also be altered. The software then generates fringes on the LCD and takes measurements at the phaseshifts of 0, $\pi/2$, π, and $3\pi/2$ radians described in Section 7.2.1. This is done with both horizontal and vertical fringes and takes less than 30 seconds per measurement with a reasonable number of stacked images. These images are then stored in the directory assigned to the optic.

The laptop which contains these images is connected to the internet and synced remotely to a desktop PC elsewhere. The rest of the analysis happens in MATLAB on this other computer. Care must be taken before leaving the lab that suitable reference images exist for the test images just taken and that none of the images contains saturated pixels. The simplest approach is to take reference images with various periods (3,5,10,15 and 20mm) after finding a suitable value for the gain. The camera exposure may also be altered if necessary.

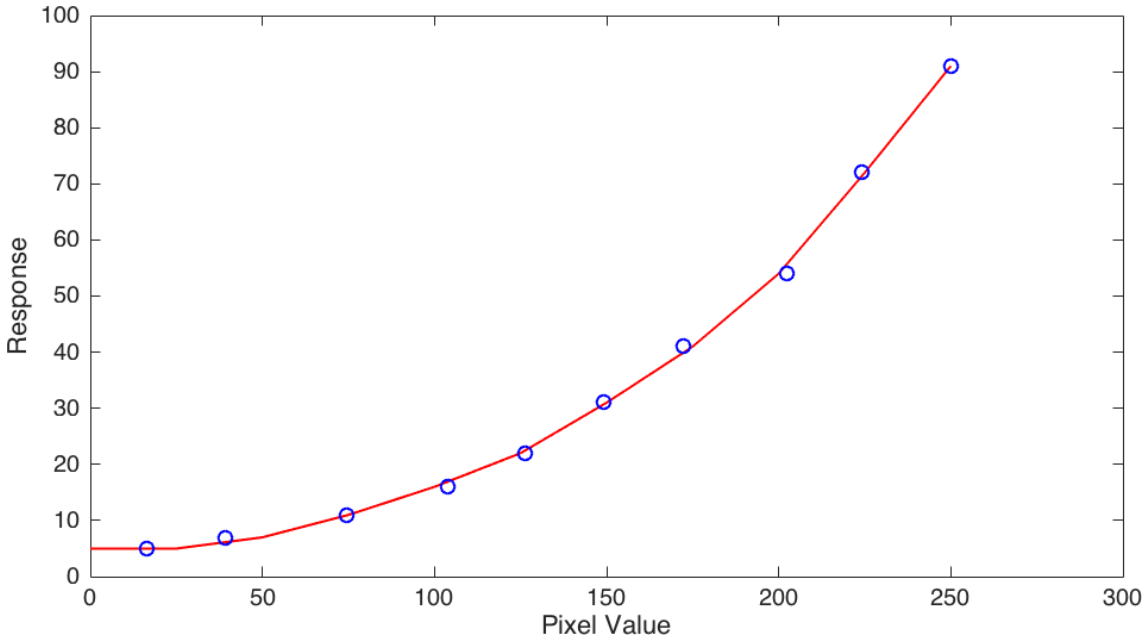

Figure 7.3. This is an example of the fit used to derive screen pixel value, and hence phase, from the camera output. Calibration images are taken every time another optic is under test or if the ambient light conditions change significantly. Camera gain and aperture are selected to provide a good signal in each case. Blue circles are data, the red line is the polynomial fit found by the software.

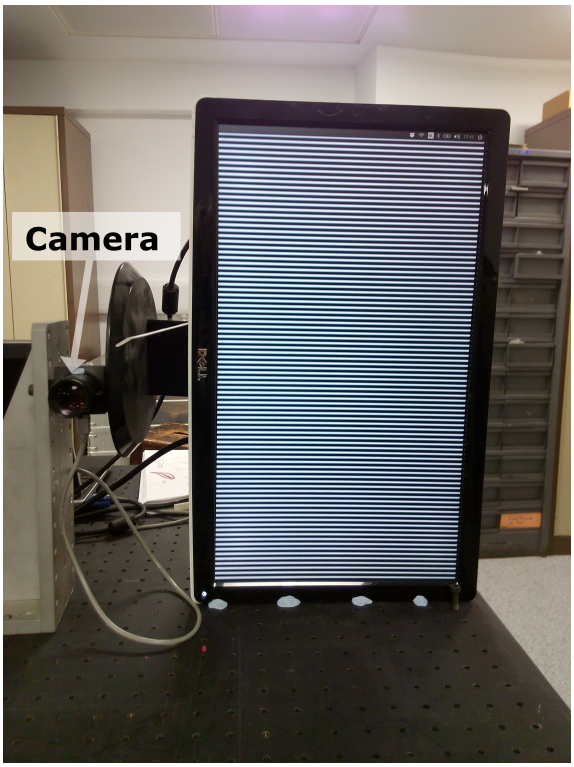

Figure 7.4. Image showing the arrangement of camera (left) and LCD screen. In this image the screen is showing 5mm fringes.

Another code was written to process these images. The user may specify which directory contains test images and which contains reference images, and which fringe spacing to look for. The Python code mentioned above encodes this information in the filenames so there is no confusion. The user must also specify the area of the image which contains data. At this point this area must be rectangular, which would make testing circular optics difficult. The first step is to create a flatfield image for the reference and test optics, which is taken from the brightest calibration image for each. Images are then normalised using this flatfield to account for variations in surface reflectivity. The calibration images are also used to find a fit between screen pixel values and camera pixel values. This is done using the MATLAB *polyfit()* function, then camera pixel values are converted back to screen pixel values using the *polyval()* function to remove the effects of camera and screen response. An example of this fit is shown in Figure 7.3.

The code then uses the four phase shifted images for each orientation to derive the phase at each point of the mirror using Equation 7.1. The values for the two directories are subtracted from each other to find the phase difference. Naturally for the reference flat the phase advances almost linearly across the surface of the mirror, whereas for the test optic it varies across the surface. Sometimes discontinuites of π are found in the returned

phases due to fringes intersecting with the edges of the test area. These discontinuites are found and repaired by the code prior to surface reconstruction.

This process is repeated for both vertical and horizontal fringes to find tip and tilt surface gradients as described in Section 7.2.1. From this gradient field the surface is then reconstructed as described in 7.2.2. The entire process takes less than 20 seconds, with the majority of this time being devoted to surface reconstruction since this part of the algorithmn could not be vectorised.

7.4 Tests

This section shows the results of some preliminary tests done during the development of this technique. Firstly, a comparison was made between an interferometric and deflectometric measurement. This is shown in Figure 7.5. It is apparent that there is a very good, sub-micron agreement between these results even with 10mm fringes, whilst 5mm fringes give yet a closer match. In general it seems that smaller fringes give better data.

In Figure 7.7 are shown the results of using deflectometry to measure the thin pieces of glass shown in Figure 7.6. It is important to note that the measurements in Figures 7.5 and 7.7 were taken with the same physical test set up. Thus, the system is capable of sub-micron accuracy whilst at the same time having a dynamic range of several hundred microns.

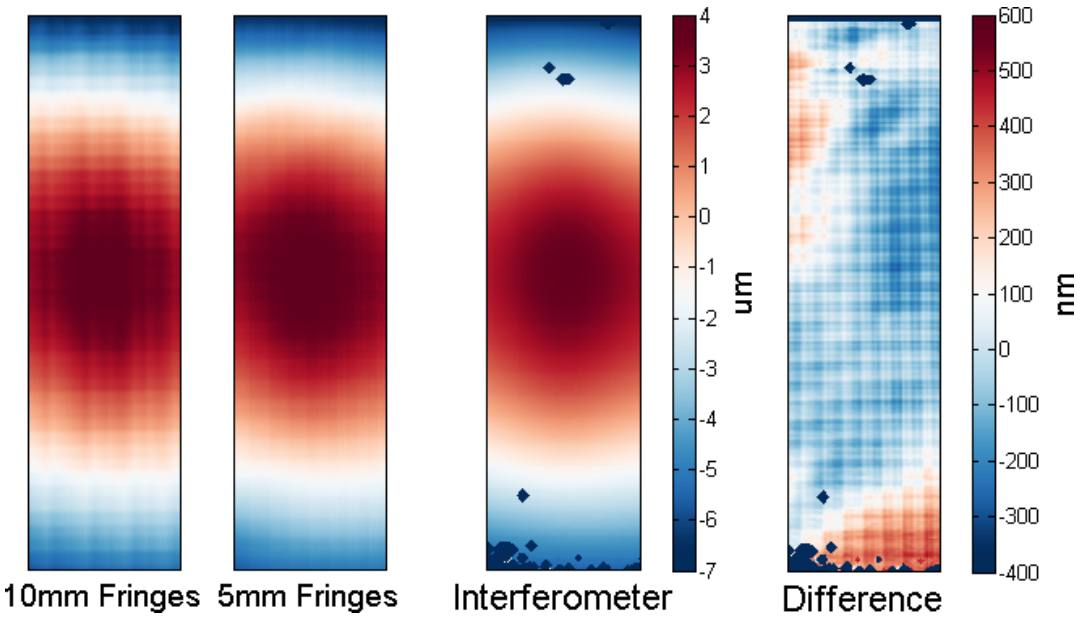

Figure 7.5. A comparison of interferometric and deflectometric (left) tests of a distorted microscope slide. The test piece is silvered and has epoxy glue on the rear, the shrinkage of which has created $\sim 10\mu$m of distortion across the surface. 10mm and 5mm fringes were used. Low-level artefacts from the deflectometric measurement are visible in the residual map on the right appearing as grid-like features with the same period as the fringe spacing.

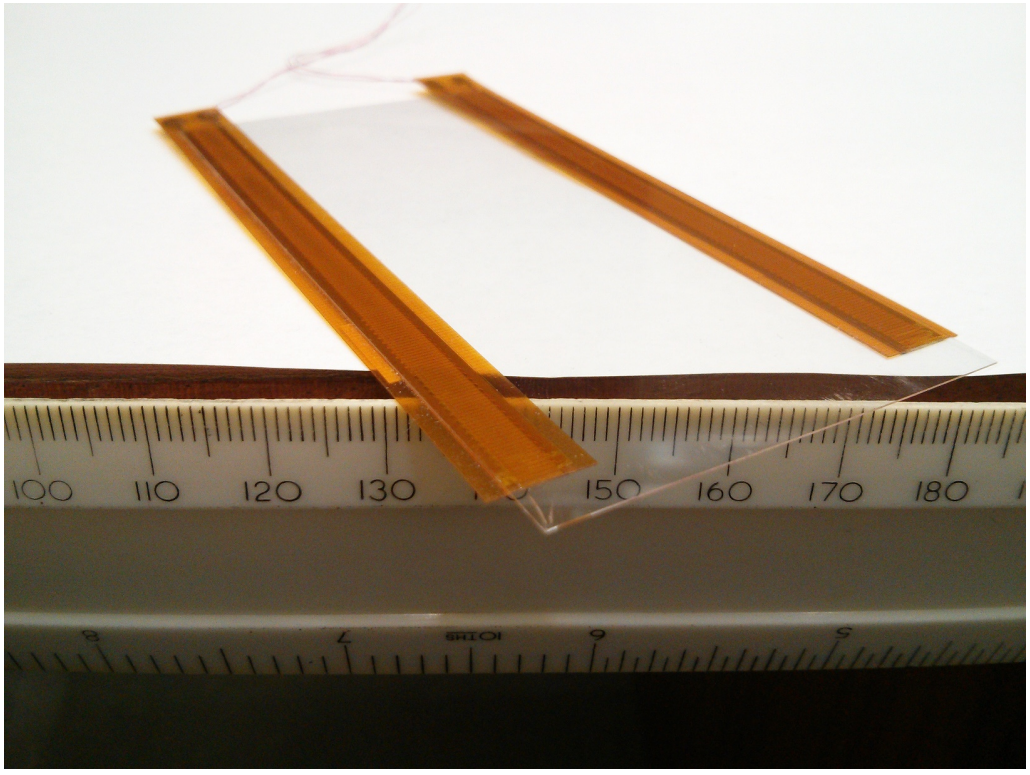

Figure 7.6. An early protoype tested using deflectometry. Results are shown in in Figure 7.7

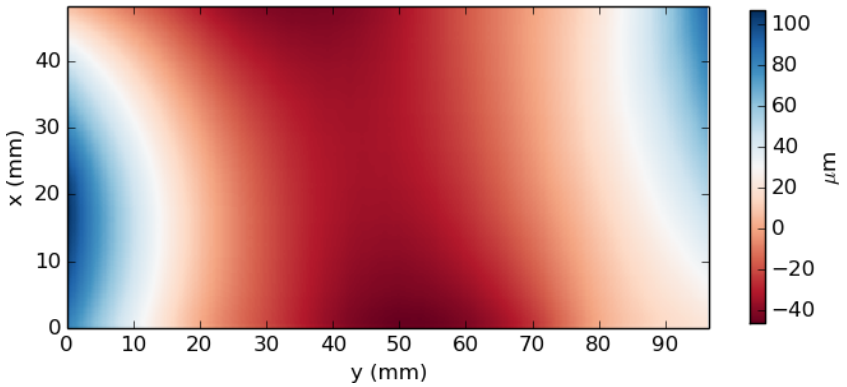

(a) Measured test surface.

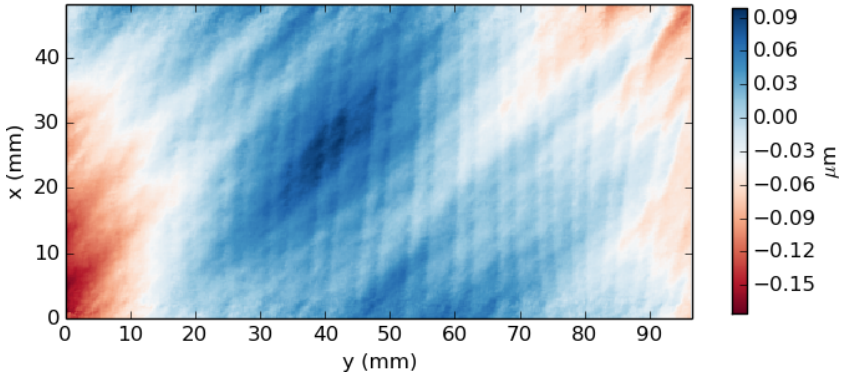

(b) Typical measurement noise.

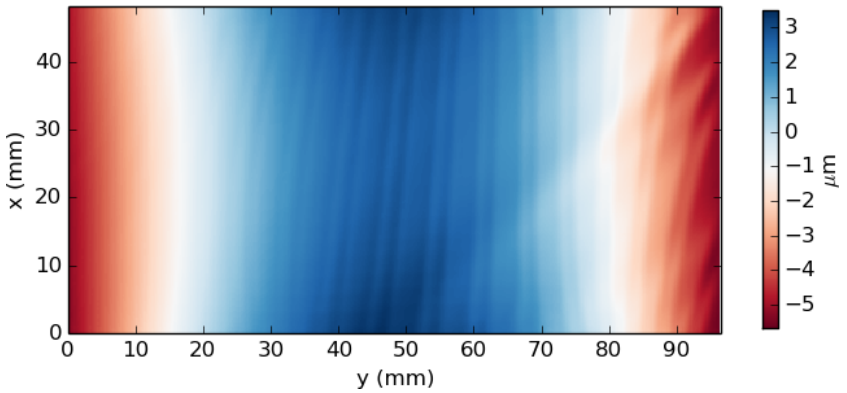

(c) Measured effect of negative -20V.

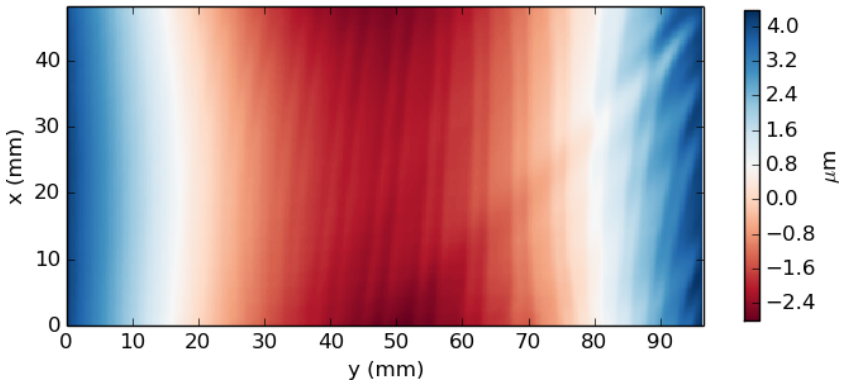

(d) Measured effect of +50V.

Figure 7.7. A series of measurements taken of an early prototype using the methodology described in Section 7.3. 10mm fringes were used with single exposure phase images.

From Figures 7.5 and 7.7 it is clear that there are regular artifacts in the measurement. Since deflectometry has been shown by other authors to be capable of nanometer resolution (Su et al. (2012)), these errors are a result of the implementation used in this case, which was tailored to rapid acquisition rather than precision. In the following Chapter there are many measurements taken with a greater number of averaged images, longer exposures, and more attention paid to avoiding external light, which do not exhibit such artefacts.

Chapter 8

Prototype Testing

8.1 Setup

The deflectometric techniques shown in Chapter 7 were used to test the new prototype described in Chapter 6. The prototype was mounted and connected to a three channel high voltage supply (Figure 8.1). A configurable bus was used to connect each of the seven actuators on the prototype to any of the three channels.

The air temperature in the lab was monitored and found to be constant to within 0.1°C over timescales of several tens of minutes. This is important because of the low thermal mass of the prototype, along with the large surface area exposed to ambient air and the large CTE mismatch between the mount (steel, aluminium, wood), the glass and the actuators (PZT and polyimide).

The prototype was mounted using a single bolt and a terminal block was used for wiring to avoid placing unnecessary stress on the mirror. The screen and camera were placed 2m away from the optical surface, which was then slightly angled such that the camera could image the reflection of the central part of the screen in the test surface. The aperture of the 50mm camera lens was reduced to give an improved depth of field, whilst being still wide enough to detect low intensity pixels on the screen without excessive gain.

The lighting in the laboratory is adjustable and was used at its lowest level for all tests to increase contrast of the test fringes. Finally, reference measurements were taken in the new configuration using the large flat ($\lambda/2$) mirror which is visible at the right-hand edge of Figure 8.1. The prototype was then tested, the results of which are shown in Section 8.2.

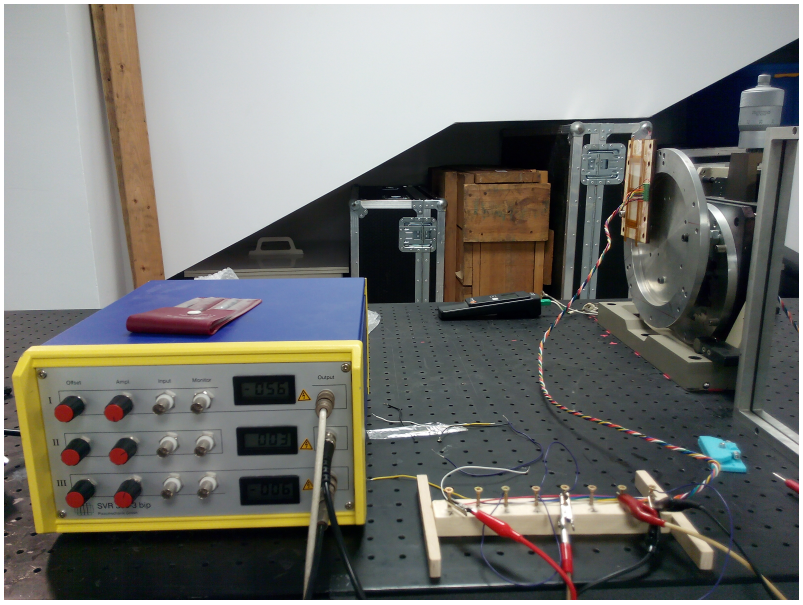

Figure 8.1. A three channel high voltage amplifier was used to control the prototype. A configurable bus was made to pass voltage to selectable combinations of actuators.

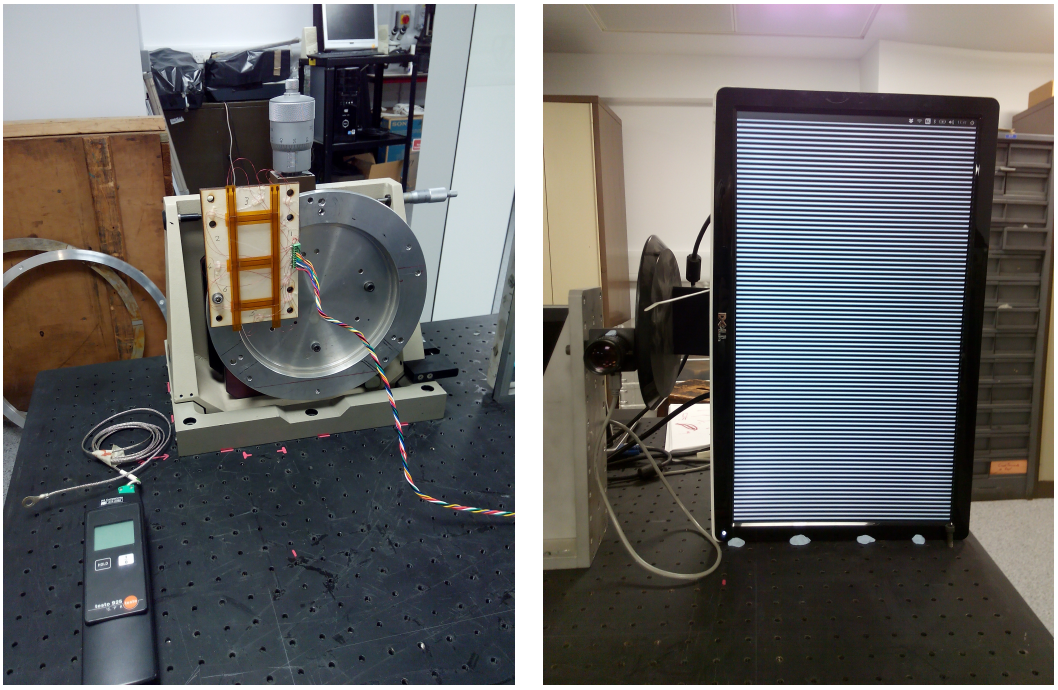

Figure 8.2. The prototype mirror is shown mounted onto its test fixture (left). A digital thermometer was used to check the stability of the ambient air temperature. The screen and camera (right) were placed facing the mirror at a distance of 2m. 5mm fringes were used for all tests.

8.2 Results

Actuators were numbered as shown in Figure 8.3 and tested invididually at 50V to find the influence functions which are shown (also numbered) in Figure 8.4. The prototype was wired such that one electrode of each actuator was held at a common voltage. This facilitates use with high voltage supplies which do not have a negative rail, as an intermediate voltage can be used to set a common level. In this case the voltages supplied to each actuator are measured relative to the common level rather than 'ground', or the 0V output of the amplifier. The high voltage supply used in the tests described here was equipped with a negative rail, meaning that the common connection of the actuators was simply connected to 0V as expected.

It can be seen from Figure 8.4 that the range of motion for the actuators at a given voltage varies dramatically, from 10μm for actuators 1 and 6 on the long edge, to $\sim 0.5\mu$m for actuators 3 and 5 on the short edges. This demonstrates the effect of constraints on actuator range of motion, despite the relatively elastic glue used for bonding the corners. It is also interesting to note the difference in range of motion between actuators 1 and 7 and actuators 2 and 6, which move only half as far despite being in theoretically equivalent placements. This is most probably due to difference in the actuator/glass bond or in the corner mounts due to differences in glue placement, which is quite likely as it was difficult to place the glue accurately when constructing the prototype. This further underlines the importance of constraints in the response of the mirror.

The difference between Figures 8.4c, 8.4e and Figure 8.4d show again the importance of mounting on the response of the mirror. Although all three actuators are along the short axis of the mirror, actuator 4 has a much greater range of motion because it is further away from the constrained corners. The influence function is also 'neater' because it is less affected by variations in glue placement. It should be noted that this sensitivity to mounting is probably due mostly to the tape used to attach the actuators to the rear surface of the mirror. The actuators themselves are very strong and should easily deform the soft glue used to mount the corners of the mirror, but the elastic layer of polyimide tape and adhesive between the actuator and mirror means that some of this motion may be lost and instead the tape layer is deformed. It would be beneficial to test the extent of this effect, either physically or with further FEA using elastic layers between mirror and actuator to simulate the silicone adhesive.

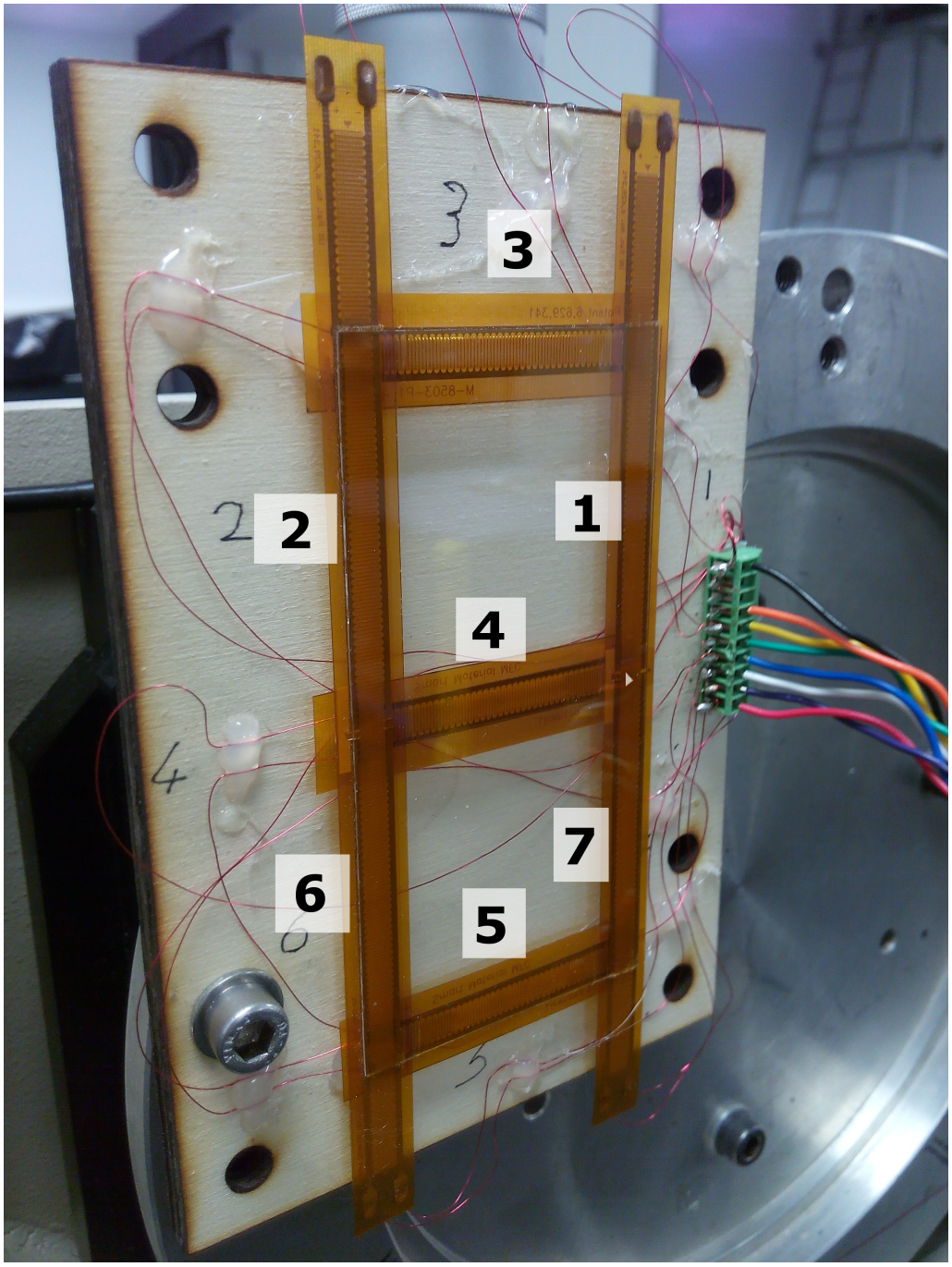

Figure 8.3. A closeup of the prototype with attached actuators numbered.

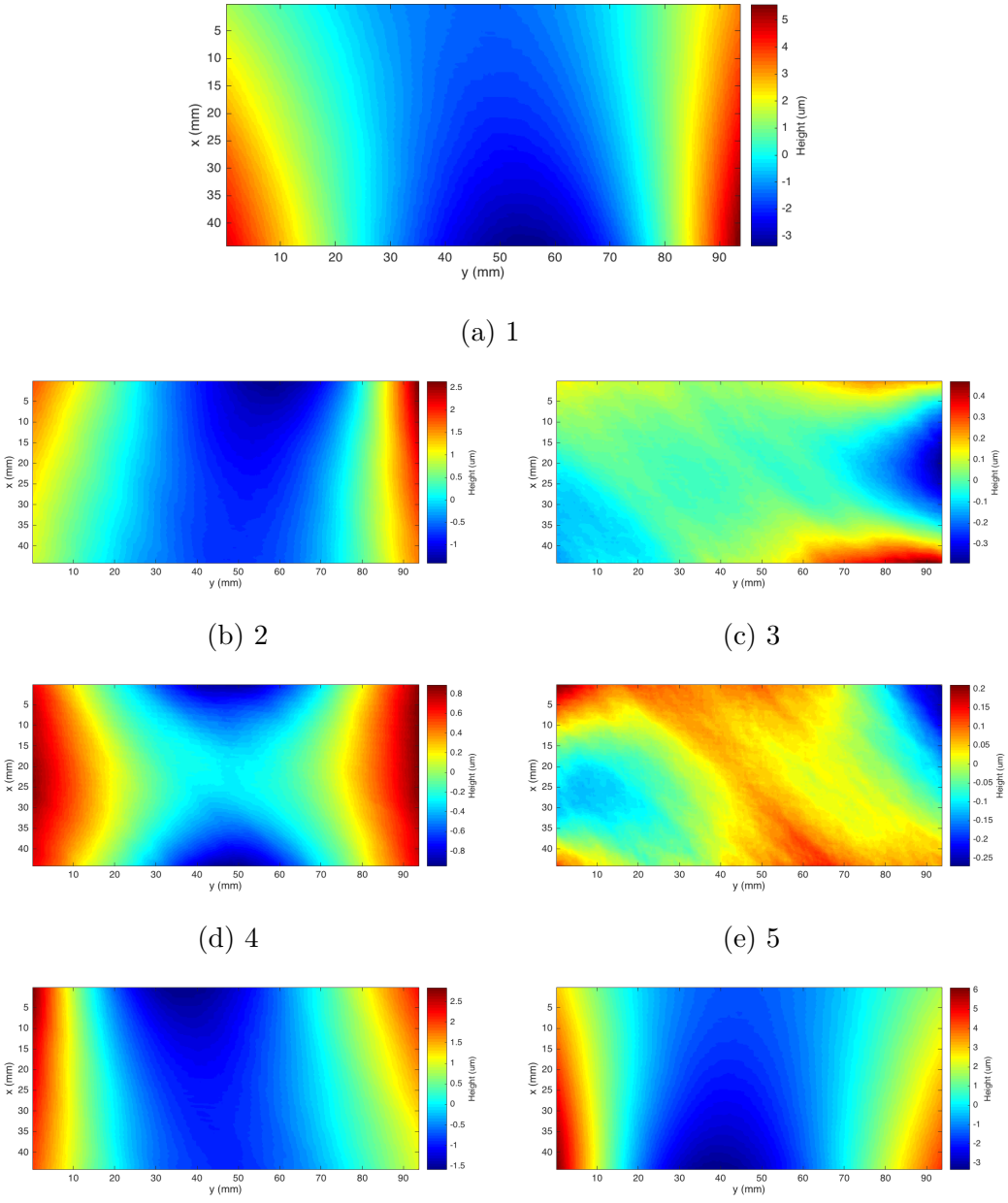

(a) 1

(b) 2

(c) 3

(d) 4

(e) 5

(f) 6

(g) 7

Figure 8.4. Measured influence functions of all actuators. Displacements were found using the deflectometry setup described in Chapter 7. In each measurement the actuator being tested was raised to 50V while the others were held at 0V.

Figure 8.5 shows a trace along the length of the mirror which was generated by taking the average value of a ten pixel wide strip centred on actuator 1. There is no visible kinking or print through despite the cut in the center of the actuator to separate the electrodes for actuators 1 and 7. The change in surface height is displaced from the centre of the mirror in the direction of actuator 1 (the active actuator), but is not centred above the actuator itself. This is due to mounting constraints, and was predicted in the simulations in Chapter 6. A comparison of the influence functions of actuators 1 and 7 is shown in Figure 8.6.

Figure 8.7 shows the effect of actuating 1 and 7 simultaneously in opposite directions, while Figure 8.8 shows a full surface height map of the same test. The range of motion seen in Figure 8.8 is around 5μm at 50V, which is a very good value given requirements for sub-micron accuracy shown in Chapter 5. It is safe to assume that any active x-ray telescope will be required to correct aberrations at the micron and sub-micon level, and being able to do this with relatively low voltages is an advantage.

Figure 8.9 shows a combination of influence functions from actuators 1 and 7 which should reproduce the surface height data shown in Figure 8.8 if the assumption of linear summation of influence functions is correct. This is an important point as SVD (as explained in Chapter 8) relies on this assumption, and any mirror which did not display this characteristic would be very difficult to control. It can be seen from Figures 8.8 and 8.9 that the agreement is qualitively very good. There are some slight differences, but these are around the 10% level and can be explained by measurement error and hysteresis.

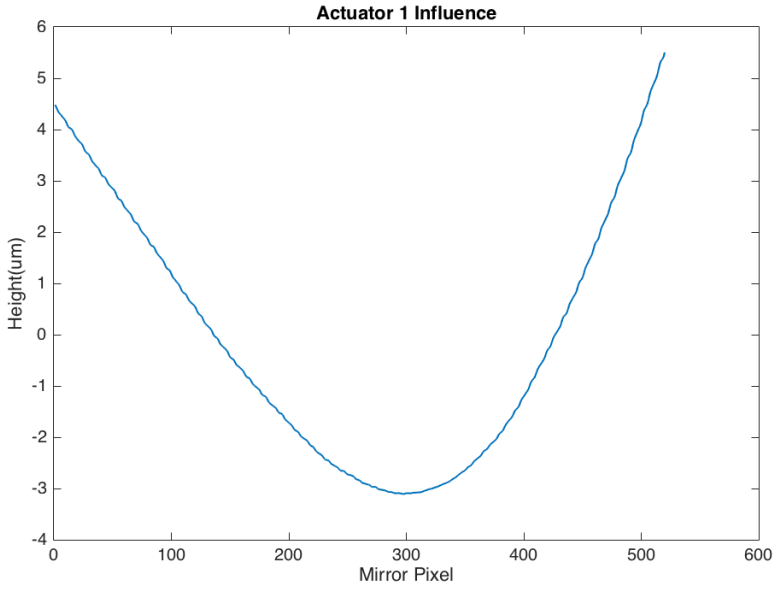

Figure 8.5. Influence function of actuator 1 at 50v. Data was taken from an average of a 10 pixel wide strip roughly centred on actuators 1 and 7, running vertically up the entire side of the mirror (pixel 0 being at the bottom). The displacement is concentrated towards the middle of the mirror due to the edge constraints, despite the position of the actuator being from pixels ∼250-500.

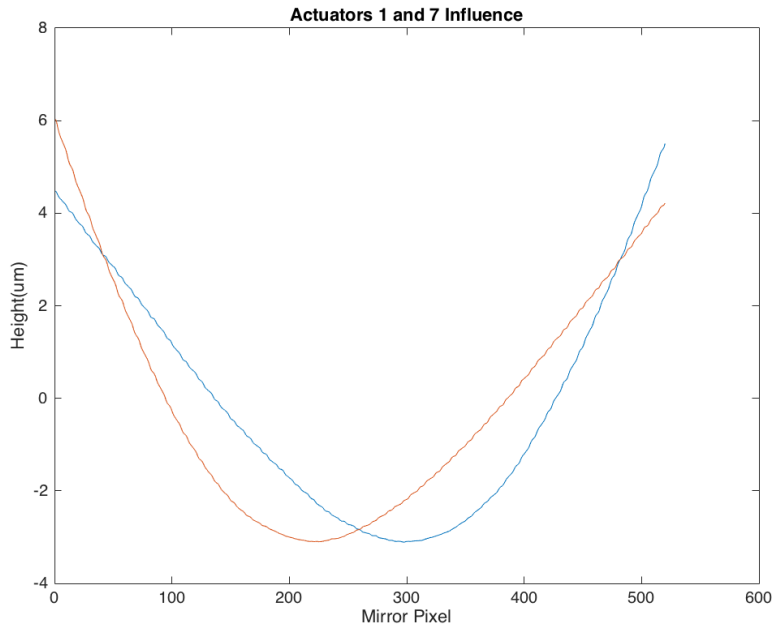

Figure 8.6. A comparison between the influence functions actuators 1 (blue) and 7 (red), with the same setup as in Figure 8.5

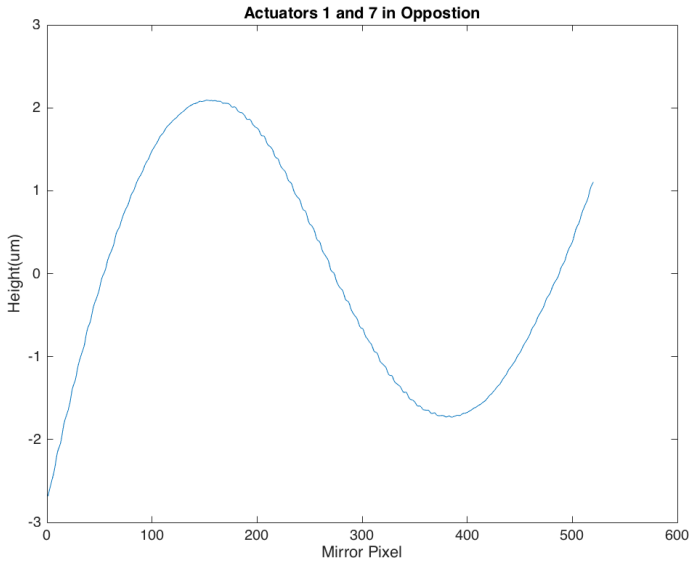

Figure 8.7. The effect of raising actuator 1 to 50V and lowering actuator 7 to -50V. Data were taken from an average of a 10 pixel wide strip roughly centred on actuators 1 and 7, running vertically up the entire side of the mirror (pixel 0 being at the bottom).

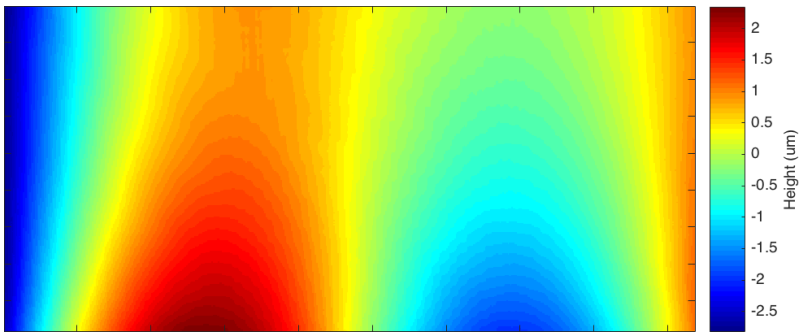

Figure 8.8. A surface height map corresponding to Figure 8.7 showing data for the entire mirror.

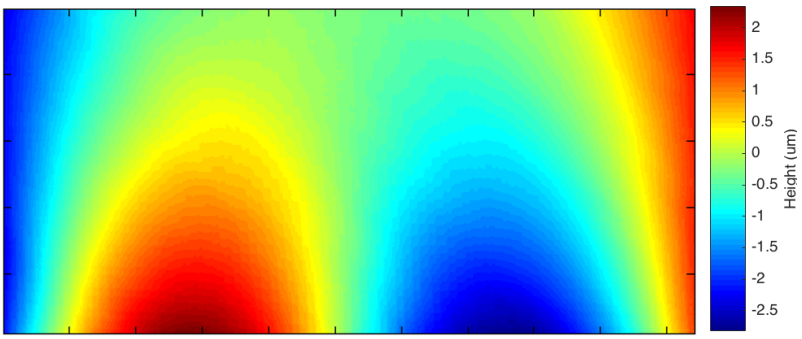

Figure 8.9. A combination of the influence functions from Figures 8.4a and 8.4g (actuators 1 and 7) which should produce the same surface height map as Figure 8.8 if the assumption of influence functions adding linearly is correct.

It is necessary to understand the hysteresis present in a system before it can be reliably controlled. To this end, a point was chosen in the centre of the trace shown in Figure 8.5 and was measured at a range of voltages approached from above and below. It can be seen from this test (Figure 8.10) that there is indeed a large amount of hysteresis present in this prototype, at the level of about 20%, although this is not necessarily a problem as long as it is predictable. There are various ways of reducing the effects of hysteresis; it is especially easy if the useable bandwidth of the system is much higher than that required to correct aberrations. In this case, the actuators are easily capable of moving the mirror at tens of Hz but corrections are only required on the timescale of several seconds or less. A simple strategy in this situation is to oscillate the mirror around the target voltage, reducing the amplitude of the oscillations until a steady voltage is reached. This is the same strategy that was used during the testing of NEMO2 described in Chapter 4. It is interesting to note that the datasheet of the actuators (See Figure 6.2 in Chapter 6) actually lists the hysteresis of the MFC actuators used in the new prototype as 20%, so it seems that the double sided tape used to attach them has not really increased this.

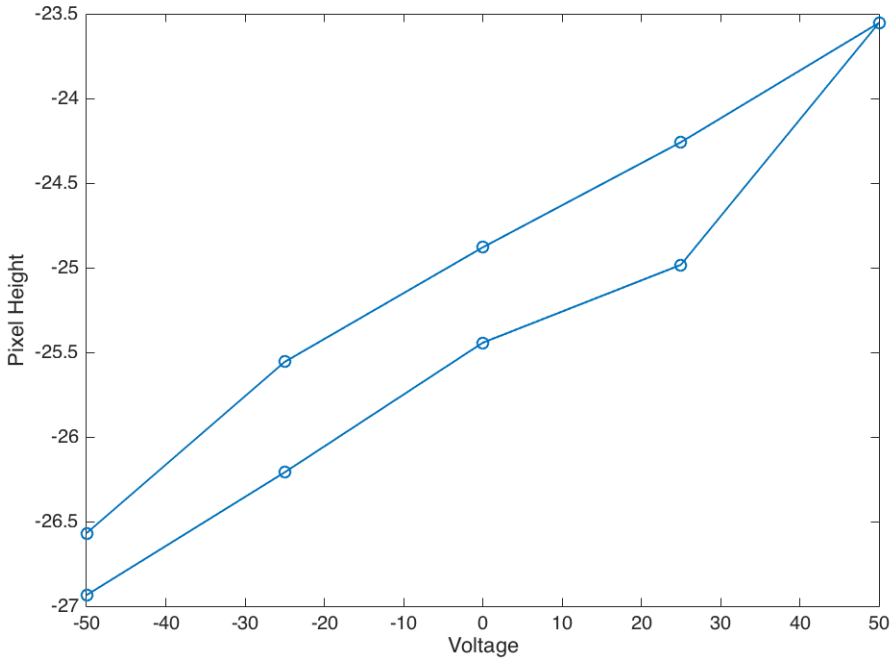

Figure 8.10. An example of hysteresis shown by measuring the displacement of a point on the mirror surface above an actuator at difference voltages.

SVD analysis (as described in Chapter 6) was performed on the measured influence functions, and the command matrices for three simple deformations were found. The desired shapes, along with the best fit approximated given by SVD and the command matrices, are shown in Figures 8.11 - 8.13.

It is clear that the mirror is better able to approximate some deformations than others. Actuator placement was designed such that gross curvature along the radial or axial axes of the mirror should be well formed, but degrees of freedom and compromises made during mounting the prototype mean that more complex shapes are difficult.

It is interesting to compare Figures 8.11 - 8.13 to Figure 6.14 in Chapter 6. The earlier figure was derived from SVD on influence functions found using FEA for a simulated, corner mounted 7 actuator mirror with the same layout. As expected they are quite similar; Figure 8.13 in particular matches well. It appears that Figures 8.11 and 8.12 actually match the desired shapes better than predicted through FEA. Since all of these figures are generated using SVD, it can only be that the actual influence functions as measured in this Chapter are more conducive to forming these shapes than those predicted. This is perhaps due to differences in the rigidity of the corner mounts and inaccurate predictions on how the MFCs will behave when actuated. No attempt was made to model the tape layer in FEA before construction, although it is not clear how that would contribute to this result.

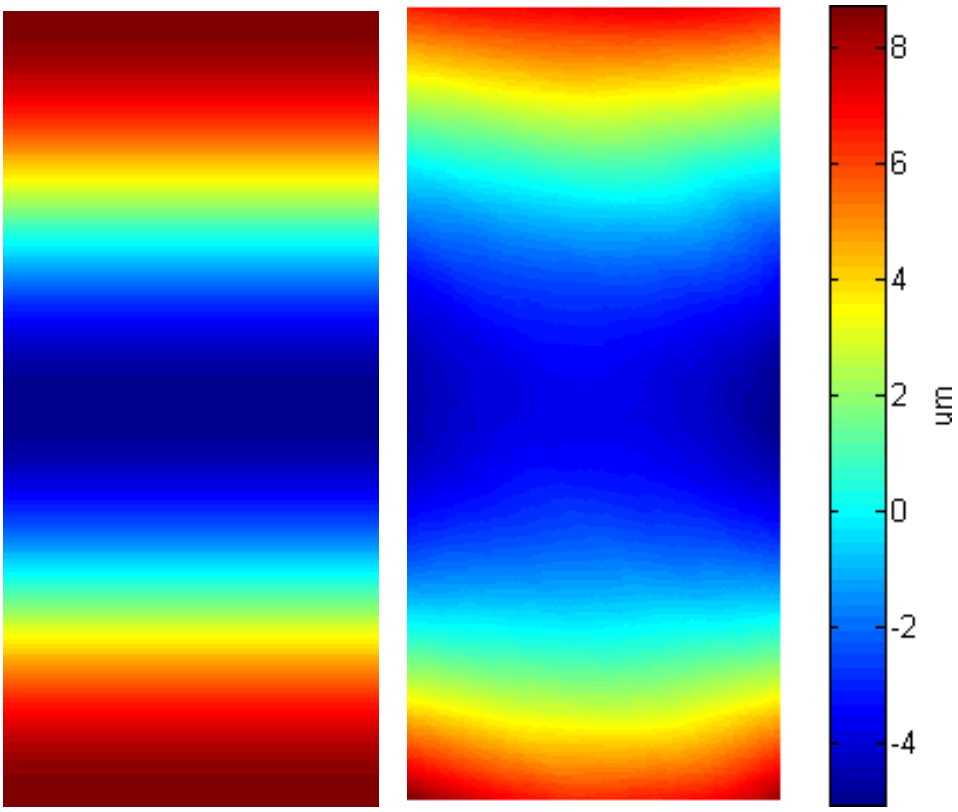

Figure 8.11. Curvature along the long axis of the prototype (left) and the best least-squares approximation (right) attainable according to SVD and the influence functions shown in Figure 8.4

Actuator	1	2	3	4	5	6	7
Voltage	1.7	5.1	15.6	7.9	-13.6	3.6	2.0

Table 8.1. Actuator voltages derived using SVD to fit the shape shown in the left of the above figure

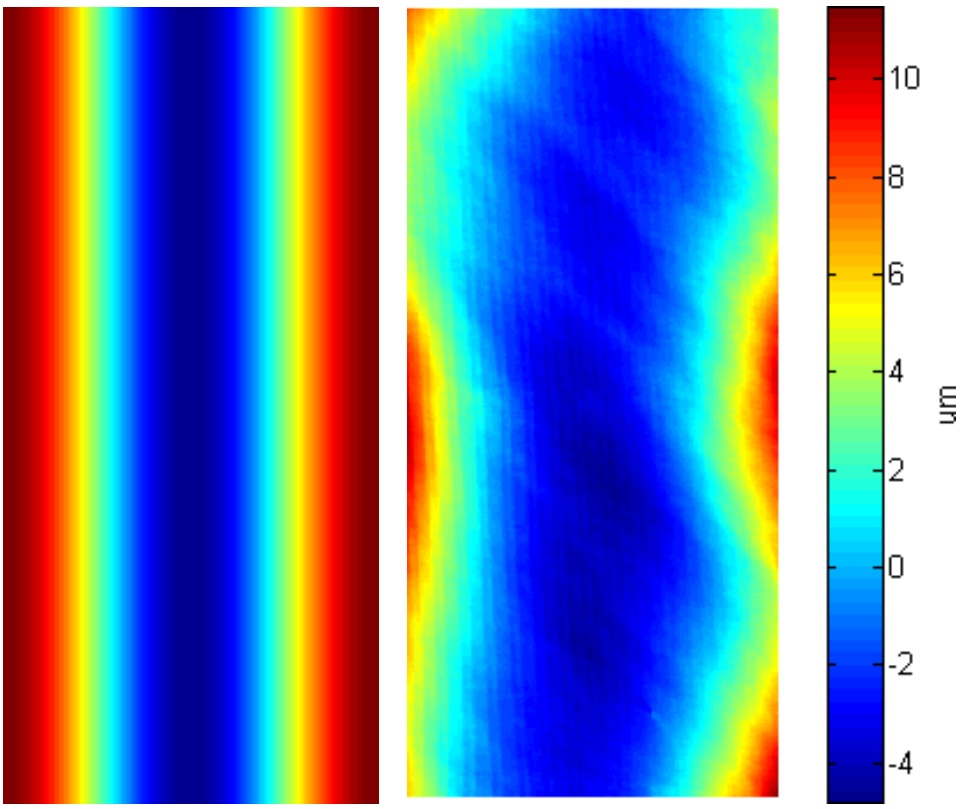

Figure 8.12. Curvature along the short axis of the prototype (left) and the best least-squares approximation (right) attainable according to SVD and the influence functions shown in Figure 8.4

Actuator	1	2	3	4	5	6	7
Voltage	13.2	12.6	63.9	-106.0	45.3	23.2	-4.3

Table 8.2. Actuator voltages derived using SVD to fit the shape shown in the left of the above figure

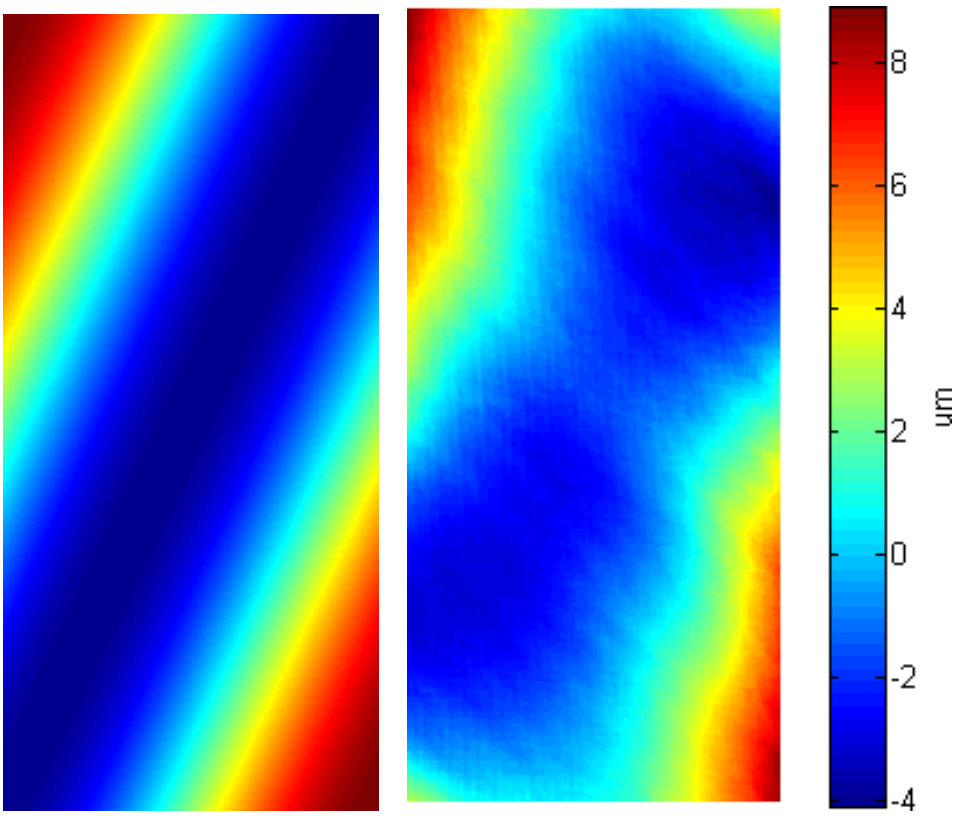

Figure 8.13. Twist in the mirror (left) and the best least-squares approximation (right) attainable according to SVD and the influence functions shown in Figure 8.4

Actuator	1	2	3	4	5	6	7
Voltage	-4.8	27.3	28.9	-25.2	76.5	-8.3	7.7

Table 8.3. Actuator voltages derived using SVD to fit the shape shown in the left of the above figure

8.3 Analysis

Unfortunately, it was not possible within the timeframe of the PhD to test these results by actually applying the voltages to the mirror. However, the results earlier in this chapter still provide good information on the new prototype. The performance of the MFC actuators is surprisingly good and does not appear to be negatively impacted by the use of double sided tape. The hysteresis measured earlier in this chapter was approximately 20%, which coincides with the datasheet value shown in Figure 6.2.

Across a voltage range of ±50V the actuators give a range of motion of about 5 microns, which is sensible given the data on typical aberrations of slumped glass and required surface accuracy for grazing incidence x-ray telescopes (see Chapters 3 and 5). Further testing should be done on the effect of the tape used to mount the actuators and the frequencies with which the mirror can be driven. It would also be interesting to check the long term stability of the tape adhesive, and if the influence functions of the actuators change over time as the adhesive is 'broken in', particularly at higher voltages. It is also necessary to test the cryogenic and vacuum performance of all the elements used in this system, as well as the effect of the differences in CTE between the actuators, their internal components, and the glass substrate. Finally, it would of course be useful to test if measurements of the mirrors shape do correspond to the FEA predictions when SVD-generated voltages are applied.

Chapter 9

Conclusions

Frodo: *It's gone! It's done!*

Sam: *Yes, Mr. Frodo... It's over now*

9.1 Summary

The aim of the work presented here was to explore the effects of using a simple, low-cost modal approach to actuation of thin glass, most notably using off-the-shelf MFC actuators as opposed to custom shaped or deposited PZT. The nature of this work and the environment in which it was conducted necessitated using and developing new techniques for high-power aspheric metrology (Chapter 7) and code for optical simulation of arbitrary surfaces (Chapter 5).

We succeeded in creating a prototype active mirror using the aforementioned MFC actuators. The mirror has a range of motion of around 5 microns within a voltage of $\pm$50V, and should be capable of reproducing modal deflections on scales of several centimetres and above. Actuator placement can be easily adapted to suit common aberrations found in slumped glass and prototypes are relatively easy and inexpensive to manufacture. The method of using double-sided Kapton tape to attach the actuator to the rear surface of the glass seems successful at this stage, with no apparent negative effects regarding hysteresis or range of motion. The performance in vacuum (in terms of outgassing) and at cryogenic temperatures needs to be verified along with the long term stability of the system, but the tape used is suitable for these conditions and the adhesive appears to be more than sufficient so far.

A semi-automated deflectometry system was created in order to test these mirrors (Catling et al. (2014)). The system is able to take a full stack of images of a surface in under 30 seconds, which then take up to another 20 seconds to process on a desktop computer. The resulting measurement has a demonstrated accuracy in the hundreds of nanometer range; it has not been tested beyond this since all the test pieces used were very thin and maintaining their shape at this level between measurements is impractical. However as mentioned in Chapter 7, others have demonstrated the technique to be more than capable of nanometer level resolution (Su et al. (2012)).

A simple raytracing code was written to simulate the performance of grazing incidence optics. In its current form the code is able to generate a parabolic surface with a given size and focal length and add rectangularly derived zernike aberrations to the surface up to the sixth order. The code creates a three dimensional diagram of the surface and allows extraction of the rays at any point along the optical axis.

9.2 Further Work

Extending the deflectometry and raytracing codes would be very interesting. In particular, it would be useful to achieve real-time deflectometric measurements of the mirror to allow rapid characterisation of influence functions and easy testing of the SVD method of control. All of the pieces of work done in this thesis are complementary, although there was not quite enough time to develop them enough to be used to their full potential.

Clearly further testing of the prototype would be beneficial, and it is unfortunate that this was also not possible within the available timeframe. This is very early-stage research so it is not yet clear how the technology could be implemented in an active x-ray telescope, but there is an argument to be made that commercially available actuators will most probably play some part. More work should be done on the mechanical interfacing between the actuator and glass, as polyimide/silicone tape, although it seemed to work in this instance, may not be the best choice.

It is worth noting that the same companies who sell MFC actuators also produce raw PZT fibres, and it would be interesting to deposit electrodes directly on the rear surface of the glass and use these without the polyimide package. It is even possible that the fibres would work well enough in the reduced electrical field created by having electrodes on only a single side and would not need to be sandwiched to the glass with a second electrode layer. However this again raises the question of using glue over large areas on the rear surface of the glass, and shrinkage would likely become an issue. The fibres would also

need to be poled at high temperature and voltages which would introduce more issues if done in-situ.

In the opinion of the author, one of the most important questions in this area which remains unanswered is the calibration strategy for a full-sized telescope with thousands of degrees of freedom. Many groups are constructing zonal active mirrors with actuator sizes of 1cm or less, and little thought is given to how these would be managed in a finished system, or indeed if so many degress of freedom are necessary on every mirror. Some work on wavefront sensing using several intra-focal measurements (Spiga et al. (2016)) could be applicable to a finished in-orbit system, but more research is definitely needed in this direction. As has been mentioned, it seems possible that a combination of active components and passive post-processing such as ion figuring will be necessary to obtain sub-arcsecond resolution, barring unexpected advances in manufacturing. In the near future x-ray astronomy should be well served by silicon pore optics and ATHENA, but it is wise to bear in mind the limitations of this technology (McClelland et al. (2013)) and the possibilities that may come from of exploring other options. Chandra is now living on borrowed time, and there is likely to be a dearth of high resolution x-ray imaging capability for a number of years once it expires. Exploring simple and low-cost approaches to producing high resolution mirrors in the meantime is prudent.

This page was intentionally left blank

Bibliography for Chapter 1

Bernd Aschenbach. "Realization of x-ray telescopes–from design to performance,". *Experimental Astronomy*, 26(1):95–109, 2009. ISSN 1572-9508.

X. Barcons, D. Barret, A. Decourchelle, J.-W. den Herder, T. Dotani, A. C. Fabian, R. Fraga-Encinas, H. Kunieda, D. Lumb, G. Matt, K. Nandra, L. Piro, N. Rando, S. Sciortino, R. K. Smith, L. Strüder, M. G. Watson, N. E. White, and R. Willingale. "Athena (Advanced Telescope for High ENergy Astrophysics) Assessment Study Report for ESA Cosmic Vision 2015-2025,". *ArXiv e-prints*, July 2012.

M. Bavdaz, Ph. Gondoin, K. Wallace, T. Oosterbroek, D. Lumb, D. Martin, P. Verhoeve, L. Puig, L. Torres Soto, and A. N. Parmar. "Ixo system studies and technology preparation," *Proc. SPIE* **7437**. 743702–743702–9, 2009a.

M. Bavdaz, Ph. Gondoin, K. Wallace, T. Oosterbroek, D. Lumb, D. Martin, P. Verhoeve, L. Puig, L. Torres Soto, and A. N. Parmar. "Ixo system studies and technology preparation," *Proc. SPIE* **7437**. 743702–743702–9, 2009b.

Marcos Bavdaz, David H. Lumb, Anthony J. Peacock, Marco Beijersbergen, and Stefan Kraft. "Status of x-ray optics development for the xeus mission," *Proc. SPIE* **5488**. 829–836, 2004.

Marcos Bavdaz, Nicola Rando, Eric Wille, Kotska Wallace, Brian Shortt, Maximilien Collon, Coen van Baren, Giovanni Pareschi, Finn Christensen, Michael Krumrey, and Michael Freyberg. "Esa-led athena/ixo optics development status," *Proc. SPIE* **8147**. 81470C–81470C–8, 2011.

Marco Beijersbergen, Stefan Kraft, Marcos Bavdaz, David H. Lumb, Ramses Guenther, Maximilien Collon, Arjan L. Mieremet, Ray Fairbend, and Anthony Peacock. "Development of x-ray pore optics: novel high-resolution silicon millipore optics for xeus and

ultralow mass glass micropore optics for imaging and timing," *Proc. SPIE* **5539**. 104–115, 2004.

Martin Elvis, R. J. Brissenden, G. Fabbiano, D. A. Schwartz, P. Reid, W. Podgorski, M. Eisenhower, M. Juda, J. Phillips, L. Cohen, and S. Wolk. "Active x-ray optics for generation-x, the next high resolution x-ray observatory," *Proc. SPIE* **6266**. 62661K–62661K–11, 2006.

Peter Friedrich, Bernd Aschenbach, Christoph Braig, Heinrich Bruninger, Bernd Budau, Wolfgang Burkert, Michael J. Freyberg, Gisela Hartner, Gnther Hasinger, Peter Predehl, Monika Vongehr, Stefano Basso, Oberto Citterio, Mauro Ghigo, Francesco Mazzoleni, Giovanni Pareschi, Udo Dinger, Wilhelm Egle, Ralf Lenke, Georg Luichtel, and Herbert Schwarz. "Manufacturing of wolter-i mirror segments with slumped glass," *Proc. SPIE* **6266**. 62661G–62661G–8, 2006.

Jessica A. Gaskin, Martin C. Weisskopf, Alexey Vikhlinin, Harvey D. Tananbaum, Simon R. Bandler, Marshall W. Bautz, David N. Burrows, Abraham D. Falcone, Fiona A. Harrison, Ralf K. Heilmann, Sebastian Heinz, Randall C. Hopkins, Caroline A. Kilbourne, Chryssa Kouveliotou, Ralph P. Kraft, Andrey V. Kravtsov, Randall L. McEntaffer, Priyamvada Natarajan, Stephen L. ODell, Robert Petre, Zachary R. Prieskorn, Andrew F. Ptak, Brian D. Ramsey, Paul B. Reid, Andrew R. Schnell, Daniel A. Schwartz, and Leisa K. Townsley. "The x-ray surveyor mission: a concept study," *Proc. SPIE* **9601**. 96010J–96010J–14, 2015.

R. Giacconi, W. P. Reidy, G. S. Vaiana, L. P. Van Speybroeck, and T. F. Zehnpfennig. "Grazing-incidence telescopes for x-ray astronomy,". *Space Science Reviews*, 9(1):3–57, 1969. ISSN 1572-9672.

Dietrich Korsch, Charles L. Wyman, and L. Mike Perry. "Influence of alignment and surface defects on the performance of x-ray telescopes," *Proc. SPIE* **0184**. 211–222, 1979.

K. Nandra, D. Barret, X. Barcons, A. Fabian, J.-W. den Herder, L. Piro, M. Watson, C. Adami, J. Aird, J. M. Afonso, and et al. "The Hot and Energetic Universe: A White Paper presenting the science theme motivating the Athena+ mission,". *ArXiv e-prints*, June 2013.

Daniel Rodriguez Sanmartin, Dou Zhang, Tim Button, Carl Meggs, Carolyn Atkins, Peter Doel, David Brooks, Charlotte Feldman, Richard Willingale, Ady James, Graham

Willis, and Andy Smith. "Development of net-shape piezoelectric actuators for large x-ray optics," *Proc. SPIE* **7803**. 78030M–78030M–8, 2010.

R. Willingale, G. Pareschi, F. Christensen, and J.-W. den Herder. "The Hot and Energetic Universe: The Optical Design of the Athena+ Mirror,". *ArXiv e-prints*, July 2013.

Bibliography for Chapter 2

J. Aird, A. Comastri, M. Brusa, N. Cappelluti, A. Moretti, E. Vanzella, M. Volonteri, D. Alexander, J. M. Afonso, F. Fiore, I. Georgantopoulos, K. Iwasawa, A. Merloni, K. Nandra, R. Salvaterra, M. Salvato, P. Severgnini, K. Schawinski, F. Shankar, C. Vignali, and F. Vito. "The Hot and Energetic Universe: The formation and growth of the earliest supermassive black holes,". *ArXiv e-prints*, June 2013.

X. Barcons, D. Barret, A. Decourchelle, J.-W. den Herder, T. Dotani, A. C. Fabian, R. Fraga-Encinas, H. Kunieda, D. Lumb, G. Matt, K. Nandra, L. Piro, N. Rando, S. Sciortino, R. K. Smith, L. Strüder, M. G. Watson, N. E. White, and R. Willingale. "Athena (Advanced Telescope for High ENergy Astrophysics) Assessment Study Report for ESA Cosmic Vision 2015-2025,". *ArXiv e-prints*, July 2012.

M. Cappi, C. Done, E. Behar, S. Bianchi, V. Braito, E. Costantini, M. Dadina, C. Feruglio, F. Fiore, S. Gallagher, P. Gandhi, N. Grosso, J. Kaastra, A. King, A. Lobban, R. Maiolino, E. Piconcelli, G. Ponti, D. Porquet, K. Pounds, D. Proga, P. Ranalli, J. Reeves, G. Risaliti, P. Rodriguez Hidalgo, E. Rovilos, S. Sim, G. Stewart, F. Tombesi, T. G. Tsuru, S. Vaughan, D. Wang, and D. Worrall. "The Hot and Energetic Universe: Astrophysics of feedback in local AGN,". *ArXiv e-prints*, June 2013.

M. M. Civitani, S. Basso, M. Bavdaz, O. Citterio, P. Conconi, D. Gallieni, M. Ghigo, F. Martelli, G. Pareschi, G. Parodi, L. Proserpio, G. Sironi, D. Spiga, G. Tagliaferri, M. Tintori, E. Wille, and A. Zambra. "An integration machine for the assembly of the x-ray optic units based on thin slumped glass foils for the ixo mission," *Proc. SPIE* **8147**. 81470R–81470R–11, 2011.

J. H. Croston, J. S. Sanders, S. Heinz, M. J. Hardcastle, I. Zhuravleva, L. Bîrzan, R. G. Bower, M. Brüggen, E. Churazov, A. C. Edge, S. Ettori, A. C. Fabian, A. Finoguenov, J. Kaastra, M. Gaspari, M. Gitti, P. E. J. Nulsen, B. R. McNamara, E. Pointecouteau,

T. J. Ponman, G. W. Pratt, D. A. Rafferty, T. H. Reiprich, D. Sijacki, D. M. Worrall, R. P. Kraft, I. McCarthy, and M. Wise. "The Hot and Energetic Universe: AGN feedback in galaxy clusters and groups,". *ArXiv e-prints*, June 2013.

Jessica A. Gaskin, Martin C. Weisskopf, Alexey Vikhlinin, Harvey D. Tananbaum, Simon R. Bandler, Marshall W. Bautz, David N. Burrows, Abraham D. Falcone, Fiona A. Harrison, Ralf K. Heilmann, Sebastian Heinz, Randall C. Hopkins, Caroline A. Kilbourne, Chryssa Kouveliotou, Ralph P. Kraft, Andrey V. Kravtsov, Randall L. McEntaffer, Priyamvada Natarajan, Stephen L. ODell, Robert Petre, Zachary R. Prieskorn, Andrew F. Ptak, Brian D. Ramsey, Paul B. Reid, Andrew R. Schnell, Daniel A. Schwartz, and Leisa K. Townsley. "The x-ray surveyor mission: a concept study," *Proc. SPIE* **9601**. 96010J–96010J–14, 2015.

K. Nandra, D. Barret, X. Barcons, A. Fabian, J.-W. den Herder, L. Piro, M. Watson, C. Adami, J. Aird, J. M. Afonso, and et al. "The Hot and Energetic Universe: A White Paper presenting the science theme motivating the Athena+ mission,". *ArXiv e-prints*, June 2013.

L. Proserpio, M. Ghigo, S. Basso, P. Conconi, O. Citterio, M. Civitani, R. Negri, G. Pagano, G. Pareschi, B. Salmaso, D. Spiga, G. Tagliaferri, L. Terzi, A. Zambra, G. Parodi, F. Martelli, M. Bavdaz, and E. Wille. "Production of the ixo glass segmented mirrors by hot slumping with pressure assistance: tests and results," *Proc. SPIE* **8147**. 81470M–81470M–11, 2011.

R. Willingale, G. Pareschi, F. Christensen, and J.-W. den Herder. "The Hot and Energetic Universe: The Optical Design of the Athena+ Mirror,". *ArXiv e-prints*, July 2013.

Bibliography for Chapter 3

Ryan Allured, Sagi Ben-Ami, Vincenzo Cotroneo, Vanessa Marquez, Stuart McMuldroch, Paul B. Reid, Daniel A. Schwartz, Susan Trolier-McKinstry, Alexey A. Vikhlinin, and Margeaux L. Wallace. "Improved control and characterization of adjustable x-ray optics," *Proc. SPIE* **9603**. 96031M–96031M–10, 2015.

Marcos Bavdaz, Eric Wille, Kotska Wallace, Brian Shortt, Sebastiaan Fransen, Nicola Rando, Maximilien Collon, Marcelo Ackermann, Giuseppe Vacanti, Ramses Gnther, Jeroen Haneveld, Mark Olde Riekerink, Arenda Koelewijn, Coen van Baren, Dirk Kampf, Karl-Heintz Zuknik, Arnd Reutlinger, Finn Christensen, Desiree Della Monica Ferreira, Anders C. Jakobsen, Michael Krumrey, Peter Mller, Vadim Burwitz, Giovanni Pareschi, Mauro Ghigo, Marta Civitani, Laura Proserpio, Daniele Spiga, Stefano Basso, Bianca Salmaso, Daniele Gallieni, Matteo Tintori, Pierluigi Fumi, Francesco Martelli, Giancarlo Parodi, Ivan Ferrario, and Ian Povey. "X-ray optics developments at esa," *Proc. SPIE* **8861**. 88610L–88610L–12, 2013.

M. Civitani, S. Basso, M. Bavdaz, O. Citterio, P. Conconi, D. Gallieni, M. Ghigo, B. Guldimann, F. Martelli, G. Pagano, G. Pareschi, G. Parodi, L. Proserpio, B. Salmaso, D. Spiga, G. Tagliaferri, M. Tintori, E. Wille, and A. Zambra. "Ixo x-ray mirrors based on slumped glass segments with reinforcing ribs: optical and mechanical design, image error budget, and optics unit integration process," *Proc. SPIE* **7732**. 773242–773242–19, 2010.

M. M. Civitani, S. Basso, M. Bavdaz, O. Citterio, P. Conconi, D. Gallieni, M. Ghigo, F. Martelli, G. Pareschi, G. Parodi, L. Proserpio, G. Sironi, D. Spiga, G. Tagliaferri, M. Tintori, E. Wille, and A. Zambra. "An integration machine for the assembly of the x-ray optic units based on thin slumped glass foils for the ixo mission," *Proc. SPIE* **8147**. 81470R–81470R–11, 2011.

Maximilien J. Collon, Marcelo Ackermann, Ramses Gnther, Giuseppe Vacanti, Marco W. Beijersbergen, Marcos Bavdaz, Eric Wille, Kotska Wallace, Jeroen Haneveld, Mark Olde Riekerink, Arenda Koelewijn, Coen van Baren, Peter Mller, Michael Krumrey, Vadim Burwitz, Giorgia Sironi, and Mauro Ghigo. "Aberration-free silicon pore x-ray optics," *Proc. SPIE* **8861**. 88610M–88610M–11, 2013.

C. Feldman and R. Willingale. *Proc. SPIE* **8503**. October 2012.

R. Gnther, M. Collon, S. Kraft, M. Beijersbergen, M. Bavdaz, D. Lumb, A. Peacock, and K. Wallace. "Production of silicon pore optics," *Proc. SPIE* **6266**. 626619–626619–8, 2006.

Ryan S. McClelland, Michael P. Biskach, Kai-Wing Chan, Rebecca A. Espina, Bruce R. Hohl, Elizabeth A. Matson, Timo T. Saha, and William W. Zhang. "Design, construction, and testing of lightweight x-ray mirror modules," *Proc. SPIE* **8861**. 88610O–88610O–13, 2013.

K. Nandra, D. Barret, X. Barcons, A. Fabian, J.-W. den Herder, L. Piro, M. Watson, C. Adami, J. Aird, J. M. Afonso, and et al. "The Hot and Energetic Universe: A White Paper presenting the science theme motivating the Athena+ mission,". *ArXiv e-prints*, June 2013.

P. B. Reid, T. L. Aldcroft, V. Cotroneo, W. Davis, R. L. Johnson-Wilke, S. McMuldroch, B. D. Ramsey, D. A. Schwartz, S. Trolier-McKinstry, A. Vikhlinin, and R. H. T. Wilke. "Technology development of adjustable grazing incidence x-ray optics for sub-arc second imaging," *Proc. SPIE* **8443**. 84430T–84430T–8, 2012.

Raul E. Riveros, Vincent T. Bly, Linette D. Kolos, Kevin P. McKeon, James R. Mazzarella, Timothy M. Miller, and William W. Zhang. "Fabrication of single crystal silicon mirror substrates for x-ray astronomical missions," *Proc. SPIE* **9144**. 914445–914445–6, 2014.

D. Spiga, S. Basso, M. Bavdaz, V. Burwitz, M. Civitani, O. Citterio, M. Ghigo, G. Hartner, B. Menz, G. Pareschi, Laura Proserpio, B. Salmaso, G. Tagliaferri, and E. Wille. "Profile reconstruction of grazing-incidence x-ray mirrors from intra-focal x-ray full imaging," *Proc. SPIE* **8861**. 88611F–88611F–17, 2013.

D. Spiga, M. Barbera, S. Basso, M. Civitani, A. Collura, S. Dell'Agostino, U. Lo Cicero, G. Lullo, C. Pelliciari, M. Riva, B. Salmaso, and L. Sciortino. **9208**. 92080A, September 2014.

D. Spiga, M. Barbera, S. Basso, M. Civitani, A. Collura, S. Dell'Agostino, U. Lo Cicero, G. Lullo, C. Pelliciari, M. Riva, B. Salmaso, and L. Sciortino. "Active shape correction of a thin glass/plastic x-ray mirror," *Proc. SPIE* **9208**. 92080A–92080A–10, 2014.

D. Spiga, M. Barbera, A. Collura, S. Basso, R. Candia, M. Civitani, M. S. Di Bella, G. Di Cicca, U. Lo Cicero, G. Lullo, C. Pelliciari, M. Riva, B. Salmaso, L. Sciortino, and S. Varisco. "Manufacturing an active X-ray mirror prototype in thin glass,". *Journal of Synchrotron Radiation*, 23(1):59–66, Jan 2016.

Edward Sung, Brandon Chalifoux, Mark L. Schattenburg, and Ralf K. Heilmann. "Non-touch thermal air-bearing shaping of x-ray telescope optics," *Proc. SPIE* **8861**. 88610R–88610R–8, 2013.

Melville P. Ulmer, Xiaoli Wang, Jian Cao, Julia Savoie, Bridget Bellavia, Michael E. Graham, and Semyon Vaynman. "Progress report on using magneto-strictive sputtered thin films to modify the shape of a x-ray telescope mirror," *Proc. SPIE* **8503**. 85030C–85030C–8, 2012.

Xiaoli Wang, Youwei Yao, Jian Cao, Semyon Vaynman, Michael E. Graham, Tianchen Liu, and M. P. Ulmer. "Investigation of magnetically smart films applied to correct the surface profile of light weight x-ray optics in two directions," *Proc. SPIE* **9603**. 96031O–96031O–9, 2015.

Anita Winter, Elias Breunig, Vadim Burwitz, Peter Friedrich, Gisela Hartner, Benedikt Menz, and Laura Proserpio. "Light-weight glass mirror systems for future x-ray telescopes," *Proc. SPIE* **8861**. 88610Q–88610Q–10, 2013.

Bibliography for Chapter 4

Carolyn Atkins. *Active X-ray optics for the next generation of X-ray space telescopes.* PhD thesis, University College London, 10 2009.

Charlotte Feldman. *Smart X-ray optics for large and small scale applications.* PhD thesis, University of Leicester, 11 2009.

Charlotte Feldman, Richard Willingale, Carolyn Atkins, David Brooks, Tim Button, Peter Doel, Ady James, Daniel Rodriguez Sanmartin, Andy Smith, Craig Theobald, Samantha Thompson, Hongchang Wang, and Dou Zhang. "First results from the testing of the thin shell adaptive optic prototype for high angular resolution x-ray telescopes," *Proc. SPIE* **7437**. 74371G–74371G–11, 2009.

Charlotte Feldman, Richard Willingale, Carolyn Atkins, David Brooks, Tim Button, Peter Doel, Ady James, Carl Meggs, Daniel Rodriguez-Sanmartin, Andy Smith, Craig Theobald, and Graham Willis. "The performance of thin shell adaptive optics for high angular resolution x-ray telescopes," *Proc. SPIE* **7803**. 78030N–78030N–10, 2010.

Stephen L. O'Dell, Thomas L. Aldcroft, Carolyn Atkins, Timothy W. Button, Vincenzo Cotroneo, William N. Davis, Peter Doel, Charlotte H. Feldman, Mark D. Freeman, Mikhail V. Gubarev, Raegan L. Johnson-Wilke, Jeffery J. Kolodziejczak, Charles F. Lillie, Alan G. Michette, Brian D. Ramsey, Paul B. Reid, Daniel Rodriguez Sanmartin, Timo T. Saha, Daniel A. Schwartz, Susan E. Trolier-McKinstry, Melville P. Ulmer, Rudeger H. T. Wilke, Richard Willingale, and William W. Zhang. "Toward active x-ray telescopes ii," *Proc. SPIE* **8503**. 850307–850307–15, 2012.

Daniel Rodriguez Sanmartin, Dou Zhang, Tim Button, Carl Meggs, Carolyn Atkins, Peter Doel, David Brooks, Charlotte Feldman, Richard Willingale, Ady James, Graham Willis, and Andy Smith. "Development of net-shape piezoelectric actuators for large x-ray optics," *Proc. SPIE* **7803**. 78030M–78030M–8, 2010.

Dou Zhang, Daniel Rodriguez Sanmartin, Tim W. Button, Carl Meggs, Carolyn Atkins, Peter Doel, David Brooks, Charlotte Feldman, Richard Willingale, Alan Michette, Slawka Pfauntsch, Shahin Sahraei, Ady James, Camelia Dunare, Tom Stevenson, William Parkes, Andrew Smith, and Hongchang Wang. "The fabrication and characterisation of piezoelectric actuators for active x-ray optics," *Proc. SPIE* **7448**. 744807–744807–9, 2009.

Bibliography for Chapter 5

Pinjiang He, Xiaoying Zong, and Ruimin Fu. "Zernike polymomials for rectangular area and applications in off-axis asphere testing," *Proc. SPIE* **7656**. 765615–765615–6, 2010.

Bibliography for Chapter 6

M. M. Civitani, S. Basso, M. Bavdaz, O. Citterio, P. Conconi, D. Gallieni, M. Ghigo, F. Martelli, G. Pareschi, G. Parodi, L. Proserpio, G. Sironi, D. Spiga, G. Tagliaferri, M. Tintori, E. Wille, and A. Zambra. "An integration machine for the assembly of the x-ray optic units based on thin slumped glass foils for the ixo mission," *Proc. SPIE* **8147**. 81470R–81470R–11, 2011.

Mauro Ghigo, Laura Proserpio, Stefano Basso, Oberto Citterio, Marta M. Civitani, Giovanni Pareschi, Bianca Salmaso, Giorgia Sironi, Daniele Spiga, Giampiero Tagliaferri, Gabriele Vecchi, Alberto Zambra, Giancarlo Parodi, Francesco Martelli, Daniele Gallieni, Matteo Tintori, Marcos Bavdaz, Eric Wille, Ivan Ferrario, and Vadim Burwitz. "Slumping technique for the manufacturing of a representative x-ray grazing incidence mirror module for future space missions," *Proc. SPIE* **8884**. 88841Q–88841Q–14, 2013.

Ryan S. McClelland, Michael P. Biskach, Kai-Wing Chan, Rebecca A. Espina, Bruce R. Hohl, Elizabeth A. Matson, Timo T. Saha, and William W. Zhang. "Design, construction, and testing of lightweight x-ray mirror modules," *Proc. SPIE* **8861**. 88610O–88610O–13, 2013.

Bibliography for Chapter 7

Tom Catling, David Brooks, and Peter Doel. "Phase measuring deflectometry for thin actuated mirrors," *Proc. SPIE* **9151**. 91510S–91510S–6, 2014.

Run Huang, Peng Su, James H. Burge, and Mourad Idir. "X-ray mirror metrology using scots/deflectometry," *Proc. SPIE* **8848**. 88480G–88480G–6, 2013.

Reinhard Klette and Karsten Schlns. "Height data from gradient fields,". In *Proceedings of SPIE (the international Society for Optical Engineering) on Machine Vision Applications, Architectures, and Systems Integration* , 204–215, 1996.

Peng Su, Yuhao Wang, James H Burge, Konstantine Kaznatcheev, and Mourad Idir. "Non-null full field x-ray mirror metrology using scots: A reflection deflectometry approach,". *Optics express*, 20(11):12393–12406, 2012.

Bibliography for Chapter 8

Bibliography for Chapter 9

Tom Catling, David Brooks, and Peter Doel. "Phase measuring deflectometry for thin actuated mirrors," *Proc. SPIE* **9151**. 91510S–91510S–6, 2014.

Ryan S. McClelland, Michael P. Biskach, Kai-Wing Chan, Rebecca A. Espina, Bruce R. Hohl, Elizabeth A. Matson, Timo T. Saha, and William W. Zhang. "Design, construction, and testing of lightweight x-ray mirror modules," *Proc. SPIE* **8861**. 88610O–88610O–13, 2013.

D. Spiga, M. Barbera, A. Collura, S. Basso, R. Candia, M. Civitani, M. S. Di Bella, G. Di Cicca, U. Lo Cicero, G. Lullo, C. Pelliciari, M. Riva, B. Salmaso, L. Sciortino, and S. Varisco. "Manufacturing an active X-ray mirror prototype in thin glass,". *Journal of Synchrotron Radiation*, 23(1):59–66, Jan 2016.

Peng Su, Yuhao Wang, James H Burge, Konstantine Kaznatcheev, and Mourad Idir. "Non-null full field x-ray mirror metrology using scots: A reflection deflectometry approach,". *Optics express*, 20(11):12393–12406, 2012.